WATERAGRI

D3.1: Assessment of Use of Remotely Sensed Vegetation to Improve Irrigation

10/2021

WP 3 Innovative Sustainable Water Retention and Management Measures

This project has received funding from the European Union's Horizon 2020 research and innovation programme under Grant Agreement No 858375.

Author(s)/Organisation(s)	Attila Nagy (UNIDEB) Zsolt Zoltán Fehér (UNIDEB) Tamás Magyar (UNIDEB) Philip Brunner (UNINE) Oliver Schilling (UNINE) Harrie-Jan Hendricks-Franssen (FZJ) Francesco Cavazza (CER) Kedar Ghag (OULU) Syed Mustafa (OULU) Bjørn Kløve (OULU) Ali Torabi Haghighi (OULU)
Contributor(s)	Haidi Abdullah (VULTUS) Erika Buday-Bódi (UNIDEB) János Tamás (UNIDEB) Dávid Pásztor (UNIDEB) Andrea Szabó (UNIDEB) Wiesław Fiałkiewicz (UPWr) Arkadiusz Głogowski (UPWr) Adriano Battilani (CER) Diego Guidotti (Agricolus)
Work Package	WP3
Delivery Date (DoA)	31/10/2021
Actual Delivery Date	31/10/2021
Abstract:	Deliverable "D3.1: Assessment of Use of Remotely Sensed Vegetation to Improve Irrigation" report the activities of Tasks T3.2 (Irrigation Scheduling). The Deliverable describes the role of Lidar in excess water risk mapping, the utilization of groundwater and surface water for irrigation, hydrological modelling to support irrigation, RS based yield prediction model and RS based vegetation data in irrigation.

Document Revision History			
Date	**Version**	**Author/Contributor/ Reviewer**	**Summary of main changes**
27/07/2021	v1	Attila Nagy (UNIDEB)	table of contents (structure plan)
21/09/2021	v2	Attila Nagy (UNIDEB), Diego Guidotti (Agricolus), Haidi Abdullah (VULTUS), Bjørn Kløve (OULU), Adriano Battilani (CER)	first draft (includes data and information requested)
27/09/2021	v3	Attila Nagy (UNIDEB), Oliver Schilling (UNINE), Harrie-Jan Hendricks-Franssen (FZJ)	2nd internal draft
30/09/2021	v4	Attila Nagy (UNIDEB), Wiesław Fiałkiewicz (UPWr)	3rd internal draft
02/10/2021	v5	UNIDEB and other partners	4th internal draft
12/10/2021	v6	Attila Nagy (UNIDEB) and other UNIDEB partners,	content check (chapters including figures and tables)

		Bjørn Kløve (OULU), Harrie-Jan Hendricks-Franssen (FZJ)	
29/10/2021	v7	Harrie-Jan Hendricks-Franssen (FZJ), Erika Buday-Bódi (UNIDEB) and UNIDEB colleagues	language and formal check
30/10/2021	v8	Suhad Almuktar (ULUND), Sebastian Puculek (ULUND)	quality check
31/10/2021	final	Miklas Scholz (ULUND)	final version

Dissemination Level		
PU	Public	X

WATERAGRI Consortium			
Participant Number	Participant organisation name	Short name	Country
1	LUNDS UNIVERSITET	ULUND	SE
2	EDEN MICROFLUIDICS	EDEN	FR
3	FORSCHUNGSZENTRUM JULICH GMBH	FZJ	DE
4	TEKNOLOGIAN TUTKIMUSKESKUS VTT Oy	VTT	FI
5	DEBRECENI EGYETEM	UNIDEB	HU
6	ALCHEMIA-NOVA GMBH	ALCN	AT
7	AGROGEO AGARFEJLESZTO-FOLDTANI-FOVALLALKOZO KORLATOLT FELELOSSEGU TATRSASAG	AGROGEO	HU
8	UNIVERSITAET FUER BODENKULTUR WIEN	BOKU	AT
9	ALMA MATER STUDIORUM UNIVERSITA DI BOLOGNA	UNIBO	IT
10	THE UNIVERSITY OF SALFORD	USAL	UK
11	COCONSORZIO DI BONIFICA DI SECONDO GRADO PER IL CANALE EMILIANO ROMAGNOLO CANALE GIANDOTTI	CER	IT
12	CENTRUM DORADZTWA ROLNICZEGO W BRWINOWIE	CDR	PL
13	INOSENS DOO NOVI SAD	INOSENS	RS
14	UNIWERSYTET PRZYRODNICZY WE WROCLAWIU	UPWr	PL
15	BAY ZOLTAN ALKALMAZOTT KUTATASI KOZHASZNU NONPROFIT KFT	BZN	HU
16	VULTUS AB	VULTUS	SE
17	TECHNISCHE UNIVERSITEIT DELFT	TU DELFT	NL
18	UNIVERSITE DE NEUCHATEL	UNINE	CH
19	AB GARDSTANGA NYGARD	GN	SE
20	OULUN YLIOPISTO	OULU	FI
21	AGRICOLUS SRL	AGRICOLUS	IT
22	INSTITUT NATIONAL DE RECHERCHE POUR L'AGRICULTURE, L'ALIMENTATION ET L'ENVIRONNEMENT	INRAE	FR
23	MARTIN REGELSBERGER	TBR	AT

Funding Scheme: Research and Innovation Action (RIA) ● Theme: SFS-23-2019
Start date of project: 01 May 2020 ● Duration: 48 months

Table of contents

List of tables

List of figures

List of Abbreviations and Acronyms	
Q_0	volumetric flux per unit surface area
q_0	average surface water flow velocity
1-D	one-dimensional
3D	3-dimensional
Adj. R-sq	same as R-squared with adjustment
AVHRR	Advanced Very High-Resolution Radiometer
BBCH	exact abbr. of ‘Biologische Bundesanstalt, Bundessortenamt und CHemische Industrie’ by which phenological phases are expressed
CCD	charge-coupled device
CWSI	Crop Water Stress Index
DEM	Digital Elevation Model
DFE	Degrees of Freedom error
dpi	dot per inch
E1	Nash-Sutcliffe efficiency index
elev.	elevation
EnKF	ensemble Kalman filter
EOV	Egységes Országos Vetület (in Hungarian) (in English: Unified National Projection of Hungary)
ESA	European Space Agency
ET	evapotranspiration
ET_0	reference evapotranspiration
ET_c	crop evapotranspiration
F(x)	particle size distribution
FAO	Food and Agriculture Organization
fAPAR	Fraction of Absorbed Photosynthetically Active Radiation
GW	groundwater
HGS	HydroGeoSphere
HGS-PDAF	HydroGeoSphere-Parallel Data Assimilation Framework
I	irrigation
IEW	inland excess water
k	conductivity
K_c	crop coefficient
LAI	Leaf Area Index
LANDSAT	Land Remote-Sensing Satellite
LiDAR	Light Detection and Ranging
MODIS	Moderate Resolution Imaging Spectroradiometer
MSI	MultiSpectral Instrument
NDRE	Normalized Difference Red Edge
NDREw	Normalized Difference Red Edge for wheat

NDVI	Normalized Difference Vegetation Index
NDWI	Normalized Difference Water Index
NIR	near infrared
NPBR	Normalized Ration Procedure between bands VV and VH polarization
NRMSE	Normalized Root Mean Square
nRMSE	normalized Root Mean Square Error
NUT 2	Nomenclature des Unités Territoriales Statistiques (in French) (in English: Nomenclature of Territorial Units for Statistics) – level2
OLI	operational land imager
P	precipitation
PCHIP	Piecewise Cubic Hermite Interpolating Polynomial
PDAF	Parallel Data Assimilation Framework
R2, R-sq, R-square	Coefficient of Determination
RMSE	Root Mean Square Error
RS	Remote Sensing
RS-based	Remote Sensing based
RWU	root water uptake
SAVI	Soil Adjusted Vegetation Index
SLA	Specific Leaf Area
SNAP	Sentinel Application Platform
SPEI	Standardized Precipitation Evapotranspiration Index
SPI	Standardized Precipitation Index
SPOT	Satellite pour l'Observation de la Terre (in French) (in English: Satellite for observation of Earth)
SSE	sum of squared error
SWIR	short-wave infrared
TIRS	thermal infrared sensors
USGS	United States Geological Survey
VI, VIs	vegetation index, plural: vegetation indices
VRE	Vegetation Red-Edge
WB	water balance
WD	water deficit
WF	cumulative water fluxes
WRF	Weather Research and Forecast
θ	volumetric water content
θ_p	porosity
ρ_B	bulk density
ρ_p	particle density
Ψ_m	water retention

1 Introduction

Due to the growth in global demand for food and the increasing pressure on agricultural ecosystems related to climate change, early and reliable information on crop production has become essential for decision-making in agricultural practice.

Over the past decades, the variability of weather has increased in many regions of Europe, just like in other parts of the world. The impact of climate change on hydrological variables like precipitation, temperature and soil moisture is highly uncertain and depends on seasons and regions (Vautard et al., 2013; Putnam and Broecker, 2017; Ruosteenoja et al., 2017). Most climate scenarios predict increased water scarcity in arid areas, such as Hungary. Although the annual precipitation trend remains very uncertain, the frequency of droughts has already increased significantly due to rising temperatures and the associated potential evapotranspiration. Reduced precipitation and soil moisture levels in the spring and summer due to climate change are expected to affect agricultural crop production even in northern Europe negatively (Rummukainen et al., 2004; Ruosteenoja et al., 2017). Summer drought has become a common and recurring phenomenon in Finland. When drought occurs at the water-sensitive stages of crops, it leads to substantial (10 - 20 %) yield loss (Peltonen-Sainio et al., 2021). As a result, summer droughts are causing significant reduction in food production volumes. For example, in Finland, the drought in the summer of 2018 was observed to result in low grain yield (https://yle.fi/uutiset/osasto/news/10688762, last accessed on 19 September 2021).

At the same time, the presence of excess water causes a growing challenge and a valid concern in agricultural production in Europe as well. In addition, inland excess water and drought often appear simultaneously in a year, which can also influence agricultural production negatively. Groundwater may play an important role in building resilience to hydrological extremes especially during summer drought. However, long-term dependence on groundwater for irrigation may have considerable adverse effects on environmental conditions.

One of the measures to tackle the effects of drought and to secure sustainable food production by the avoiding of substantial yield losses is irrigation at the water-sensitive stage of crops. The reuse and improved use of drainage water for irrigation through improved drainage control could be an essential strategy to reduce yield losses during summer drought, as well as the loading of nutrients into surface water. Proper irrigation control requires real-time data about the agricultural field, the surrounding catchment and the condition of the crop so that water balance may be defined properly. There are several physically based hydrological models available for modelling, which can be operated at various scales. Irrigation is usually based on the measurement of the water content in soil or meteorological variables used to model or calculate evapotranspiration (Nagy - Tamás, 2009). In recent years, mobile meteorological stations and soil sensors have been employed to measure the meteorological conditions and water supply of plants in real time. Plant-based methods, such as the plant water stress index, represent a great potential for irrigation control, although the definition of reference or threshold values might be problematic (Jones 2004). The development of biomass monitoring tools helps with surveying the spatial variability of plants and plant biomass (Tsutsumi - Itano, 2005). Remote sensing based (RS-based) prediction models developed from vegetation indices have the potential to provide quantitative and timely information on crops for larger regions or even at the local farm scale. The first steps in quantitative hydrogeological modelling will also be presented. These models enable us to simulate water flow in both the surface and subsurface domain, as well as the coupling between them, which makes it possible to manage surface and subsurface water resources jointly. The calibration of the model includes the elaboration of a conceptual model and the appropriate climatic and hydraulic boundary conditions. Based on observation data, model parameters such as hydraulic conductivity can be calibrated subsequently. At the current stage of the project, the elaboration of the conceptual model has been completed, and a preliminary sensitivity analysis concerning driving climatic factors and soil moisture dynamics has been carried out.

In summary, the water balance modelling of agricultural sites and catchments, the enhanced use of drainage water for irrigation, and the fast, real-time monitoring of drought and inland excess water are essential for a better understanding of the soil–water–plant nexus and the ensuing improvement of irrigation scheduling practices. In this deliverable, a simple, flexible and eco-friendly approach is presented to reuse drainage water for irrigation through improved drainage control, which promotes a circular economy. The report also discusses the capabilities of remote sensing techniques in improving crop yield and monitoring with a view to supporting the farming community in preparation for future climate change scenarios. Moreover, quantitative hydrogeological modelling, various RS data, vegetation indices and modelling activities have also been assessed for the purpose of irrigation scheduling, however, their efficiency in estimating evapotranspiration needs further testing in WP5.

2 The role of Lidar in mapping excess water risk

Inland excess water (IEW) bodies are being globally threatened by ongoing urbanization, agricultural irrigation, environmental degradation and climate change (Vörösmarty et al., 2010). Due to climate change, extreme water management conditions (for instance inland excess water) have become a growing challenge and represent now a real concern for agricultural production in Europe as well. The Hungarian case study site is also affected by inland excess water every third year on the average. The formation of excess water is in part based on terrain characteristics, but soil compaction also makes a negative impact on infiltration, which in turn contributes to the formation of excess water. Though the site is not equipped with any variable rate irrigation system, it is important to delineate spots with the potential risk of excess water in general, since such spots should be irrigated at a lower intensity and with less water input. The mapping of excess water requires the application of a DEM with proper resolution or a DEM combined with RS data sources so that spots covered by excess water may be detected. For this reason, the goal was to assess the applicability of various digital elevation models in the mapping of inland excess water based on the example of the Hungarian case study site. The elevation models assessed in the current study are derived from conventional topographic maps, aerial laser scanning a. k. a. LiDAR and active satellite remote sensing by the SENTINEL 1 Synthetic Aperture Radar products, provided by the European Space Agency.

2.1 Study site and methods

The reference area is a grassland site of 15.6 hectares in the northeastern part of Hungary. Figure 1 shows the spatial location of the area. Under the current research, IEW affected areas were identified by the processing of digital elevation models of different origins and characteristics.

(1) In the case of DEM generated from analogue basic data, the processing steps comprised the scanning of the conventional topographical paper map at a resolution of 600 dpi and its georeferencing into the Unified National Projection of Hungary (in Hungarian: Egységes Országos

Vetület: EOV, EPSG:23.700) projection. Subsequently, a vector layer was created and contour lines were digitalised based on the topographical map. There was also a database compiled from height data. A total of 25.372 vertex points representing height data were used as an input and a 3D contour surface was generated with the kriging method. The areas susceptible to inland excess water were then marked based on the elevation model.

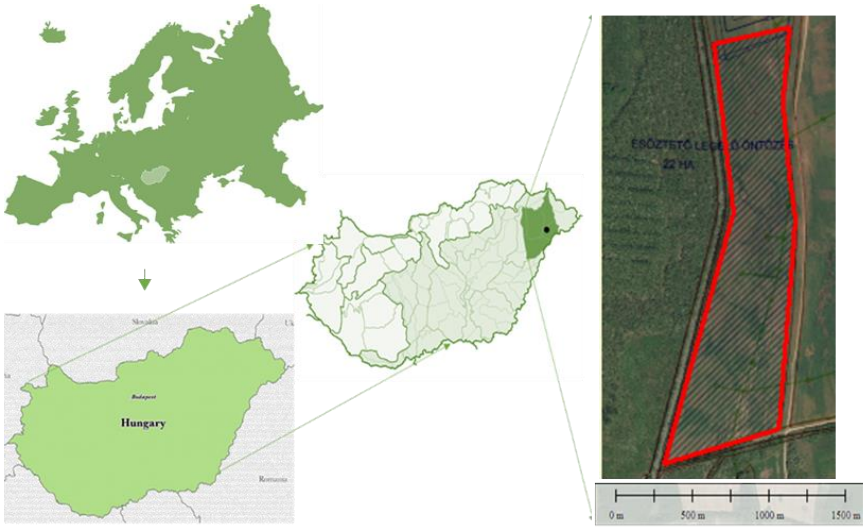

Figure 1: Location of the study area of LiDAR mapping

(2) The aerial LiDAR survey is the product of the cooperation between the Institute of Water and Environmental Management and Eurosense Ltd. The laser scan survey was carried out with the IGI LiteMapper system. The grassland was surveyed in March, i.e. at the beginning of the vegetation period and the lowest vegetation level, when excess water was mostly present at the site. All these conditions were optimal for the understanding of the topography of the areas and the evaluation of the differences in micro-relief. The area comprised 129,072,937 points in total. The resolution of LiDAR data points is 14.58 point/m^2, thus they can be used to build high resolution models. The laser point cloud processed by photogrammetry was pre-processed with the software GlobalMapper. A preliminary elevation profile analysis was carried out in the software for the grassland.

On the basis of LiDAR images, the maps of slope categories were prepared and finally the inland marshes were marked in the sample area. The elevation model based on high-resolution LiDAR data was analysed through steps similar to those used for processing the DEM based on analogous (so-called traditional) data. After that, roads, canals and reservoirs were sorted out. In the next phase, run-off and accumulation relations were investigated on the basis of slope conditions. After this, the intensity values of the laser survey were examined for the purpose of mapping inland excess water. In the next step, the applicability of digital elevation models for mapping IEW was compared based on three different types of mapping, traditional and LiDAR images, as well as Synthetic Aperture Radar products.

(3) Sentinel 1 data were downloaded for the grassland area from the website of the European Space Agency (ESA) (https://scihub.copernicus.eu/). Radar images (amplitude values) were processed in the software environment of the ESA Sentinel Application Platform (SNAP) 2.0. As a first step of pre-processing, the radiometric calibration of the images took place to get the Sigma0_VV channel, then speckle filtering was done. It was followed by a geometric correction (range Doppler terrain

correction). Finally, a binary transformation was carried out on the basis of the histogram, where low values correspond to water, while high values represent non-water areas. Based on the histogram, the threshold to separate water from the land was determined to be 2.21 x 10^{-2}.

During segmentation, the following formula was used:

$$255 * (\sigma 0_{VV} < 2.21\ x\ 10^{-2})$$

The expression $\sigma 0_{VV}$<2.21 x 10^{-2} is interpreted as a logical value. Values less than 2.21 x 10^{-2} are true (represented with 1), whereas values higher than that are false (represented with 0).

2.2 LiDAR in mapping excess water risk

Firstly, the digital elevation models (DEM) produced from the digitization of analogous data and the aerial LiDAR were subjected to a comparative analysis on the relief of the grassland (Figure 2). The results calculated based on the 1:10 000 scale topographical map show that the risk of inland excess water is low, if only the elevation of the grassland is considered. In contrast to this, however, there were inland marshes visible in the grassland during site visits, which are also demonstrated in the aerial laser images. This can be explained in part by the soil and hydrological characteristics of the site, and the 10-meter resolution of the elevation model, which does not allow the monitoring of the micro relief.

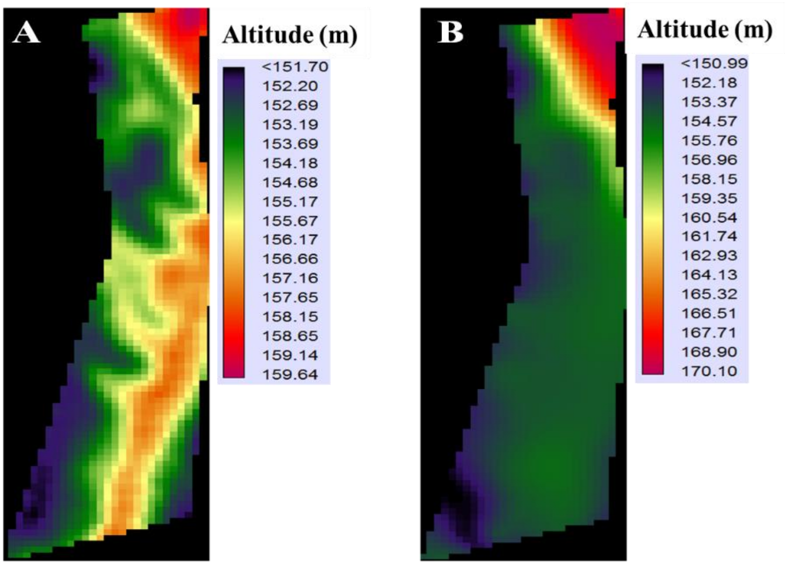

Figure 2: Elevation values based on 10x10 m spatial resolution databases (A – Relief map from LiDAR data B – Relief map from topographical map)

The height difference in the area is 7.94 m according to laser data and 19.11 m according to conventional DEM (obtained by the digitising of analogous basic data). The information content of the relief map derived from topographical data is much more limited, thus the interpolator is smoothing the difference in the terrain, due to the low resolution of the 1:10 000 scale data sources (Figure 3/A).

Schumann et al. (2008) compared the suitability of digital terrain models based on LiDAR, contour line map and SRTM in hydrological modelling. Based on their findings, they concluded that the DEM based on LiDAR was the best, followed by the SRTM and then the DEM based on contour lines/traditional maps.

The DEM and the slope category map, as well as the runoff map of the grassland with the catchments were also determined (Figure 3/D). The hill (sand dune) rises from the lowest spot of the area to a height of 5 meters and this elevation of the relief serves as a catchment border. On the basis of the runoff lines, the deeper accumulation cauldrons could pool water from high-intensity precipitation or snowmelt, hence, the intensity values of the laser survey were analysed.

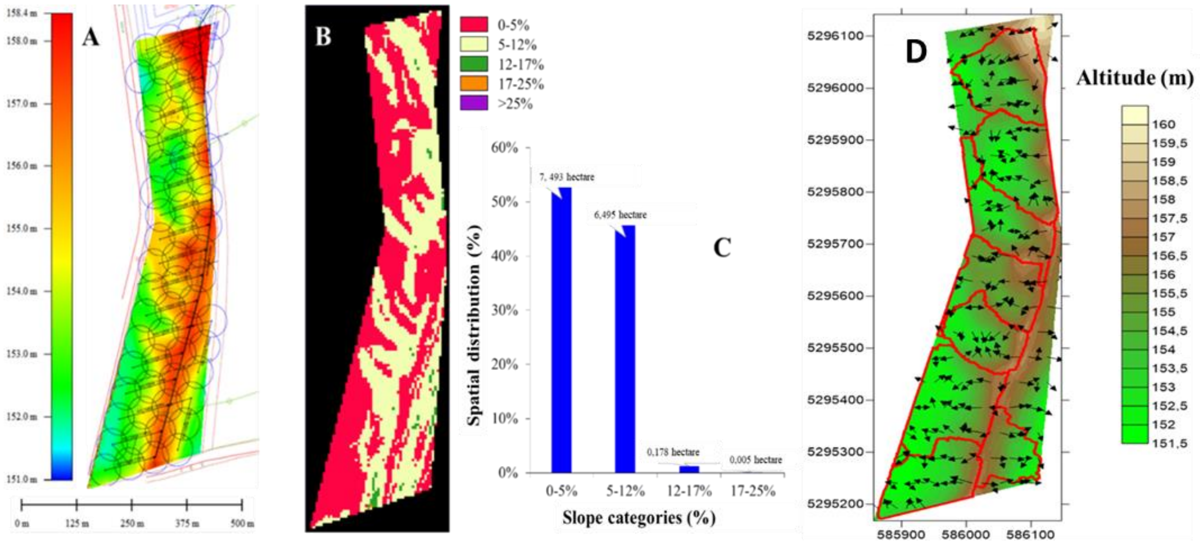

Figure 3: Terrain model (A) and slope categories (B and C) of the studied grassland and the digital elevation model with runoff vectors and water catchments (arrows: run-off vectors; red contour: sub-catchments) (D)

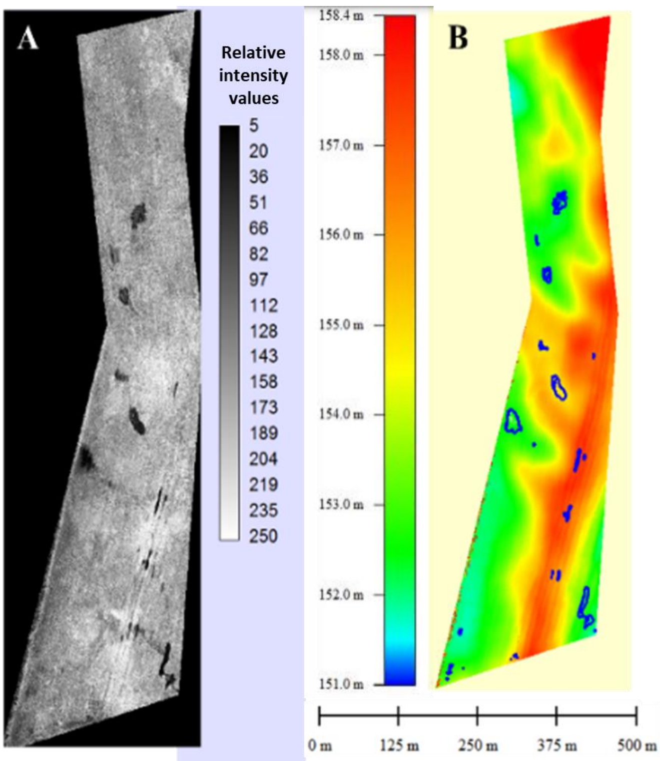

Figure 4: The map generated based on the reflected laser intensity (A) and the LiDAR-based DEM with IEW (blue contours) (B)

Since the airborne LiDAR system used the infrared wavelength range for the measurements, it can be suitable for mapping potentially harmful excess surface water. During the selection of intensity values, 45 areas affected by harmful inland excess water were identified, representing almost 0.2 ha as a whole (Figure 4). Some areas were classified improperly in the sorting process (mainly the southern areas of a size of less than 15 m^2) due to higher point density. After the sorting of these areas, no more than 13 larger and coherent areas affected by inland excess water could be found; the size of more than half of which was less than 100 m^2, while that of the largest inland marsh was 512.5 m^2. 73 % of the inland water is found at low altitudes (151-154 m) in relatively flat areas. But the rest of the inland excess water spots are situated in higher elevation areas (155.81-157.37 m), in the top region of the sand dunes, which can probably be explained by soil compaction.

Inland excess water patches were identified not only by LiDAR-based products, but also topographical map based DEM. In the grassland, no inland excess water patches could be identified according to the topographical map (Figure 5).

Other research also concluded that LiDAR and high-resolution DEM could be used in hydrological sensitive areas. Yang et al. (2014) investigated the impact of a digital elevation model based on LiDAR on large-scale river basin modelling. Their findings revealed that, in the field of hydrology and hydroinformatics, it could be better to use DEM derived from high-resolution LiDAR. Thomas et al. (2017) examined hydrological sensitive areas based on digital elevation models. The research found that 1-2 m is the best resolution for the analysis of micro topography.

Figure 5: Location of inland excess water patches based on the digital elevation model derived from the 1:10 000 topographic map

In this research, wet areas identified by Sentinel 1 data were also assessed in comparison to LiDAR-based IEW areas (Figure 6). According to the Synthetic Aperture Radar data, wet area only covers LiDAR-based inland excess water patches number 5, 6 and 7 located in low relief areas (152.24-154.88 m). However, other patches were not exactly matched, probably because the relatively coarse 10 m spatial resolution of the Sentinel 1 data resulted in the spectral mixing in pixels.

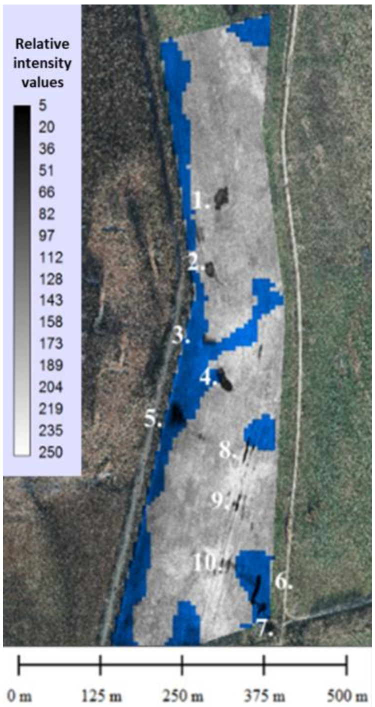

Figure 6: Wet sites (blue color) based on Sentinel data and largest IEW patches (black spots with numbers from 1 to 10) based on LiDAR map

Based on the DEM derived from LiDAR, inland excess water patches were analysed with the use of laser intensity values. In conclusion, from the data assessed, LiDAR data proved to be appropriate to map the micro-topographical differences and thus the IEW of a site precisely, while conventional topographic map-based DEM [due to its scale (1:10 000)] and Sentinel 1 [due to its coarse resolution] have certain limitations in modelling IEW at field scale. According to our findings, topography and associated runoff were the primary causes of the formation of IEW.

3 The use of surface and groundwater for irrigation

In Finland, irrigation is needed for growing some crops, such as potato, especially in dry years. In the coastal lowlands, where most of the agricultural areas are located, annual precipitation is relatively low and irrigation is beneficial for crop production. Irrigation is realized by the using of water from lakes and rivers, but due to the lack of surface water in some regions, farmers are also interested in using groundwater, especially as agricultural lands are located near or even on the top of aquifers in this coastal region. The objective of our study was to analyze water demand and irrigation scheduling and to assess the potentials for the use of surface and groundwater for potato cultivation.

3.1 Study area and data

The study area *"Isosuo"* (6.43 ha) is located in the municipality of Tyrnävä, 32 km southeast of the city of Oulu (between 64°45'21" N to 64°45'33" N Latitudes and 25°43' 40" E to 25°43'0" E Longitudes) in the North Ostrobothnia region of Finland (Figure 7). The Tyrnävä area has boreal or cold climate with long periods of sub-zero temperatures and deep ground frost during winter. The region is mostly covered by snow from late October until mid-April. May to September is the best period for potato production. Normally, farming operations start in late May depending on snow and frost conditions. Crop harvesting takes place in September. In the cropping period, the length of the daytime reaches nearly 24 hours.

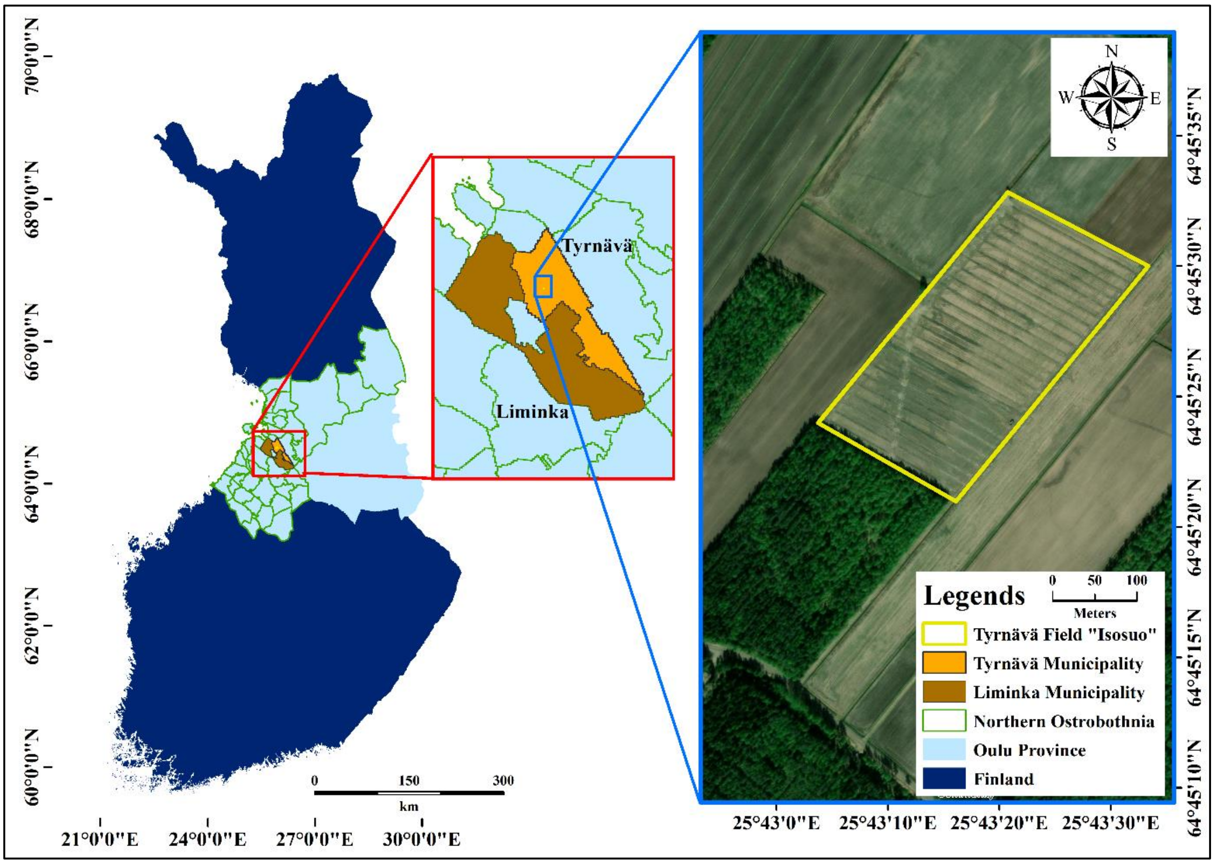

Figure 7: Location of Tyrnävä study area in the Oulu province of Finland

The municipalities of Tyrnävä and Liminka are important for potato cultivation on a regional, national, and EU scale alike. Seed potatoes are produced on ca. 700 hectares and food potatoes are produced on nearly 500 hectares on 28 seed potato farms and 21 food potato farms, respectively. These two municipalities produce around 70-75% of all Finnish seed potatoes, about 17-18 million kilograms in total, of which nearly 3-4 million kilograms are exported annually.

The temporal resolution of hydrological and climatological data collected in the region are shown in Figure 8.

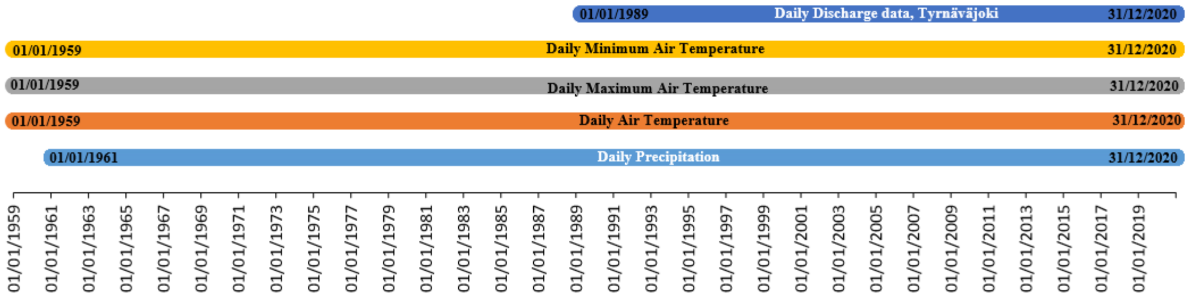

Figure 8: Data availability details

3.2 Methods

3.2.1 Water balance

Water balance calculations were used to assess irrigation needs. The average monthly water deficit and surplus presented was calculated with the following equation:

$$\pm \Delta W = P - ET_0$$

where P is the average monthly precipitation (mm/month), ET_0 is the average monthly reference or potential evapotranspiration (mm/month) and ± ΔW is the average monthly water deficit (-ΔW) or surplus (mm/month) (+ ΔW).

3.2.2 SPEI and NDVI

The Standardized Precipitation Evapotranspiration Index SPEI (Vicente-Serrano et al. 2010a) was used to identify meteorological drought and to assess the anomalies of precipitation, temperature, and evapotranspiration. Daily precipitation, daily temperature and other climatic data were collected from the Finnish Meteorological Institute (FMI). Reference evapotranspiration (ET_0 – also considered as potential evapotranspiration) was calculated by the ET_0 calculator software (FAO, 2009b), which calculates ET_0 using the FAO Penman-Monteith equation (Allen et al., 1998). The notation of Mustafa et al. (2017) was followed.

$$ET_0 = \frac{0.408\,\Delta\,(R_\mathrm{n} - G) + \gamma \dfrac{900}{T + 273}\, u_2 (e_\mathrm{s} - e_\mathrm{a})}{\Delta + \gamma(1 + 0.34 u_2)}$$

where ET_0 is the reference evapotranspiration [mm day^{-1}],

R_n is the net radiation at the crop surface [MJ m^{-2} day^{-1}],

G is the soil heat flux density [MJ m^{-2} day^{-1}],

T is the mean daily air temperature at 2 m height [°C],

u_2 is the wind speed at 2 m height [m s^{-1}],

e_s is the saturation vapour pressure [kPa],

e_a is the actual vapour pressure [kPa],

$e_s - e_a$ is the saturation vapour pressure deficit [kPa],

Δ is the slope vapour pressure curve [kPa °C^{-1}],

γ is the psychrometric constant [kPa °C^{-1}].

Monthly SPEI index values were introduced along with the monthly Normalized Difference Vegetation Index (NDVI) values that were produced using the Google Earth Engine (GEE) platform. Three Landsat NDVI imageries (i.e. Landsat 8, 7, 5) available from January 1984 until December 2020 were combined to interpolate missing values using Harmonic modelling techniques. The values were further analysed to detect the influence of SPEI over NDVI during the time interval observed.

3.2.3 Water Balance Simulation (WBS)

In this section, the basic assumptions used to develop the Water Balance Simulation (WBS) are presented. WBS provides the feasibility to simulate different lengths of crop growing seasons with a change in the number of days for each physiological stage of the potato crop. The crop growth period from 25 May to 25 September was considered as the longest possible crop growing season (124 days) in the field. The flowchart of the water balance simulation is shown in Figure 9.

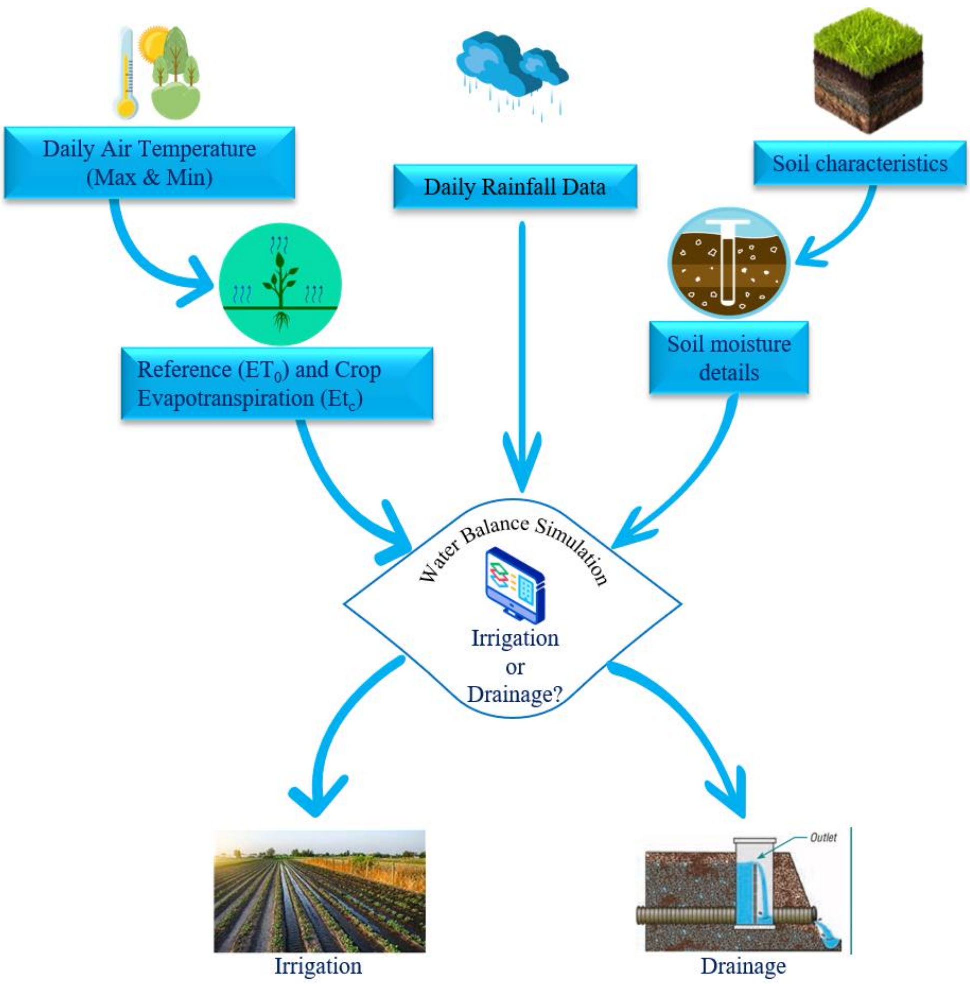

Figure 9: Flowchart of Water Balance Simulation (WBS)

Crop evapotranspiration (ET_c) is calculated as a combination of ground surface evaporation and the transpiration of water from the plant tissues (Andales et al., 2011). It can be estimated from potential evapotranspiration (ET_0) and crop coefficient (K_C) as follows:

$$ET_c = ET_0 * K_c$$

where ET_0 is estimated as follows:

$$ET_0 = 0.0023 * (T_{mean} + 17.8) * (T_{max} - T_{min}) * 0.5 * R_a$$

where T_{max} = daily maximum air temperature, (°C); T_{min} = daily minimum air temperature, (°C); T_{mean} = mean daily air temperature (i.e., average of T_{max} and T_{min}), (°C); R_a = extra-terrestrial radiation, (mm day^{-1}).

The daily values of extra-terrestrial radiation (Ra) are usually available in MJ m-2 day-1. The equivalent evaporation values in mm day-1 were obtained by the multiplication of Ra with 0.408 (Allen et al., 2007). Also, values of Ra vary with the location of the region under investigation on Earth. The following daily extra-terrestrial radiation values for the months of May to September were considered at 65° Latitude for the location of Tyrnävä (Table 1).

The K_C values vary with the plant growth and its physiological stages. The K_C values as mentioned in Figure 10 were considered to calculate the potato water requirement under different physiological growth stages under different scenarios.

We estimate the soil water storage using water retention curves (Figure 11).

Table 1: Daily extra-terrestrial radiation for different months at 65° Latitudes (MJ m-2 day-1)

Month	Daily extra-terrestrial radiation for the Month (Ra), MJ m^{-2} day^{-1}
May	35.8
Jun	41.3
Jul	38.8
Aug	29.7
Sep	17.9

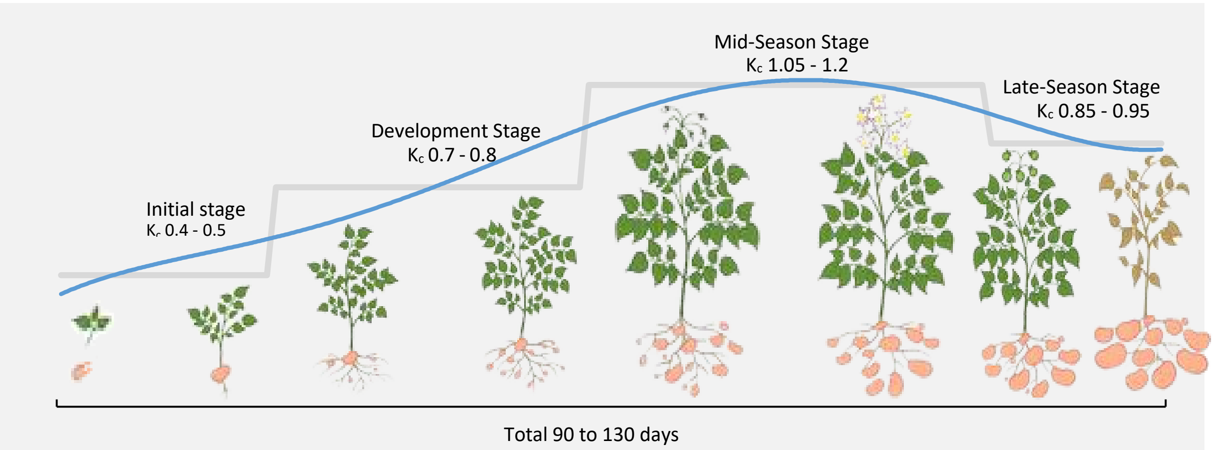

Figure 10: Range of Crop coefficient (K_c) considered for physiological growth stages of the potato crop

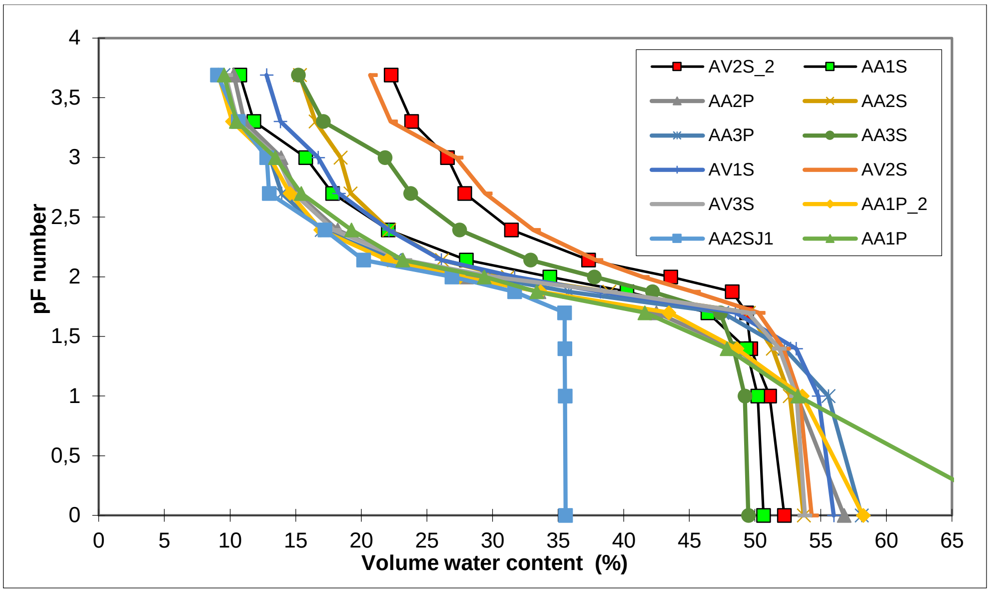

Figure 11: Soil pF Curve

Table2: Different soil (water holding) properties considered in the development of Water Balance Simulation (WBS)

Soil (water holding) properties	Details
Soil Structure	Silt clay
Depth of soil below ground level	1000 mm
Volumetric soil moisture content at Field Capacity (FC)	496 mm/m
Volumetric soil moisture content at Permanent Wilting Point (PWP)	250 mm/m
Available Water Capacity (AWC = FC - PWP)	346 mm/m
Maximum Allowable Depletion (MAD = 50% AWC)	173 mm/m
Initial Water Storage = FC	496 mm/m

The current setup of WBS calculates daily soil water storage (SWS) as follows:

$$SWS_{(t)} = SWS_{(t-1)} + P_{d_{(t)}} + ID_{(t)} - ET_{c_{(t)}} - DD_{(t-1)}$$

where $SWS_{(t)}$ = Soil water storage at time (t); $SWS_{(t-1)}$ = Soil water storage at time (t-1); $P_{d_{(t)}}$ = Average daily rainfall at time (t); $ID_{(t)}$ = Irrigation Demand in the field at time (t); $ET_{c_{(t)}}$ = Crop evapotranspiration at time (t); $DD_{(t-1)}$ = Drainage Demand in the field at time (t-1).

The Fraction available water (FAW) is:

$$FAW_{(t)} = \frac{(SWS_{(t)} - PWP)}{AWC}$$

where $FAW_{(t)}$ = Fraction available water at time (t); $SWS_{(t)}$ = Soil water storage at time (t); PWP = Soil water storage at time; AWC = Available water capacity,

and the soil water depletion (SWD):

$$SWD_{(t)} = SWS_{(t)} - FC$$

where $SWD_{(t)}$ = Soil water depletion at time (t); $SWS_{(t)}$ = Soil water storage at time (t); FC = Field capacity of soil.

In the end, the water balance situation in the field based on the crop water requirement or soil water storage conditions is:

$$If\ \left(SWD_{(t-1)} + ET_{c_{(t)}} + DD_{(t-1)} - P_{d_{(t)}}\right) > MAD$$

$$\text{Then, } ID_{(t)} = ET_{c_{(t)}} - P_{d_{(t)}}$$

where $SWD_{(t-1)}$ = Soil water depletion at time (t-1); $ET_{c_{(t)}}$ = Crop evapotranspiration at time (t); $DD_{(t-1)}$ = Drainage Demand in the field at time (t-1); $P_{d_{(t)}}$ = Average daily rainfall at time (t); MAD = Maximum Allowable Depletion; $ID_{(t)}$ = Irrigation Demand in the field at time (t) and:

$$If\ (SWD_{(t)} > FC$$

$$\text{Then, } DD_{(t)} = SWD_{(t)} - FC$$

where $SWD_{(t)}$ = Soil water depletion at time (t); FC = Field capacity of soil; $DD_{(t)}$ = Drainage Demand in the field at time (t).

3.3 Results

3.3.1 Annual water balance

The monthly average water balance calculation shows high evapotranspiration in summer months with a deficit in water (Figure 12). Evapotranspiration drops significantly during the winter months (first three and last three months of the year). From the month May onwards, monthly average potential evapotranspiration is larger than monthly average rainfall, therefore water deficit increases from this month on as shown in the figure (Figure 12). From the month of September, evaporation declines, water is in surplus and drainage is needed.

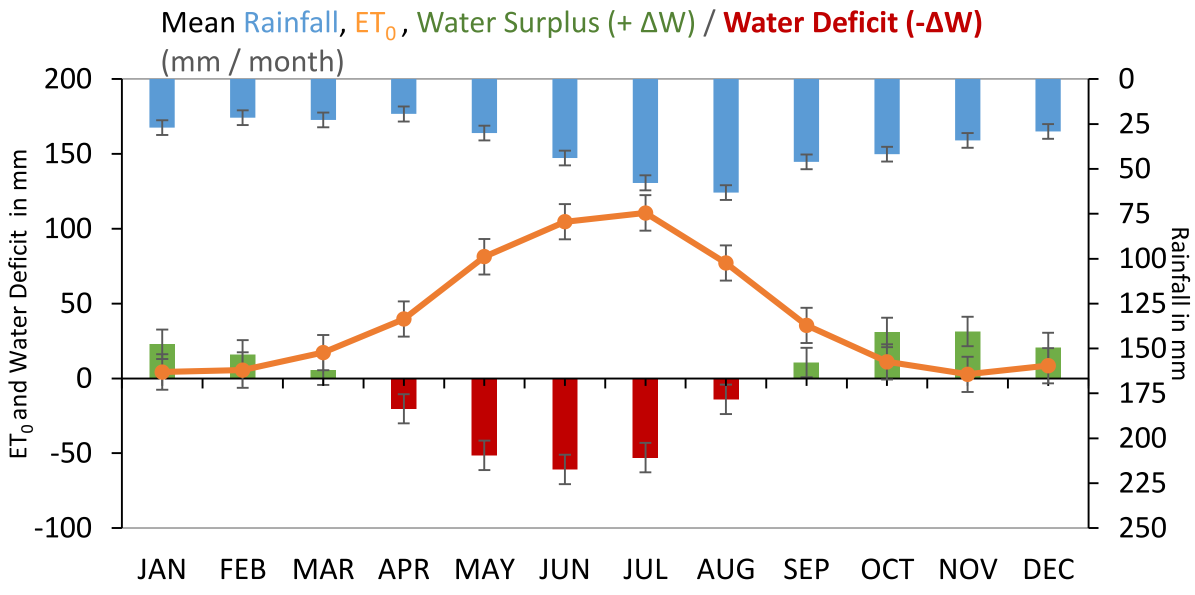

Figure 12: Average monthly water availability conditions in the Tyrnävä area

3.3.2 SPEI and NDVI

SPEI-based drought classification shows that there have been no extreme drought or wet periods observed in the region since 1984 (Figure 13). However, multiple severe and moderate droughts were observed and drought frequency (negative pulse of SPEI) has increased in the last decade.

Figure 14 shows the combined map of SPEI and NDVI. This chart reveals that severe drought occurring in the cropping season has a negative impact on NDVI values. For example, the lower NDVI values in 1992 and 1998 were caused by extreme and severe droughts in these years. Similarly, severe and extreme wet conditions during the cropping season also influence NDVI values negatively. For example, the lower NDVI value in 2004 was attributable to the extremely wet condition in that year. This indicates that supplemental irrigation would have been needed in 1992 and 1998 and drainage should have been provided for in 2004. Drought frequency has increased recently, therefore irrigation would have been advisable in 2018 and 2019. This means that the occurrence of wet and dry periods on the map displaying monthly SPEI and NDVI values also clearly indicates the intervals when there is a need for irrigation (e.g. 2006, 2018 and 2019) or drainage (e.g. 2004) (Figure 16). Year 2004 represents significant water surplus, whereas the period of 2018-2019 e.g. represents water shortage. Accordingly, both optimal irrigation and drainage management are essential to secure agriculture in this area.

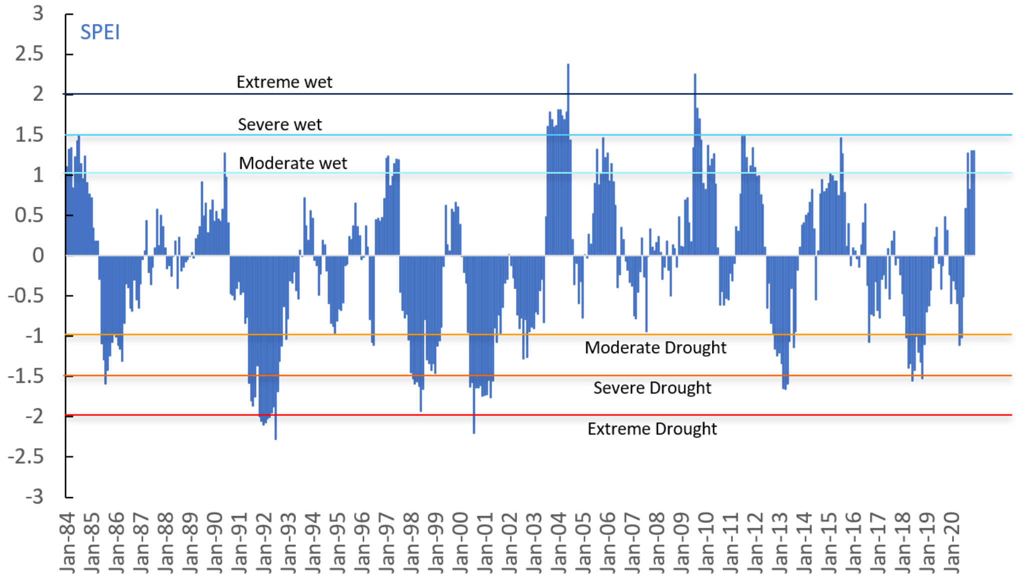

Figure 13: Monthly drought classification based on SPEI in Tyrnävä (1984-2020)

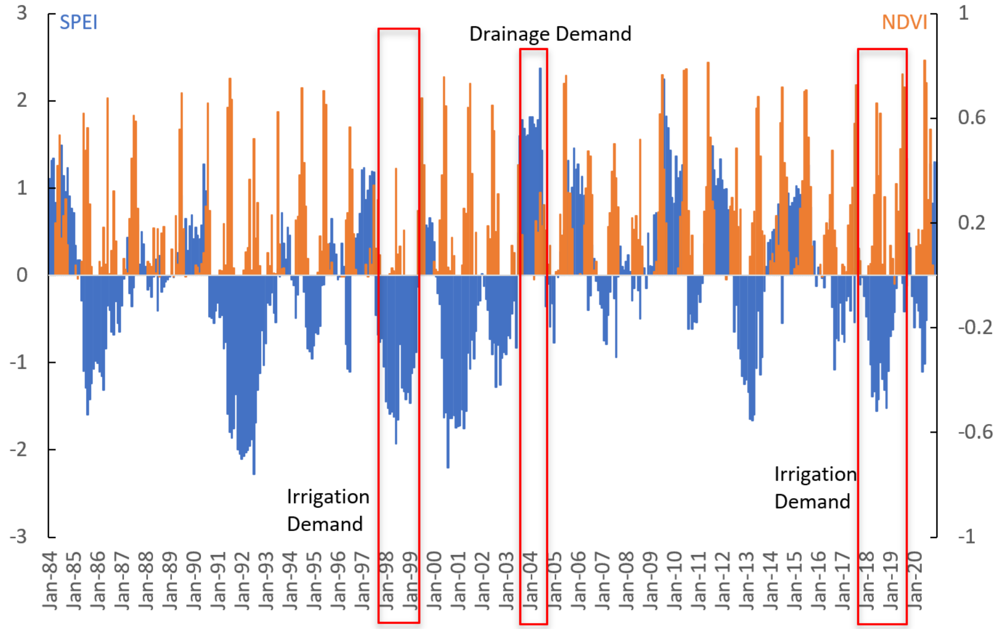

Figure 14: Water shortage analysis based on the comparison of SPEI correlated with NDVI

3.3.3 Water Balance Simulation (WBS)

Water balance simulation was used to estimate irrigation and drainage demand during cropping seasons from 2000 to 2020 (Figure 15). Based on WBS, irrigation was only required in 20% of the years (2003, 2006, 2018 and 2019), which indicates that drainage management is more important than irrigation in this area. The estimated volumes of irrigation demand for all crops in the field in years 2003, 2006, 2018 and 2019 were 2402, 7720, 963 and 807 m^3, respectively.

To provide a better understanding of irrigation demand during the dry years of 2003, 2006, 2018 and 2019 in more detail, daily WBS was also carried out (Figure 16). The demand for irrigation was observed to be the most substantial in August, during the mid-season stage of the potato, i.e. at the stage of flowering and complete crop yield development.

The WBS shows that the field required drainage during the crop growing seasons in 81% of the years (17 out of 21 years) (Figure 17). The volume of annual drainage varied between 0 to 9000 m^3 and mean annual drainage was about 2793.22m^3 (Figure 17). Therefore, a comparison between the results produced for irrigation demand (ID) (Figure 15) and drainage demand (DD) (Figure 17) in the study area indicates that the management of drained water is more crucial than irrigation.

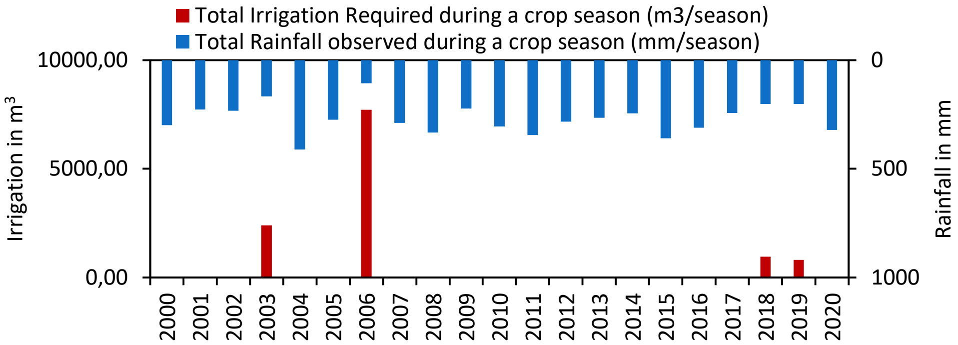

Figure 15: Total seasonal irrigation demand (ID) observed in the field from 2000 to 2020

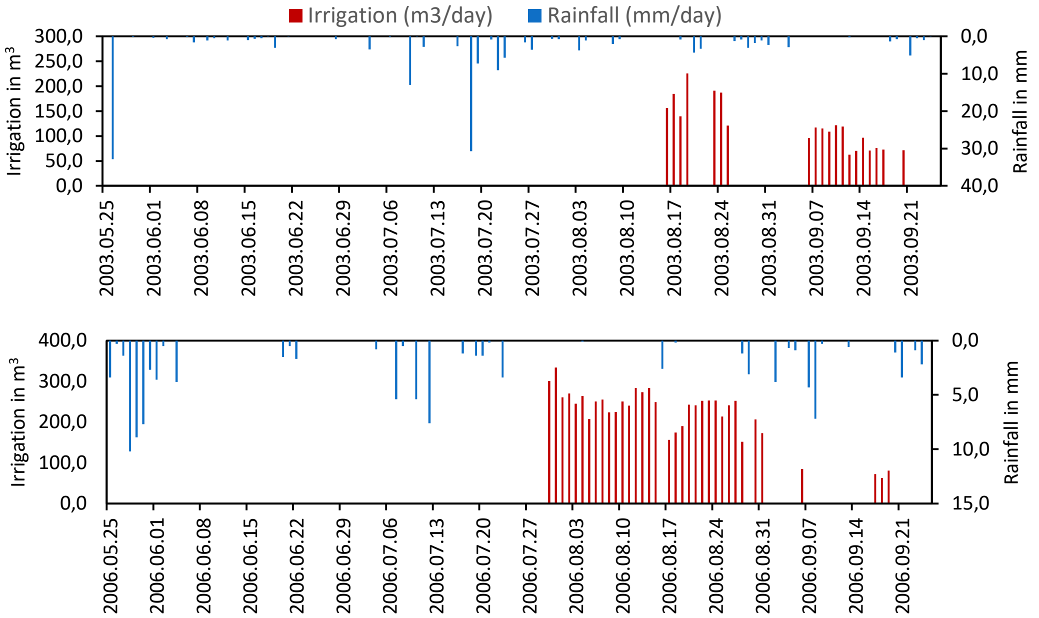

(a)

(b)

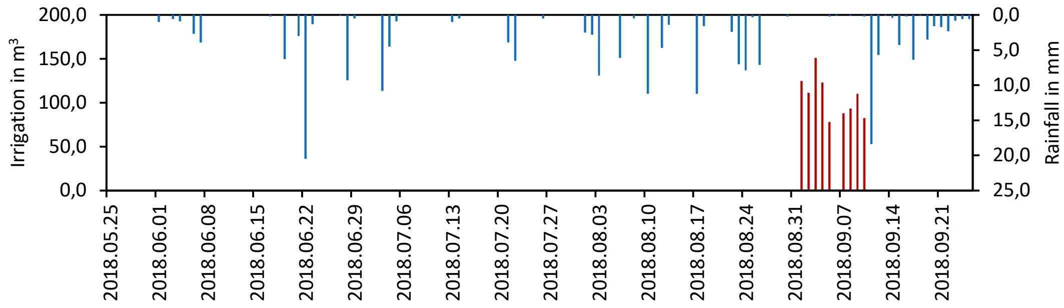

(c)

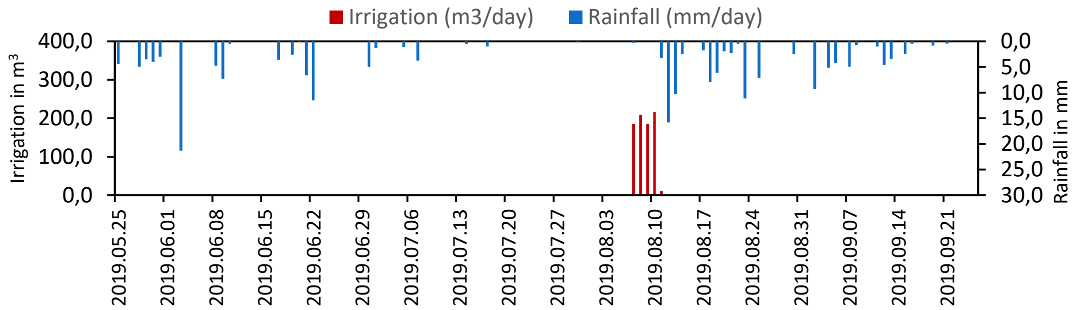

(d)

Figure 16: Daily irrigation demand observed in the field for the year of (a) 2003, (b) 2006), (c) 2018, and (d) 2019

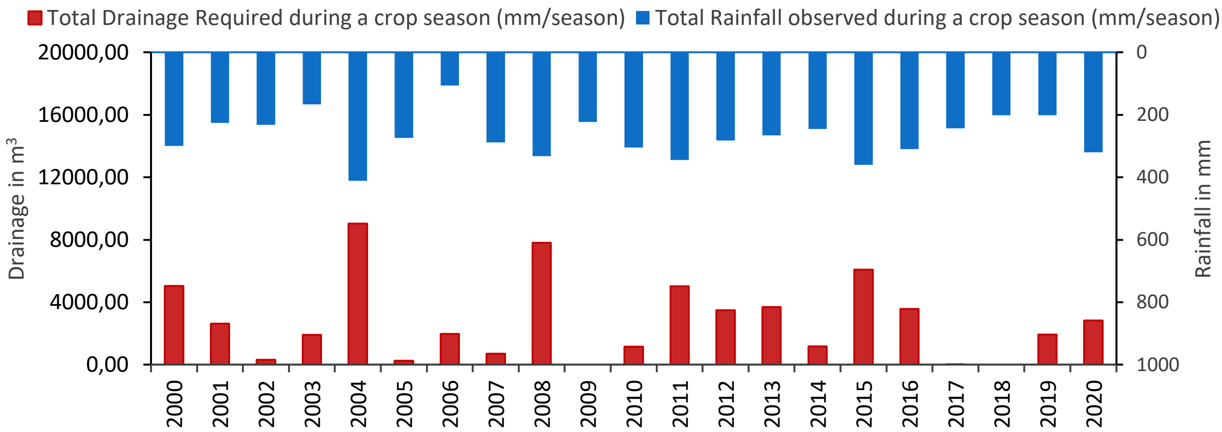

Figure 17: Total seasonal Drainage Demand (DD) observed in the field from 2000 to 2020

3.4 Discussion

3.4.1 Available water resources for irrigation

Based on WBS results, water surplus dominates over water deficit in Tyrnävä. The major source of surface water resource in the field *"Isosuo"* is the river Tyrnäväjoki. As shown in Figure 18, the river runs southwest of the field, at a distance of nearly 4-6 km (by road).

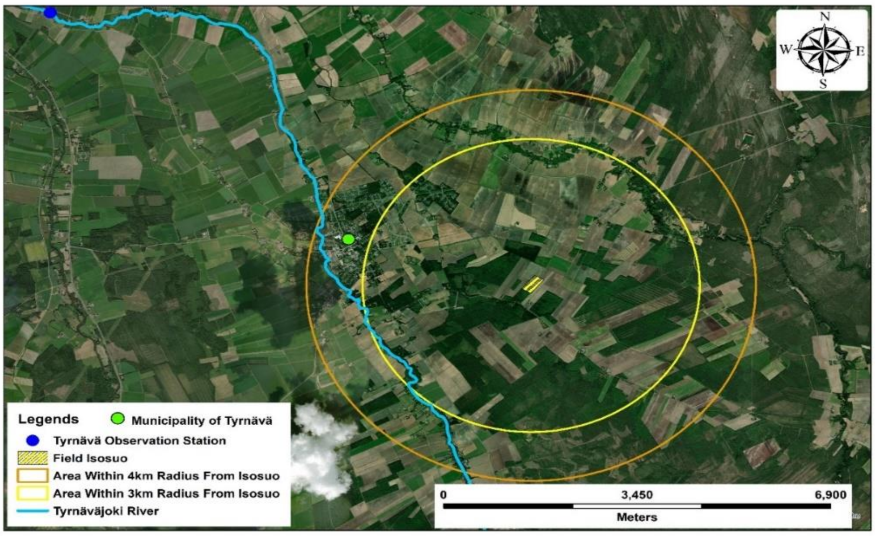

Figure 18: Available surface water resource y for the "Isosuo" field

In addition to the available surface water in the vicinity of the field, deep or shallow groundwater could also be an alternative for irrigation in the region, as an aquifer is found below the field. The field *"Isosuo"* is equipped with a controlled subsurface tile drainage system around 1 m below ground level to keep groundwater level below 1 m and provide proper soil-air environment for healthy crop root development and enhanced crop yield in the field.

The controlled drainage well in the drainage system can be raised or lowered to influence shallow groundwater level and soil moisture. In this way, groundwater levels can be managed under the field to provide soil water to the crop. The method is being tested in the Wateragri project. During summer drought periods, water availability in the field remains a major challenge.

In general, deep groundwater from aquifers is not used for irrigation in Finland, but farmers in the Tyrnävä and Liminka area are interested in the use of these water resources. Deeper groundwater could be an alternative for irrigation, but requires cost-benefit analysis and sustainability assessment. Long-term dependence on groundwater for irrigation may have significant adverse effects on environmental conditions, which also need to be taken into consideration.

3.4.2 Proposed alternative solution

At the moment, there are two controlled drainage wells operated on the north-western boundary of the study field. These wells control drainage from the field as a whole and when they are closed, drainage stops. In Wateragri, we considered the optimal use of these wells for irrigation. As an alternative method, we also investigate the possibility the collection of runoff water for later reuse for irrigation.

Figure 19 illustrates our proposed alternative solution to reuse drainage water for irrigation. The system will be assessed with an upgraded version of the currently discussed Water Balance Simulation (WBS) model, under different work packages of this project (to be discussed in future deliverables). We aim to reduce yield losses during summer drought and reduce the loading of nutrients into surface water by means of improved drainage control.

The application of controlled drainage is outlined in Figure 19. Rainfall and temperature data forecasted for days 1-10 are used as initial input. Forecasted temperature is used to estimate daily ET_0. Considering K_c (plant growth stage) and forecasted rainfall, soil moisture will be estimated using

WBS. After the running of the WBS, tentative irrigation or drainage demand values can be calculated, which will help farmers with implementing optimal irrigation or drainage management. For instance, if the field has sufficient water at the moment, but there is no rainfall forecasted for the next ten days, then, as discussed earlier in the report, farmers can raise the drainage system to keep soil moisture near to the root zone. On the contrary, if an extreme rainfall event is forecasted, drainage can be allowed by the lowering of the water level in the drains.

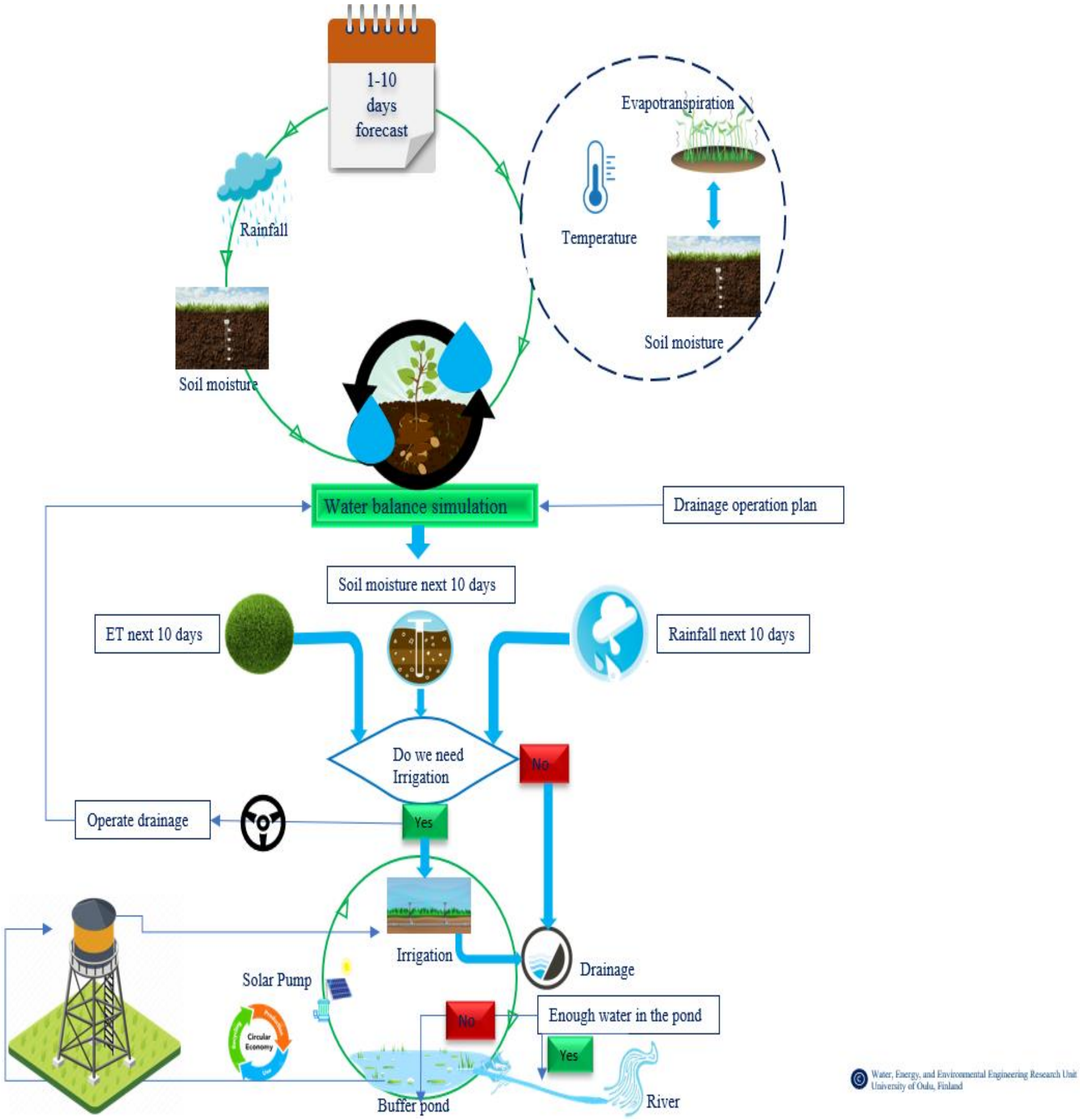

Figure 19: Smart water management solution for agriculture

In the proposed alternative solution, excess water drained during heavy rainfall could be stored in a buffer pond (constructed wetland) or an elevated storage tank. The drainage ditch beside the field would be used as a buffer pond with a V-notch or rectangular notch. During summer drought periods, the water stored in the buffer pond or elevated storage tank could be used for irrigation. This would also help overcome any possible uncertainty in the weather prediction. A solar pump could be applied to store drained water into an elevated tank. The water stored in the elevated tank could be used for irrigation by gravity flow. In this way, the proposed approach also promotes the circular economy in agricultural water management and optimizes the water-energy-food nexus.

4 Hydrological modelling to support irrigation

In WATERAGRI, several kinds of numerical models are part of the framework and used in the evaluation of WATERAGRI solutions. Certain numerical models are capable to solve complex water balance calculations and/or the flow field for a given hydrogeological setting considering various local conditions including water and land use scenarios. Choosing the best model often requires finding a balance between the problem to be solved, modelling needs and the data available. Depending on the problem at hand, model simulations are performed according to different principles and with consideration to various spatial and temporal scales. Hydrological models integrate meteorological data and responses in soils and catchments. These models can be based on physical laws, conceptual or entirely data driven. When dealing with nutrients or pollutant transport in general, pollutant characteristics must also be known, and models typically require information on substance reaction rates such as decay.

4.1 Hydrus-based modelling of water fluxes and root water uptake in a maize cultivated area of Nyírbátor for the development of precision irrigation scheduling

The Hydrus program is a finite element model for simulating the two- and three-dimensional movement of water, heat and multiple solutes in variably saturated media. The Hydrus program solves the Richards equation for saturated-unsaturated water flow and convection-dispersion type equations for heat and solute transport numerically. The flow equation incorporates a sink term to account for the water uptake by plant roots. The heat transport equation considers movement by conduction, as well as convection with flowing water.

4.1.1 Study site and description of the model

The Hungarian study area is situated in the Pannonian region, on the edge of a moderately warm and moderately cool climate belt, in the Norther Great Plain region in Szabolcs-Szatmár-Bereg county, next to the town of Nyírbátor (47°48'18.60"N, 22° 9'43.89"E). The case study site is located in a nitrate-sensitive area (based on European guidelines) and owned by the private company Bátortrade Ltd. The case study site is an irrigated arable land of 87.5 ha equipped with a linear irrigation system. The maize produced on the field is used to feed animals in the nearby farm. The case study site situated at the alluvial cone plain is covered mainly with quicksand. Nowadays, its active water network is sparse and the horizontal fragmentation of the landscape is low, due to melioration and drainage activities performed in the previous century.

The study area is situated on the edge of a moderately warm and moderately cool climate belt. The average number of yearly sunshine hours is between 1900 and 2000 (800 hours in the summer, 170 hours in the winter) based on National Weather Service data (www.omsz.hu). The average annual temperature is 9.6 °C and 16.6 °C for the summer half year. On the hottest summer days, the daily maximum temperature can exceed 34 °C. The average minimum temperature of the coldest winter days is below -17.0 °C. The annual rainfall is 570-600 mm, and there is about 350-360 mm rainfall in the summer half-year. The most common wind directions are northeast and southeast, with an average speed of 2.5 m/s. In summary, the climate of the Southeast Nyírség region is suitable for not very heat and water intensive agricultural crop production.

As part of our investigation, there was precision grid-based soil sampling carried out on an agricultural field (85.5 ha). Different databases and maps (for example Hungarian soil database, digital aerial photo archive, geological map by the Mining and Geological Survey of Hungary) were used to elaborate the soil sampling strategy (Figure 20).

Figure 20: Sampling strategy in the field

Core soil samples in two layers (30 cm and 60 cm) were taken at 102 points, representing 1.19 samples / ha on average. The soil texture of each sample was determined (> 2 mm, 200 µm - 2 mm, 50-200 µm, <50 µm), as well as soil water retention parameters like saturated water (SW), field capacity (FC), wilting point (WP), total available water content (TAW=FC-WP) and gravitational water content. The total available water in the upper layer (30 cm) is between 4.01-25.85 % with an average of 11.14±4.12 %. In the deeper layer, the total available water content is between 1.95-15.94 % with an average of 10.78± 4.55 % (Figure 21).

The aim of the model is to determine the water balance (WB) of the investigated area where maize is cultivated without any irrigation, alongside the cumulative water fluxes (WF) through the boundaries. The model considers a source term of water like precipitation (P) or irrigation (I) for the top (atmospheric) boundary of the domain, as well as a deep drainage boundary at the bottom. The length (x) and the width (y) of the transport domain are 2,200 m and 415 m, respectively (Figure 22), covering an area of 875,793 m^2 (~87.5 hectares).

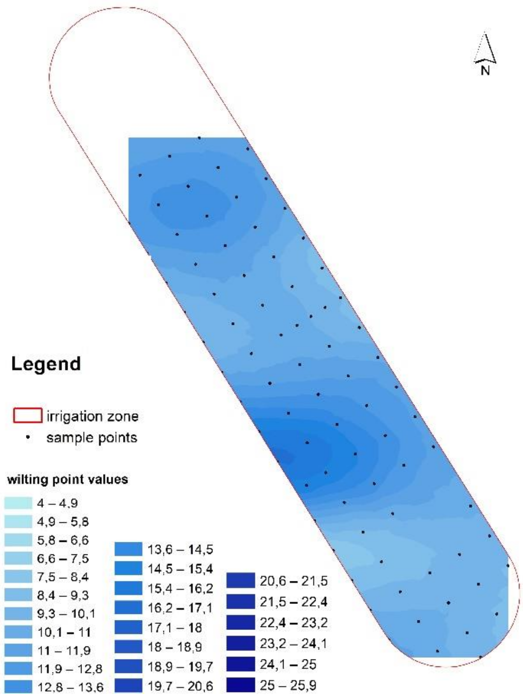

Figure 21: Total available water content (field capacity-wilting point) at the site in depth of 30 m

The depth (z) of the transport domain is 1 m. The soil physical properties previously measured and calculated in 2 different depths (30 cm and 60 cm from the soil surface). Hydraulic conductivity (k), water retention (Ψ_m), bulk density (ρ_B), particle density (ρ_p), particle size distribution (F(x)) and porosity (θ_p) are used as model input. The model also simulates root water uptake (RWU) and evapotranspiration (ET), including the theoretical crop-specific transpiration (ET_c) by maize. Based on the 3D soil physical model, water deficit (WD) can be calculated easily for the time period between 3 May 2020 and 10 September 2020 (from sowing to harvesting) in the modelled area of Nyírbátor.

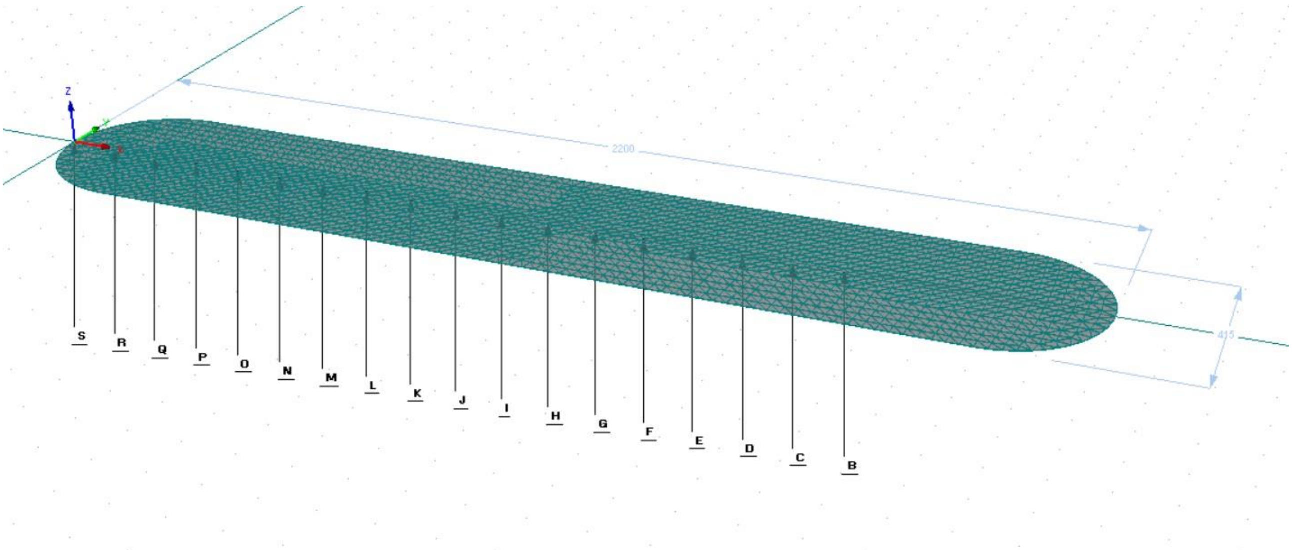

Figure 22: The generated finite element (FE) mesh of the model with the location of sampling rows (isometric view)

4.1.2 Setup and parameterization of the Hydrus model

Domain type and units – The 3D - general geometry was selected for this model.

Main processes and add-on modules – The following main processes were selected: water flow, solute transport and root water uptake. The solute transport module has not been activated yet (in the current model scenario, the solute concentration considered to be 0), however, our aim in the near future is to do an irrigation simulation where the solute transport of plant conditioners sprinkled with irrigation water could also be investigated.

Time information – The modelling timeframe is 131 days, elapsed from the sowing to the harvesting of maize (3 May 2020 – 10 September 2020), and the number of time-variable boundary records is also 131. Thus, there is a specified time-variable boundary record for each day over the investigated time period.

Soil hydraulic model – The van Genuchten-Mualem soil hydraulic model was used with no hysteresis. The shape of water retention curves can be characterized by several models (Buckingham, 1907), one of those most often used is the van Genuchten model (Eq. 1) (van Genuchten, 1980):

$$\theta(\psi)=\theta_r+\frac{\theta_s-\theta_r}{\left[1+(\alpha|\psi|)^n\right]^{1-\frac{1}{n}}}$$

where,

$\theta(\psi)$ is the water retention curve $[L^3 \cdot L^{-3}]$,
$|\psi|$ is suction pressure ([L]),
θ_s is saturated water content $[L^3 \cdot L^{-3}]$,
θ_r is residual water content $[L^3 \cdot L^{-3}]$,
α is related to the inverse of the air entry suction, $\alpha>0$ ($[L^{-1}]$ or $[cm^{-1}]$), and
n is a measure of the pore-size distribution, $n>1$ [-].

Based on this parametrization, a prediction model for the shape of the unsaturated hydraulic conductivity – saturation – pressure relationship can be developed.

Water Flow Parameters – The appropriate soil physical parameters were predicted based on the average values of the major soil physical properties measured in 2 different depths, such as particle size distribution, hydraulic conductivity and bulk density, with the Rosetta Lite v1.1. in-built module of the Hydrus software. The input data for the prediction are indicated in Table 3.

Table 3: The average results of major soil physical properties used in the Rosetta Lite v1.1. in-built module of the Hydrus software

Soil physical properties	Hydraulic conductivity, k $[m \cdot s^{-1}]$	Bulk density, ρ_B $[g \cdot cm^{-3}]$	Bulk density, ρ_p $[g \cdot cm^{-3}]$	Porosity, θ_p [V/V%]	USDA soil classification based on PSD analysis	
					Sand	Silt
Average (30 cm)	$2.886 \cdot 10^{-6}$	1.562	2.541	38.52	94.35%	5.65%
Average (60 cm)	$2.890 \cdot 10^{-6}$	1.577	2.558	38.32	95.60%	4.40%
Average total	$\mathbf{2.888 \cdot 10^{-6}}$	**1.569**	**2.550**	**38.42**	**94.98%**	**5.02%**

Root Water Uptake Parameters – The database of various crop types is included with the Hydrus software. From this database the *"Corn"* entity was selected (Wesseling, 1991). Table 4 indicates the parameters used to calculate the RWU parameters.

Table 4: The parameters used to calculate the actual value of RWU

Parameter	Value	Description
P_0	-0.15	Value of the pressure head [L] below which roots start to extract water from the soil (h_1).
P_{opt}	-0.3	Value of the pressure head [L] below which roots extract water at the maximum possible rate (h_2).
P_{2H}	-3.25	Value of the limiting pressure head [L] below which roots can no longer extract water at the maximum rate (assuming a potential transpiration rate of r_{2H}) (h_{3hight}).
P_{2L}	-6	As above, but for a potential transpiration rate of r_{2L} (h_{3low}).
P_3	-80	Value of the pressure head [L] below which root water uptake ceases (usually taken at the wilting point) (h_4).
r_{2H}	0.005	Potential transpiration rate [LT^{-1}] (currently set at 0.5 cm/day) (T_p).
r_{2L}	0.001	Potential transpiration rate [LT^{-1}] (currently set at 0.1 cm/day) (T_p).

Temporally Variable Boundary Conditions – Daily precipitation and ET_0 (reference evapotranspiration) values were calculated in external applications, and set up based on the measurements of a hydro-meteorological station (DavisMET) located nearby. The surface length associated with transpiration was 875,793 m^2 according to the geometrical parameters of the transport domain (Figure 23).

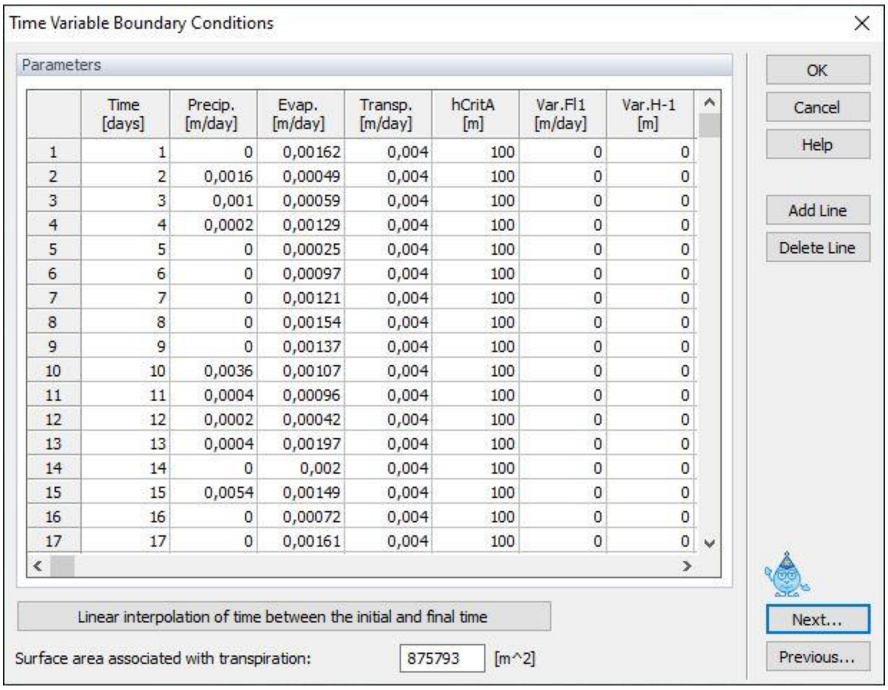

Figure 23: Time variable boundary conditions

The crop evapotranspiration (ET_c) was calculated based on the daily values of ET_0 (Allen et al., 1998) and K_c (crop coefficient). BBCH and LAI data provided by Vultus were used for the determination of K_c.

As a first step of the process, the entire period investigated was divided into 4 intervals with consideration to the crop development stages according to the suggestions of FAO (Allen et al., 1998). Table 5 summarizes the major parameters of the 4 development stages and their lengths for the year 2020.

Table 5: K_c and ET_c ranges according to the crop development stages

Stage	Indicators	Time period, T [days]	K_c range, [-]	ET_c range, [mm·day^{-1}]
Initial	Planting date (or the start of new leaves for perennials) to 10% ground cover	3 May 2020 – 13 June 2020	0.4-0.8	0.25-4.44
Crop development	10% ground cover to effective full cover, about 60-70% coverage for tree crops and 70-80% for field and row crops	14 June 2020 – 23 July 2020	0.8-1.2	1.06-6.34
Mid-season	Effective full cover to maturity, indicated by yellowing of leave, leaf drop, browning of fruit	24 July 2020 – 22 August 2020	1.2-0.9	0.93-5.78
Late-season	Maturity to harvest: the K_c value can be high, if the crop is irrigated frequently until fresh harvest or low, if the crop is allowed to dry out in the field before harvest	23 August 2020 – 10 September 2020	0.9-0.6	0.89-3.35

Figure 24 represents the parameters K_c, ET_0 and ET_c considering the crop development stages over the investigated time period. For the analysis of the temporal dynamics of the crop coefficient, the curve estimation procedure was used based on the data of the whole time period. The software Grapher 17 was used for the estimation of regression models. It was found that the K_c can be well described by a polynomial fitting ($Y=0.3116+0.0056 \cdot X+0.0002 \cdot X^2-2.0859 \cdot 10^{-6} \cdot X^3$; $R^2=0.95$).

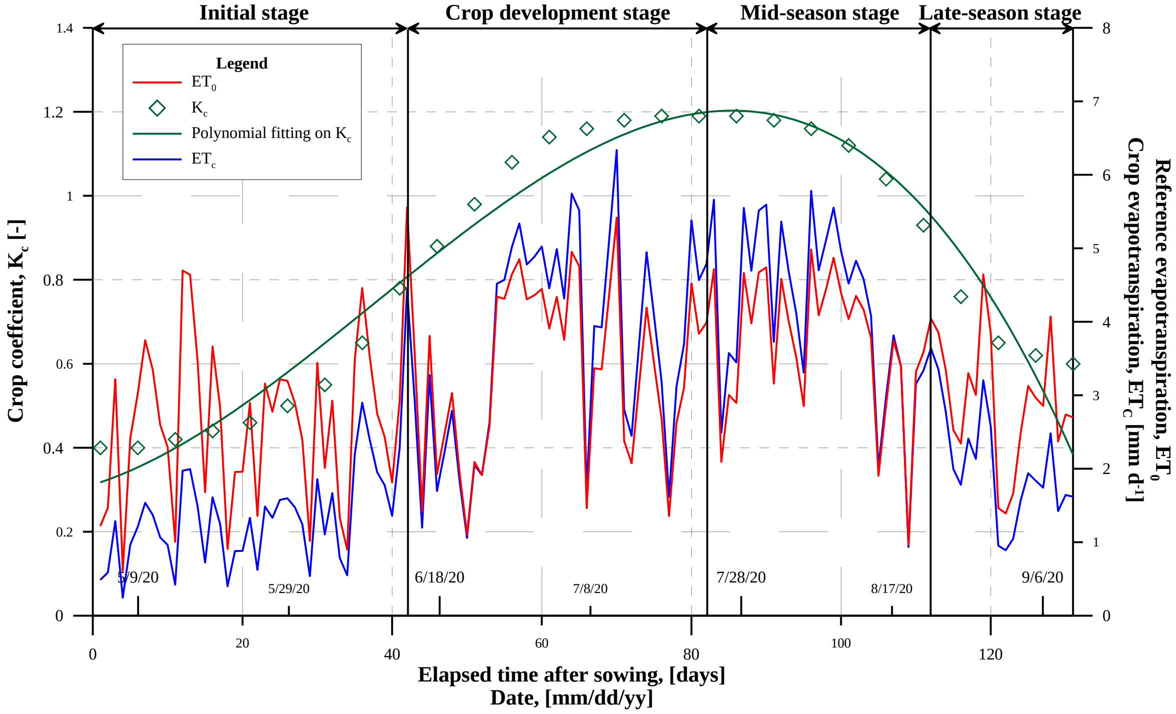

Figure 24: ET_0, K_c and ET_c as a function of elapsed time after sowing during the time period investigated

The peak value for the crop coefficient (K_c=1.2) can be observed around the boundary line between the crop development stage and mid-season stage 82 days after sowing, where the crop evapotranspiration value is 5.64 mm.

FE-Mesh parameters – The finite element mesh was generated by the unselecting of the automatic targeted FE size option and the using of 25.00 m instead.

Initial Conditions: Water Content – The initial water content was set up to field capacity according to the water retention curves measured and calculated for each sampling point.

Boundary Conditions – On the top of the simulation domain, an atmospheric boundary condition was applied, whereas on the bottom of the domain, a deep drainage condition was applied, corresponding to the groundwater level at 140 cm. Groundwater level data originated from a groundwater monitoring well, located at a distance of 1.9 km from the investigated area.

Validation of the model – The model validation was carried out for the first 65 days after sowing. Soil moisture data were collected from the Hungarian operational drought and water scarcity management system at the depth of 10 cm. The closest monitoring station (Nyírvasvári) was selected, which is located at 1.3 km from the cultivation area. There were some model modifications made, like the removal of the corn from the model, and the ET_c values were substituted with ET_0 values, so that the model and measured soil moisture content data could be compared (Figure 25). It is obvious, that there is a good correlation between the predicted and measured soil moisture content over the investigated time period (R^2=0.91), which means that the model built in Hydrus is applicable for modelling of water content changes at the case study site.

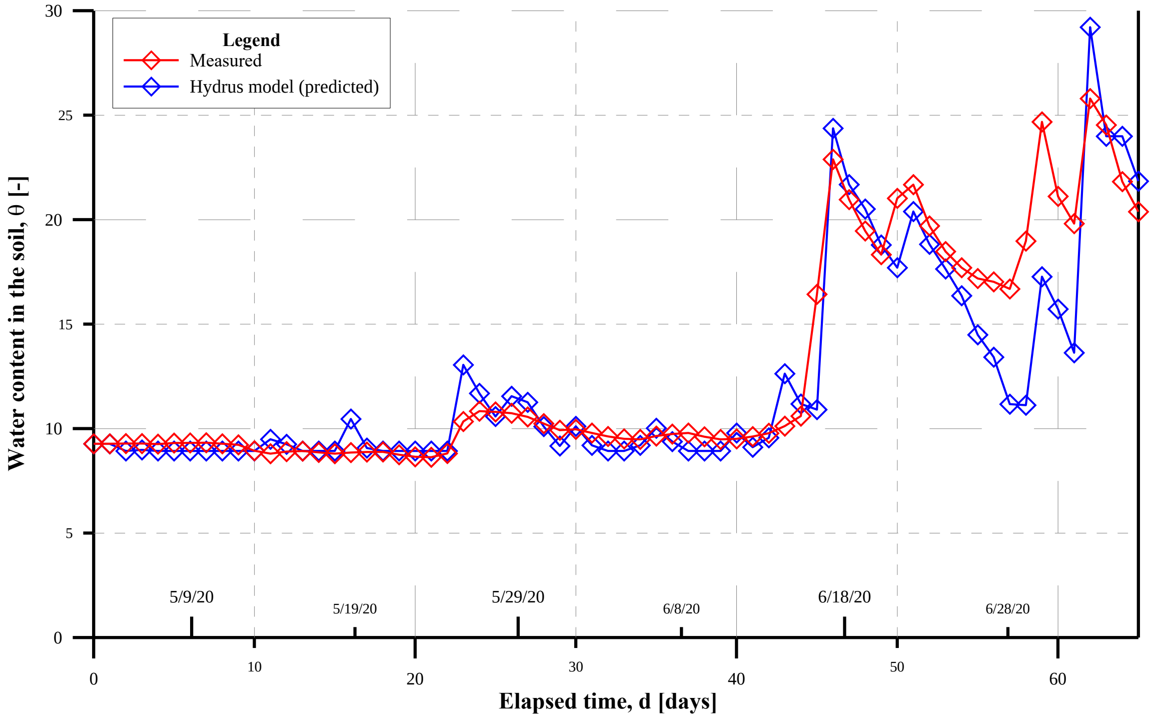

Figure 25: Measured and predicted soil water content for the period from May 3, 2020 to July 6, 2020 for the Hungarian site

4.1.3 Results of the model

4.1.3.1 Water content distribution in the soil as a function of time

In order to get a comprehensive view about the soil water content distribution of the area, the initial water content (field capacity) values were categorised, listed to 3 groups and marked with different colours (Figure 26).

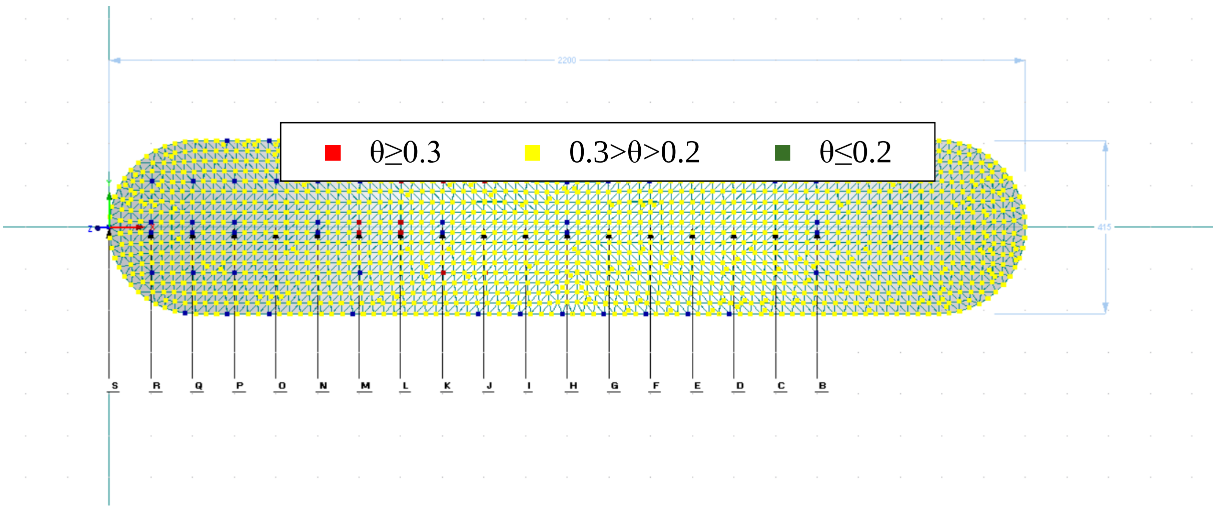

Figure 26: Initial soil moisture content (field capacity) ranges in the FE mesh nodes with the location of sampling rows

The average values related to the 3 initial water content ranges are:

- 30.54%, when $\theta \geq 0.3$,
- 24.87%, when $0.3 > \theta > 0.2$,
- 16.91%, when $\theta \leq 0.2$.

Using these 3 average initial water content values, the water contents have been predicted over the investigation period as a function of time. It can be seen in Figure 27, 28, 29 that if the initial water content is lower, the depletion of the water is faster in the soil. Moreover, all of the 3 average initial water content values reach the wilting point within 40 days without any irrigation and remain constant until the 10th of September 2020.

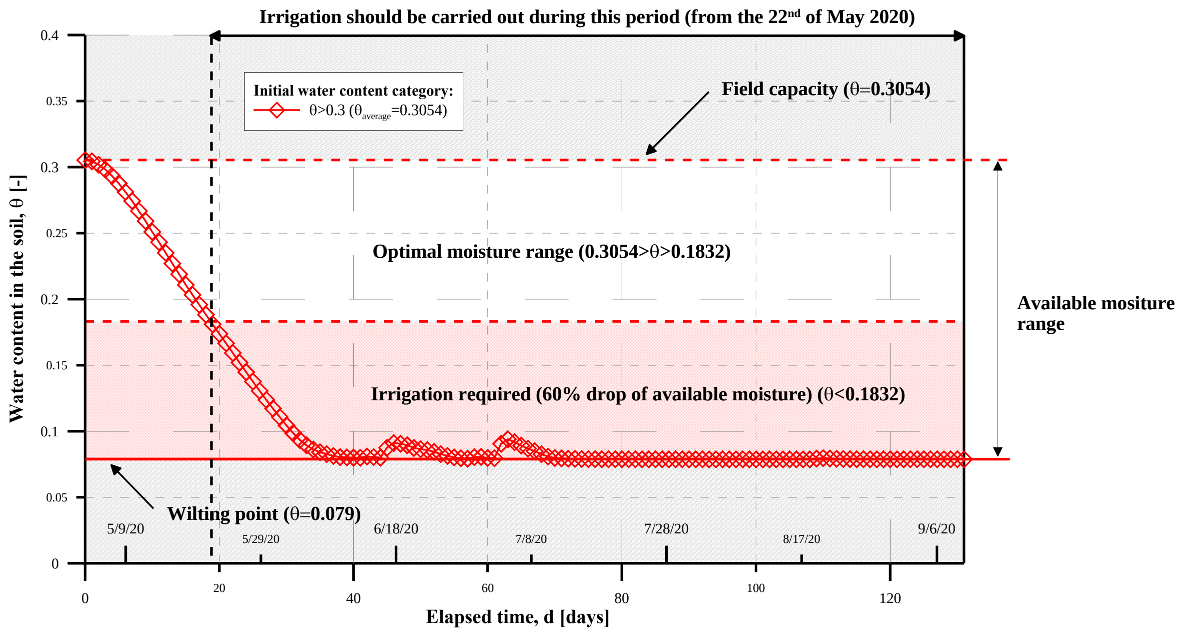

Figure 27: Water content in the soil as a function of time, when the initial soil moisture content is higher than 0.3 ($\theta_{average}$=0.3054)

The difference between the field capacity (30.54%, 24.87% and 16.91%) and the wilting point (7.9%) gives us the available soil moisture range, which is 22.64%, 16.97 and 9.01% considering the initial field capacity ranges. Based on practical experiences, irrigation should be carried out when the available moisture range drops to 60%, which corresponds to soil moisture contents of 18.32%, 14.92% and 10.15%, respectively.

The model results showed that irrigation should be carried out:

- from 22 May 2020, when the initial water content is higher than 0.3,
- from 16 May 2020, when the initial water content is between 0.2 and 0.3,
- from 12 May 2020, when the initial water content is less than 0.2.

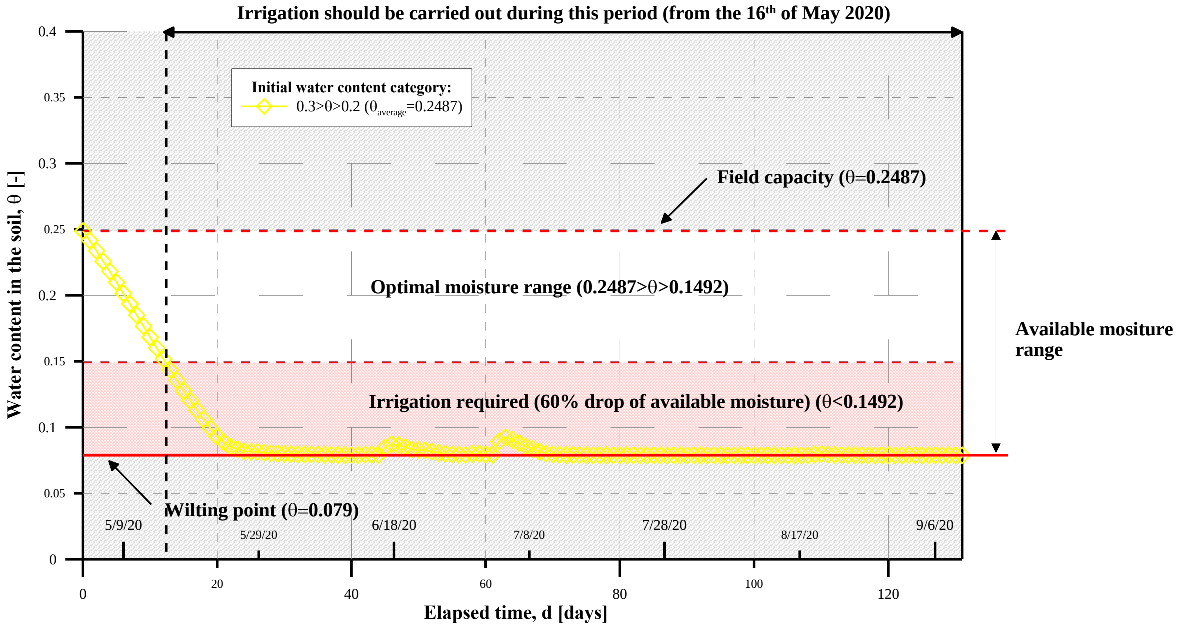

Figure 28: Water content in the soil as a function of time, when initial soil moisture content is between 0.2 and 0.3 ($\theta_{average}$=0.2487)

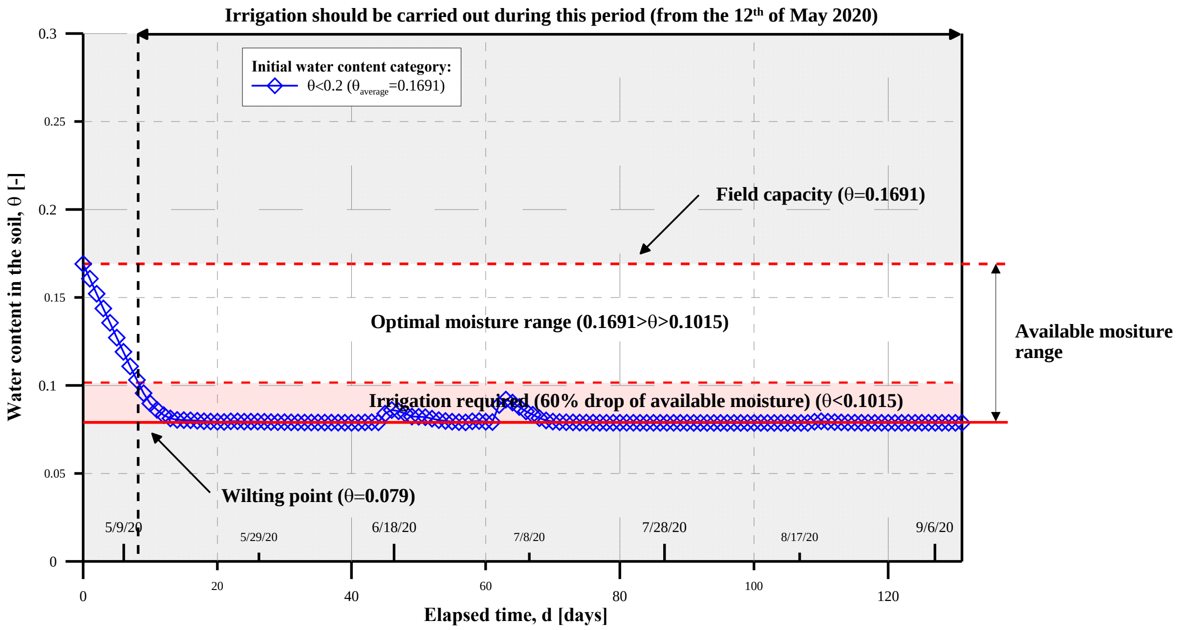

Figure 29: Water content in the soil as a function of time, when ϑ<0.2 ($\vartheta_{average}$=0.1691)

It can also be seen that incoming precipitation is not sufficient to supplement the water content in the soil to the optimal soil moisture range. Thus, it can be concluded that the water balance is negative in this area for all initial water content ranges.

4.1.3.2 Water fluxes through the boundaries (atmospheric and deep drainage) and the water balance as a function of time elapsed after sowing

In Figure 30, the water fluxes at the upper and lower model boundary are given as a function of time elapsed after sowing. After heavy precipitation events (e.g. 16 June 2020 – P=47.8 mm or 3 July 2020 – P=62.2 mm), elevated deep drainage can be observed in the model a few days after the heavy rainfall. Root water uptake increases as well, if a higher amount of precipitation is coming. The water balance is negative almost over the entire time period, except when precipitation level is high enough to balance it. Based on the hydro-meteorological data of the last year, the highest precipitation events occurred in the crop development stage, but evapotranspiration was also higher in this stage as a consequence of higher radiation and elevated temperatures.

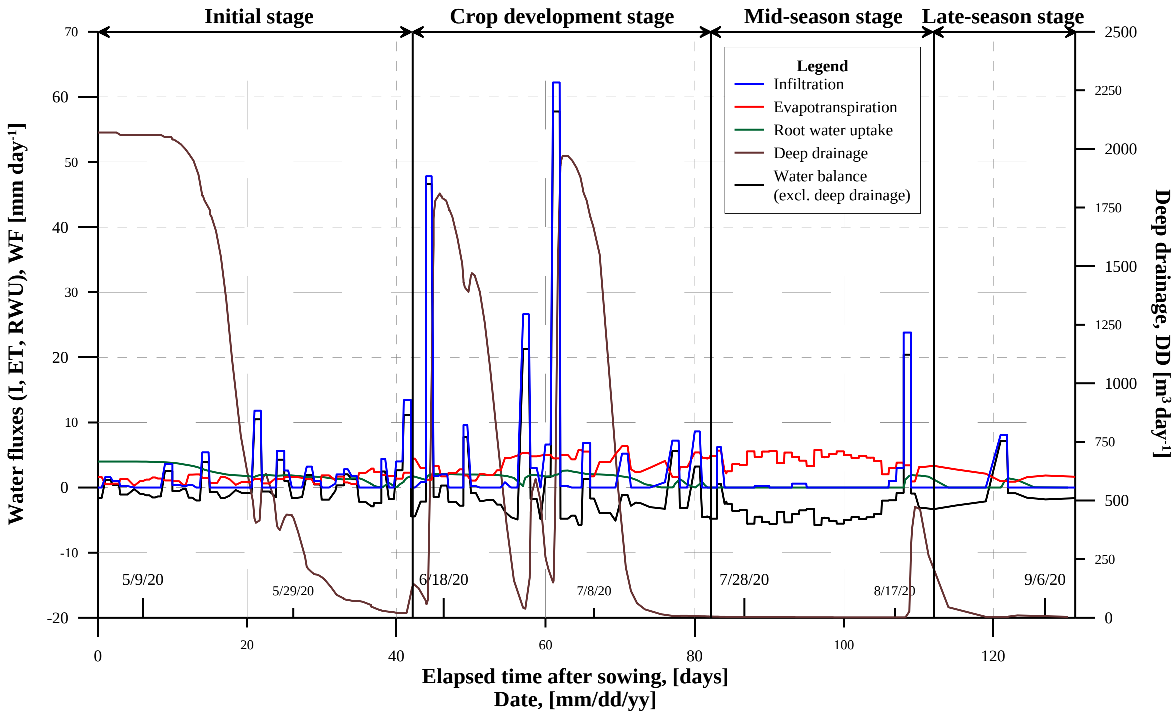

Figure 30: Water fluxes through the boundaries (atmospheric and deep drainage) and the calculated water balance

4.1.3.3 Cumulative water fluxes (atmospheric and deep drainage) and the water balance

Cumulative water fluxes are presented in Figure 31. Infiltration takes on positive values, because the incoming precipitation increases the water content in the soil. Deep drainage, evapotranspiration and root water uptake have negative values, because they decrease the water content in the soil. The so-called *"Atmospheric"* curve represents the balance between infiltration and evapotranspiration. By the end of the investigated time period, total infiltration was 267,000 m^3, while evapotranspiration, root water uptake and deep drainage totalled to 321,000 m^3, 145,000 m^3 and 72,000 m^3, respectively. Notice that ET includes RWU. Water balance can be calculated for the 87.5-hectare area from 3 May 2020 to 10 September 2020 in awareness of the exact values of these fluxes.

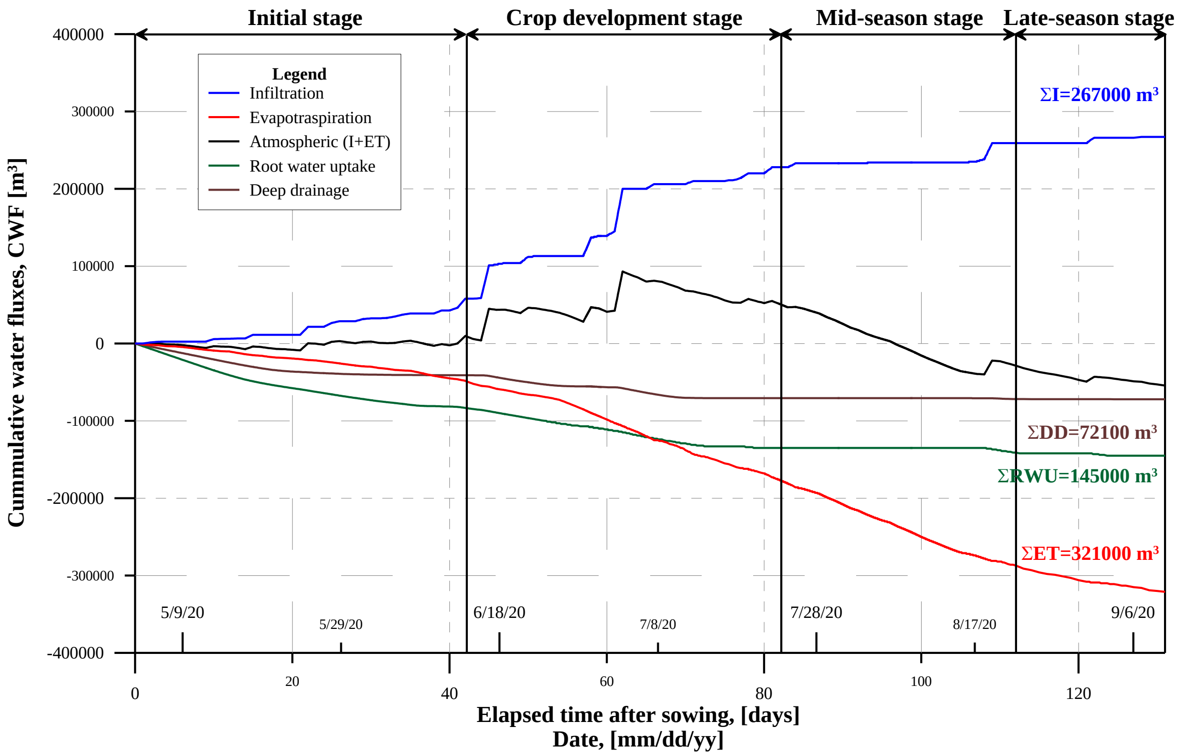

Figure 31: Cumulative water fluxes through the boundaries (atmospheric and deep drainage)

WB=I-(ET (includes RWU)+DD)

WB=267,000 m^3-(321,000 m^3+72,100 m^3)

WB=-126,100 m^3

In conclusion, the model results reveal a lack of 126,100 m^3 of water in the investigated agricultural land. Considering, that the area of the site is 875,793 m^2, the specific water deficit (WD) is 0.143 m^3/m^2, which is equal to 143.9 mm/m^2 or 143.9 l/m^2 or 1439 m^3/ha.

4.2 HydroGeoSphere based modelling

In contrast to simple conceptual water balance and 1-D soil column models, fully coupled and fully distributed surface water - groundwater flow models as employed in WP7 are capable of considering almost all components of the water cycle explicitly and in an integrated way. These models can be used to evaluate how drainage systems can be optimized, when and how much irrigation to apply, and how ideal soil moisture conditions for different crop types can be maintained. This can be achieved either through climate and land use change scenario simulations, which are essentially predictions into the far future, or through quasi-real-time modelling based on data assimilation, which allows the prediction of soil moisture or groundwater levels in an agricultural field to be predicted for two weeks ahead, similarly to short-term weather forecasts. That information can then be used by farmers to manage irrigation and drainage scheduling, but potentially also for estimations of crop development. In the case of ParFlow-CLM, predictions of carbon and nitrogen stocks, as well as crop yield could also be made, but these features are currently in a development phase (also within WATERAGRI). Different methods to test and improve model accuracy and reduce error exist, and they are typically part of the numerical modelling workflow meant to solve a practical problem. These form a principal part of WP7, for which the physically based and fully coupled surface water-groundwater-vegetation models are developed.

We shall report below on the current state of progress of the HydroGeoSphere based modelling for the Lower Silesia case study site. The state of progress will be illustrated on a simple climatic scenario analysis. The model will later be used for data assimilation experiments, which will allow real-time predictions of water availability and crop water demands. The results and outcomes of the modelling will be reported fully as part of the deliverables of WP7.

4.2.1 Study site and methods

4.2.1.1 The HydroGeoSphere Numerical Flow model

HydroGeoSphere (HGS) (Aquanty, 2021; Brunner - Simmons, 2012; Schilling et al. 2018) is a physically-based and fully integrated surface water – groundwater - vegetation flow model that has been successfully applied in many different hydrogeological contexts and at many different spatial and temporal scales. HGS can explicitly simulate the interactions between groundwater, surface water and vegetation under consideration of variably saturated subsurface flow and complex heterogeneous subsurface properties (e.g, Ala-Aho et al. 2017; Schilling et al. 2014, 2017; Tang et al. 2018). HGS can also consider fully explicit contaminant or nutrient transport, as well as irrigation and tile drainage in agricultural contexts (e.g., Bonton et al. (2012), De Schepper et al. (2017)). HGS has recently been coupled to the Weather Research and Forecast (WRF) model for the integrated simulation of atmosphere, surface, and subsurface interactions (Davison et al., 2015) and has been used for data assimilation experiments using the ensemble Kalman filter (EnKF) (Kurtz et al., 2017; Tang et al., 2017, 2018). As part of WP7, HGS will be coupled to the extremely powerful Parallel Data Assimilation Framework (PDAF) (Nerger et al., 2013), which will enable data assimilation with several state-of-the-art data assimilation algorithms. PDAF is also the data assimilation component of TerrSysMP-PDAF (Kurtz et al., 2016), which is the numerical model and data assimilation platform that is used by FZJ for the simulation of several other case study sites in WATERAGRI.

In HGS, the surface and subsurface are represented by two domains, the overland domain and the porous medium domain. All of the following information on HydroGeoSphere has previously been published in the HGS manual (aquanty.com), and is fully based on these sources (Schilling et al., 2018, 2020).

Surface water flow, i.e. flow within the overland domain, is represented with the following diffusion-wave approximation of the two-dimensional Saint-Venant equation:

$$\frac{\partial \varphi_o h_o}{\partial t} = -\overline{\nabla} \cdot d_o \mathbf{q}_\text{o} - d_o \Gamma_\text{ex} \pm Q_o$$

where $\overline{\nabla}$ is the two-dimensional differential operator, d_o [m] is the depth of surface water (excluding rill storage height that represents micro-topography), φ_o [-] is the surface flow equivalent porosity that accounts for microtopography, h_o [m] is the total head ($\equiv\ z\ +\ d_o$) for given water depth d_o and elevation z, $\mathbf{q}_\text{o}$ [m/d] is the average surface water flow velocity, Γ_ex [m/d] is the volumetric rate of fluid exchange between the surface and subsurface domains per unit surface area (positive when water flows from the surface to the subsurface), and Q_o [(m^3/d)/m^3] represents sources and sinks (volumetric flux per unit surface area). The surface flow equivalent porosity ranges between 0 and 1, depending on whether the depth of surface water is below or above the micro-topography.

The average surface water flow velocity $\mathbf{q}_o$ is given by:

$$\mathbf{q}_o = -\mathbf{K}_o \cdot k_{ro} \nabla (h_o)$$

where k_{ro} is a dimensionless factor accounting for obstructed flow and microtopography, and $\mathbf{K}_o$ [m/d] is the surface conductance that is solved using Manning's equation.

Irrigation is simulated in HGS by the alignment of the numerical grid during mesh generation with irrigation infrastructure, e.g. drip irrigation piping, and by the subsequent specification of representative irrigation water fluxes [m^3/d] via second-type (Neumann) boundary conditions at discrete model nodes located within the surface domain.

Variably-saturated groundwater flow in HGS is simulated using Richards' equation:

$$\frac{\partial}{\partial t}(\theta_s S_w) = -\nabla \cdot \mathbf{q} + \Gamma_{\text{ex}} \pm Q_o$$

where θ_s [-] is the saturated water content, S_w [-] is the water saturation, $\mathbf{q}$ [m/d] is the groundwater flux (i.e. Darcy flux), and Q_o [(m^3/d)/m^3] represents sinks and sources (volumetric flux per unit volume).

The groundwater flux $\mathbf{q}$ is given by:

$$\mathbf{q} = -k_r(S_w)\mathbf{K} \cdot \nabla(\psi_w + z)$$

where $k_r(S_w)$ [-] is the relative permeability of the medium, $\mathbf{K}$ [m/d] is the saturated hydraulic conductivity tensor of the porous medium, and ψ_w and z [m] are the pressure and the elevation head, respectively. Surface water flow and groundwater flow equations (i.e., the overland and the porous medium domains) are fully-coupled with the dual-node approach (de Rooij, 2017) and solved simultaneously, without requiring iteration. The relationship between the relative permeability of the porous medium, the soil water content and pressure can be given in tabular form or parametrized using the van Genuchten functions (van Genuchten, 1980).

According to the approach of van Genuchten (1980), the saturation S_w is related to the matric suction ψ and the relative permeability k_r by:

$$S_w = \begin{cases} S_{wr} + (1 - S_{wr})\left[1 + |\alpha\psi|^{\beta}\right]^{-\upsilon}, & \psi < 0 \\ 1, & \psi \geq 0 \end{cases}$$

$$k_r(\psi) = S_e^{(l_p)}[1 - \left(1 - S_e^{1/\upsilon}\right)^{\upsilon}]^2$$

$$S_e = (S_w - S_{wr})/(1 - S_{wr})$$

where S_{wr} [-] is the residual saturation, α [L^{-1}] and υ [-] are the van Genuchten parameters, υ is given as $1 - {}^{1}/_{\beta}$ with $\beta > 1$, S_e [-] is the effective saturation and l_p [-] is the pore-connectivity parameter (which is 0.5 for the van Genuchten model).

Evapotranspiration is modeled as a combination of evaporation and transpiration, affecting both the surface and the subsurface. Transpiration T_p [LT^{-1}] is simulated based on the implementation of Kristensens and Jensen (1975):

$$T_p = f_1(LAI)\, f_2(\theta)\, RDF\, [E_{pot} - E_{canopy}]$$

$$f_1(LAI) = \max\{0, \min[1, (\mathrm{C}_2 + \mathrm{C}_1 LAI)]\}$$

where *LAI* [-] is the leaf area index, θ [-] is the soil moisture content, *RDF* [-] is the root decay function, E_{pot} [LT^{-1}] is the potential evapotranspiration, E_{canopy} [LT^{-1}] is interception and canopy evaporation, and C_1 [-] and C_2 [-] are coefficients which express the relation of transpiration on LAI. C_1 allows accounting for transpiration limiting vegetation characteristics (e.g., height, development stage, age of vegetation, degradation) and C_2 for transpiration from vegetation for which LAI can't be defined. The *RDF* describes the decrease of root density with depth. $f_2(\theta)$ takes on values between zero and one according to:

$$f_2(\theta) = \begin{cases} 0, & 0 \le \theta \le \theta_{wp} \\ f_3, & \theta_{wp} \le \theta \le \theta_{fc} \\ 1, & \theta_{fc} \le \theta \le \theta_{ox} \\ f_4, & \theta_{ox} \le \theta \le \theta_{an} \\ 0, & \theta_{an} \le \theta \end{cases}$$

$$f_3 = 1 - \left[\frac{\theta_{fc} - \theta}{\theta_{fc} - \theta_{wp}}\right]^{\mathrm{C}_3}$$

$$f_4 = 1 - \left[\frac{\theta_{an} - \theta}{\theta_{an} - \theta_{ox}}\right]^{\mathrm{C}_3}$$

Below the wilting point θ_{wp} [-], transpiration is zero, maximum transpiration is reached between the field capacity θ_{fc} [-] and the oxic limit θ_{ox} [-], and if the soil moisture content is above the anoxic limit θ_{an} [-], root stress is so high that transpiration is again 0 (Feddes - Raats, 2004). C_3 [-] is a fitting parameter with a recommended value of 1, making the ramping functions f_3 and f_4 linear (Feddes et al., 1978; Panday - Huyakorn, 2004).

Agricultural drainage infrastructure such as tile drains can be simulated in HGS in an efficient manner using so-called 1-D pipe elements, which circumvents the computationally intensive calculations that would be necessary if drainage flow were considered explicitly as part of the variably saturated subsurface porous medium flow domain. Instead, drainage flow in tile drains is simulated using the efficient one-dimensional Hazen-Williams equation (Aquanty, 2021). This, however, requires that the numerical grid is aligned with the drainage infrastructure already during mesh generation, such that the specification of the 1-D drainage network is possible via discrete model node selections.

4.2.1.2 Case study site and model

There were several case study sites selected for the fully coupled and physically based modelling experiments within WATERAGRI. For an assessment of irrigation water demand under different climatic and agricultural land use scenarios, the agricultural case study site in Lower Silesia, Poland was selected (case study site 5.7). The Lower agricultural case study site is located in South-West Poland around the village of Lubnów, which is approximately 20 km north of Wrocław. In hydrological terms, the farm studied is located on the border of 2 different hydrological catchments. However, as 90% of the area of the farm is located in the Lubnówka River catchment, only the Lubnówka River catchment was considered for the fully coupled and physically based modelling experiments. The Lubnówka River is a tributary to the Odra River, which is Poland's second largest river. The entire surface area of the said catchment is 17.4 km^2, but, for modelling purposes, the catchment was limited to the 14.6 km^2 located upstream of the official limnigraph (roughly 500 m upstream of where Lubnówka River joins the Odra River). According to the climate classification by Okołowicz (1977), the climate of the catchment is temperate warm transitional. The Lubnówka River catchment modeled is illustrated below in Figure 32.

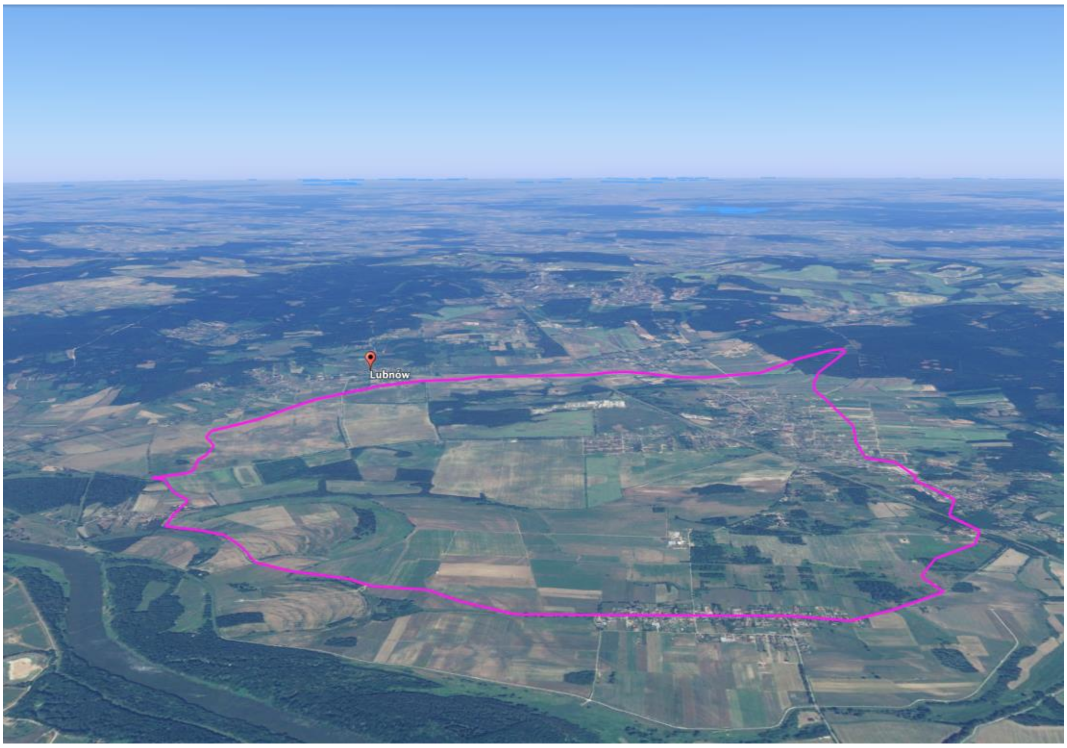

Figure 32: Lubnow River catchment outline and location of Lubnow village (Image source: Google Earth)

Mean annual precipitation at the study site, measured over the period 1991-2020, was 541 $\pm$ 95 mm. Mean air temperature over the same period was 9.7 $\pm$ 1 °C. With an average depth to groundwater of 1-2 m, a significant amount of groundwater resides in the shallow aquifer of the study site. According to the information obtained from 20 boreholes, the shallow aquifer is limited underneath by impermeable bedrock sitting at a depth of 2-5m, depending on the location within the catchment. The topsoil consists of loamy sand, clay and silt on 80%, 5% and 15% of the catchment area, respectively. Below 3-3.5m, the subsurface consists primarily of clay.

In November 2020, 4 piezometers and 4 soil moisture measurement stations were installed in the catchment subject to the study. The soil moisture stations measure soil moisture within the top 80cm of the soil, at 10cm intervals. As mentioned above, an official limnigraph is located at the outlet of the catchment, alongside an official meteorological measurement station.

4.2.1.2.1 Flow model setup and parametrization

The currently used numerical model grid consists of an approximately equilateral triangular mesh with 18’608 nodes and 36’948 elements of variable sizes, with higher resolution along agricultural drains and ditches and lower resolution on agricultural fields (Figure 33). Vertically, the model was discretized into 16 layers employing proportional sub-layering, whereby each of the top 10 layers was set to cover 2.5% of the total vertical extent of the model at any location, and the bottom 6 layers to cover 12.5% each. This fine vertical discretization in the top 25% of the model guarantees a numerically accurate simulation of variably saturated flow processes as required by Richards’ equation (Downer and Ogden, 2004).

The 3-D numerical grid is illustrated below.

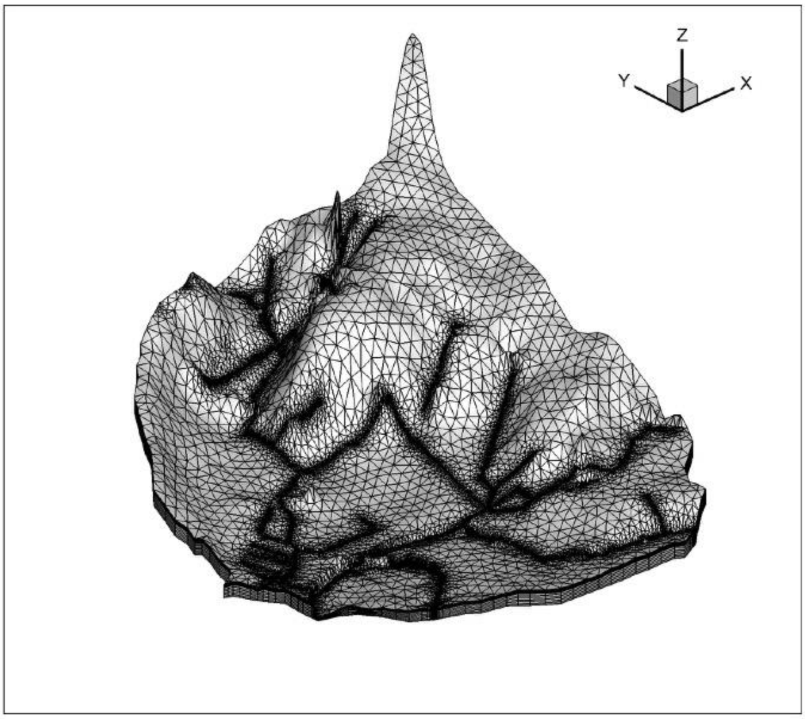

Figure 33: Numerical grid for the Lower Silesia case study site as currently implemented in HGS. The numerical grid is vertically exaggerated for a better visual presentation of elevational gradients and the location of ditches

For these illustrative scenario analyses, only the shallow aquifer was simulated, and the model was set to consist of sandy gravel using typical values after Li et al., (2008) and Dann et al. (2009) ($\mathbf{K}$ = 5.4 m/d; porosity = 0.46; α = 3.48 m^{-1}; β = 1.75, S_{wr} = 5%). The lower and lateral boundaries of the model were set impermeable, except for the downstream lateral end of the model, which was simulated as the outflow boundary and implemented as a critical depth boundary condition. As actual evapotranspiration was directly subtracted from actual precipitation prior to forcing the model with precipitation, vegetation was not explicitly simulated in these illustrative examples. The integration of more detailed subsurface parametrization, the explicit simulation of variable vegetation cover and transient model calibration via history matching or data assimilation are part of the outputs of WP6 and WP7 and will be implemented later during the project.

4.2.1.2.2 Simulated climatic scenarios

With a view to illustrating the current state of progress of the fully integrated and physically based surface water-groundwater model of the Lower Silesia case study site and to demonstrating the capability of the model to allow an estimation of irrigation water demands later in the progress of the WATERAGRI project, the existing model was used to simulate 3 key meteorological scenarios: the year which reflects the annual average precipitation as measured between 1991 and 2020 most closely (2005; 544.5 mm of precipitation), as well as the driest (2015; 388.2 mm of precipitation) and the wettest (2020; 736.5 mm of precipitation) year during the same reference period.

Simulations were run for a full 365-days period, driven by daily sums of precipitation as measured during the respective years. As remote sensing based high resolution maps of vegetation cover will only become available for the Lower Silesia case study site later during WP3/the WATERAGRI project, evapotranspiration was not explicitly simulated and the actual measured daily evapotranspiration was subtracted instead from the actual measured daily precipitation prior to forcing the model. Winter hydrological processes, i.e. snowfall and snowmelt, were not explicitly considered and all precipitation was simulated as rain.

4.2.2 Scenario comparison

Illustrations of the subsurface saturation of the numerical model under the three scenarios are presented in Figure 34.

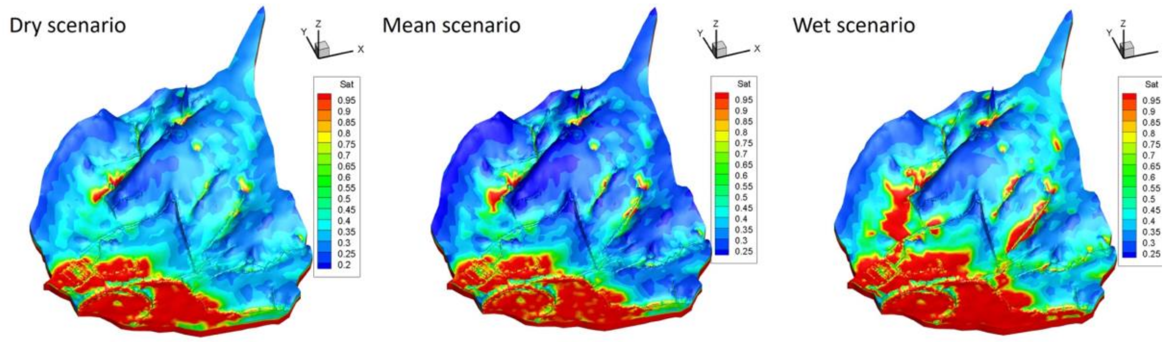

Figure 34: Comparison of subsurface saturation in the catchment on an arbitrarily chosen day (day No. 200 = 18 July)

While the lower part of the catchment is generally saturated and water levels are close to the surface in all three scenarios, the saturation state varies more in the upstream parts. However, while the wettest year exhibits strong accumulation of water in topographic depressions even in the upstream parts, the driest and the mean scenarios do not differ much in the upstream parts. This illustrates the fact that real yearly records were simulated, which, even though they may differ in the total precipitation that has fallen during a year, may also differ significantly in their evapotranspiration. In the Lower Silesia study area, for example, dry years do not correspond with years of large precipitation, and vice versa, wet years do not correspond with years of low evapotranspiration. Nevertheless, as visible in the monthly water balances of the three scenario years, illustrated below

(Figure 35), over an entire year a clear decline in the discharge of Lubnówka River and net groundwater recharge from wettest to driest year can be seen. With near zero precipitation and therefore zero net recharge during the driest months of the dry scenario, one can expect strongly increased demand for irrigation water compared to the mean and the wettest scenarios.

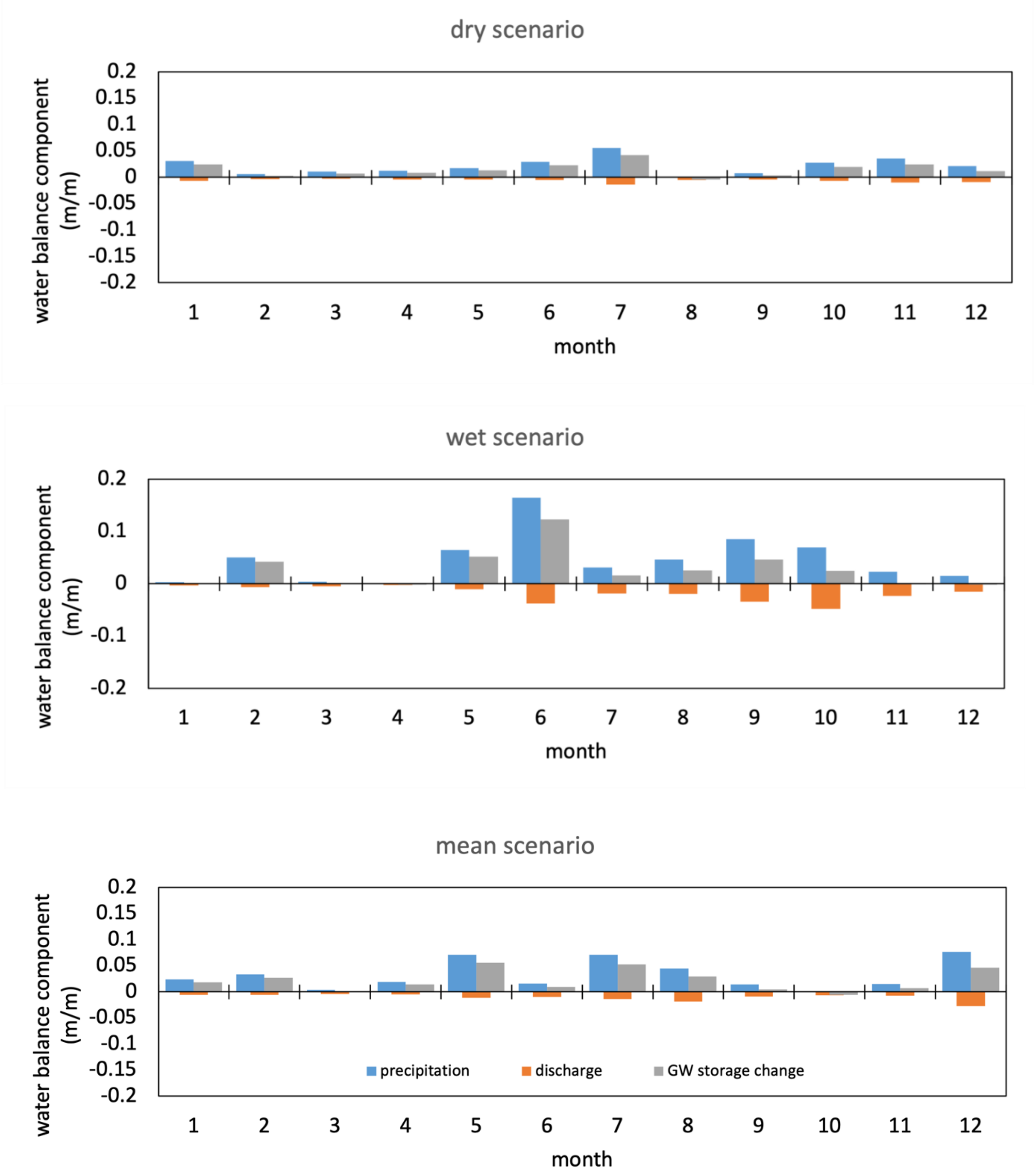

Figure 35: Comparison of monthly water balances of the three simulated scenarios. Illustrated are precipitation, discharge at the catchment outlet, and groundwater (GW) storage changes. Positive groundwater storage changes indicate net recharge, whereas negative GW storage changes indicate net GW exfiltration. Note that these numbers are indicative and expected to change with the upcoming refinement of the model.

4.2.3 Outlook

The preliminary results presented herein describe the current state of progress of the physically-based, 3D surface water-groundwater-vegetation modelling that represents the basis of the modelling for WP6 and 7. By showing the current state of progress of the Lower Silesia study site model, we aimed to demonstrate how the model is able to represent all important components of the water cycle in an integrated and physically explicit way. In a next step, we are going to include detailed soil maps, land use information and vegetation cover from the WATERAGRI remote sensing pipeline in order to improve the model's ability to represent the study site. Once fully set up and validated, the model will be used for data assimilation with the HGS-PDAF data assimilation system. The HGS-PDAF data assimilation system is currently being developed as part of WP7.

5 Remote sensing based yield prediction model

In this chapter, wheat yield was derived by linear regression based on reported yield values against the time series of six different peak-seasons. The analysis was performed on the yield information from 2013 to 2018, with the application of the Landsat 8-derived Normalized Difference Vegetation Index (NDVI) and Soil Adjusted Vegetation Index (SAVI). NDVI- and SAVI-based forecasting models were validated based on 2018-2019 datasets and compared to determine the most appropriate index of a better performance in forecasting wheat production in the Tisza River basin.

5.1 Site and data description

The study area is part of the Tisza River catchment (altitude below 200 m), which is the most important wheat and corn producing region in the Carpathian basin and in Central and Eastern Europe. Based on the annual reports of the Hungarian Central Statistical Office, around 55% of the arable lands are covered with wheat and maize. 26 wheat fields were selected throughout the Northern Great Plain region (NUT 2) within the Tisza River basin of the Hungarian Great Plain region. The 26 investigated sites were of different sizes ranging from 5 to 34 ha. The total area involved in the research was 438 ha including sites of Nyírbátor. The winter wheat yield in this area was large in 2015 and 2017 (>5 t/ha) and average in 2019 (~ 5 t/ha). However, significant drought periods were observed in several other years, therefore a decrease in yields was recorded in 2013, 2014, 2016 and 2018 (~ 0.8-1 t/ha loss, compared to average).

Compared to high resolution sensors, low resolution satellite images have a much better synoptic view providing higher temporal resolution by means of their large swat width (Rembold et al. 2013). However, the accuracy of yield detection, the interpretation (and validation) of the signal, as well as the reliability of the information content of the satellite images tend to be limited due to the spatial resolution. An average farm size is 14-15 ha in Hungary (Biro et al. 2011) and field sizes are often smaller. Therefore, datasets such as the Fraction of Absorbed Photosynthetically Active Radiation (fAPAR) or Advanced Very High-Resolution Radiometer (AVHRR) are not appropriate for yield monitoring (Gobron and Verstraete 2009), as a single pixel exceeds the average crop farm size in the CEE region. In Hungary, MODIS NDVI time-series at 250 m ground resolution had sufficient temporal and radiometric resolution to discriminate between major crop types and crop-related land use practices (Ferencz et al. 2014, Nagy et al. 2018). On the other hand, the probability of the mixed sub-pixel reflectancy of the 250m MODIS pixels is much higher than in the 10 m counterpart, meaning that the large pixel area is probably only partially represented in the analyzed crop canopy. This type of sub-pixel disturbances may cause an inherent uncertainty during measurement (Dempewolf et al. 2014). Landsat 8 produces data of higher spatial resolution (30 m) and is freely available (Woodcock et al. 2008). Landsat (or similar sensors such as SPOT) is the main source of data of sufficient spatial resolution in most agricultural areas, but has a 16-days' gap between successive images. In very rainy years in Hungary, like in 2020 it can be difficult to obtain a sufficient number of clear images within a growing season, given the cloud cover (Lobell 2013). In addition, studies on the relationship between crop yield and Landsat-derived vegetation indices are mostly bound to focus on individual fields (Liu et al. 2006; Lyle et al. 2013; Potgieter 2014). Since Landsat-derived vegetation indices have been proven to be an effective tool for assessing vegetation conditions, they can be reliably used to predict crop yield. In the present study, Landsat 8 satellite images for the growing seasons in 2013 to 2019 were downloaded from the USGS EarthExplorer website. Landsat 8 data have 11 bands: operational land imager (OLI) and thermal infrared sensors (TIRS) C1 Level-1 images with nine spectral bands. Band 4 (red) and band 5 (NIR) with 30 m spatial resolution were used for further processing.

5.2 Data processing

Data processing and yield forecasting involve several steps from data collection through processing and calibration to validation. First, the data were collected from online sources, then preprocessed for further analysis, including vegetation index calculation (NDVI, SAVI), smoothing and masking for each agricultural parcel. Thereafter, the model was calibrated with crop yields, and finally, the forecasting models were validated with the yield measurements observed. In the current research, NDVI and SAVI were chosen, since these vegetation indices (VIs) were ranked as the VIs with the highest correlations with wheat yield (Panek et al. 2020; Mokhtari et al. 2018). To reduce the noise in the VIs time series, a smoothing process was needed and a penalized spline-based smoother was applied for the smoothing of the data. Normalized Difference Vegetation Index (NDVI) and Soil Adjusted Vegetation Index (SAVI) image data were derived from Landsat 8 satellite images based on the following equations:

$$NDVI = \frac{NIR - RED}{NIR + RED}$$

$$SAVI = \left(\frac{NIR - RED}{NIR + RED + L}\right) * 1.5$$

The value of L varies by the ratio of green vegetation. L=0: in very high vegetation regions, L=1: in areas with no green vegetation. In the current case, L=0.5 was chosen. This value ensures the consistency of the different environmental conditions of the fields and works well in most situations. (Huete, A.R (August 1988).

In this study, 26 wheat parcels were selected to derive average biomass-related VI time series separately. The analysis focused on the peak-season time intervals (May to June), for the 6 years under consideration. The availability of Landsat images limited the reliability of the analysis. Wheat yield prediction models related to each Landsat observation date were developed by the regressing of the observed yield values against time series of Landsat 8-based NDVI and SAVI data. According to studies, remote sensing time series of at least 6 years should be used for analyzing crop yield (Dempewolf et al. 2014, Nagy et al. 2018). Linear regression models were developed based on six years' VIs data (2013 to 2018). The use of standard linear regression models with standard estimation techniques is subject to a number of conditions regarding the explanatory (x) (which were the Vis) and output (y) variables (which was the yield data) and their relationship. For model validation, 2018 and 2019 data were used. The performance of the forecast models was evaluated based on the data of 26 sites (n=26) with the accuracy metrics coefficient of determination (R2), Root Mean Square Error (RMSE) and Normalized Root Mean Square Error (NRMSE).

$$R^2 = 1 - \frac{\sum_{i=1}^{n}(y_i - \acute{y}_\imath)^2}{\sum_{i=1}^{n}(y_i - \bar{y})^2}$$

$$RMSE = \sqrt{\frac{\sum_{i=1}^{n}(y_i - \acute{y}_\imath)^2}{n}}$$

$$NRMSE = \frac{\sqrt{\frac{\sum_{i=1}^{n}(y_i - \acute{y}_\imath)^2}{n}}}{(\bar{y})}$$

Where: y_i is predicted yield data; $\acute{y}_1$ is the observed yield data; $\bar{y}$ is the average of the observed yields; and n is the number of field samples used for validation.

RMSE is a commonly used uncertainty metric for absolute predictions of errors and NRMSE is useful for comparisons between seasons in the case of variable yield ranges (Darvishzadeh et al. 2008). Nash-Sutcliffe efficiency E_1 was also used to assess the accuracy of the predictions. Nash and Sutcliffe (1970) defined the efficiency E_1 as one minus the sum of the absolute squared differences between the predicted yield and the observed yield data normalized by the variance of the observed yield data during the period under investigation:

$$E_1 = 1 - \frac{\sum_{i=1}^{n}(O_i - P_i)^2}{\sum_{i=1}^{n}(O_i - \bar{O})^2}$$

Where: O_i is the observed value or observed yield data, P_i are the predicted yield values; $\bar{O}$ is the mean of the observed values. Values of E_1 range between 1.0 (which is perfect fit) and $-\infty$. An efficiency rate that is lower than zero indicates that the average value of the observed yield would have been a better predictor than the model.

During the validation process, the relative deviations and absolute deviations of the predicted values from the observed values were calculated in order to assess the overall forecasting accuracy. In order to highlight the yield ranges in which the forecasting model performs the best, significant difference between the predicted and observed yield values was assessed within different yield ranges.

5.3 Yield estimation models

Wheat yield estimation was derived by the regressing of the reported (observed) yield values against the NDVI and SAVI time series of six different peak seasons. The effectivity of these vegetation indices for wheat yield assessment and forecasting was analysed and tested. The peak-season of wheat is in May and early June, followed by the ripening stage, then the harvesting period in early July in the Tisza River basin. Therefore, NDVI and SAVI data from day 120 to 190 (30 April to 9 July) were collected and analysed for wheat yield forecast. NDVI and SAVI indices showed the highest peaks (NDVI: 0.46±0.077; SAVI: 0.837±0.338) from day 138 to 150 (18 May to 30 May). After this period, vegetation indices started to decline slightly until the harvest in accordance with several studies (Rembold et al. 2013, Becker-Reshef et al. 2010, Basnyat et al. 2004, Boken and Shaykewich 2002, Delécolle et al. 1992,). The significance and strength of the correlations between VI's and wheat yield changed accordingly with the changes of NDVI and SAVI values (Figure 36). The coefficients of determination were the highest (R^2>0.6) from day 138 to 167 (18 May to 16 June) for both VIs. This interval corresponds to BBCH values from 41 to 71. The difference between the NDVI and SAVI-derived models is that the

NDVI performed maximum regression coefficients (R^2=0.757) in the beginning of the heading stage, whilst SAVI performed maximum regression coefficients (R^2=0.943) in the flowering and early ripening stage. Furthermore, the relationship between the wheat yield and the SAVI values were stronger than in the case of NDVI, suggesting SAVI being a better predictor for wheat yield.

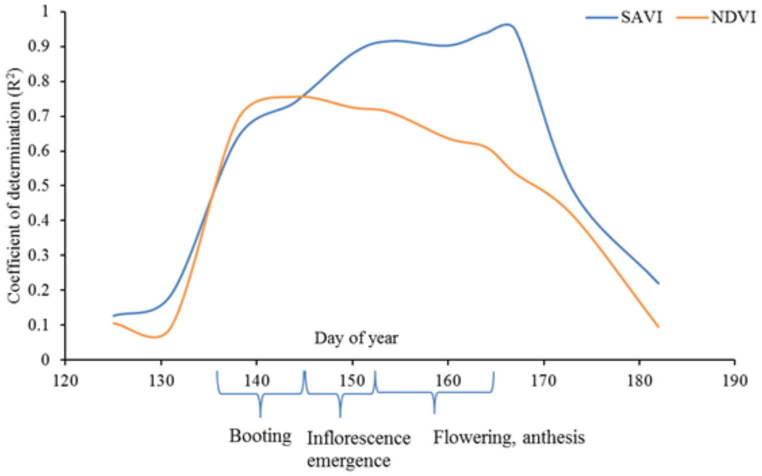

Figure 36: Determination coefficients of forecast versus reported wheat yield at a given time

In order to gain further insight into the yield prediction algorithms, results of the regression analysis were selected to interpret the characteristics of the NDVI- and SAVI-based models in BBCH 41, BBCH 59 and BBCH 71 stages as shown in Figure 37. The on scale values indicated the strongest correction with NDVI and SAVI. The models allow a rapid assessment of yields for different phenological stages of the wheat.

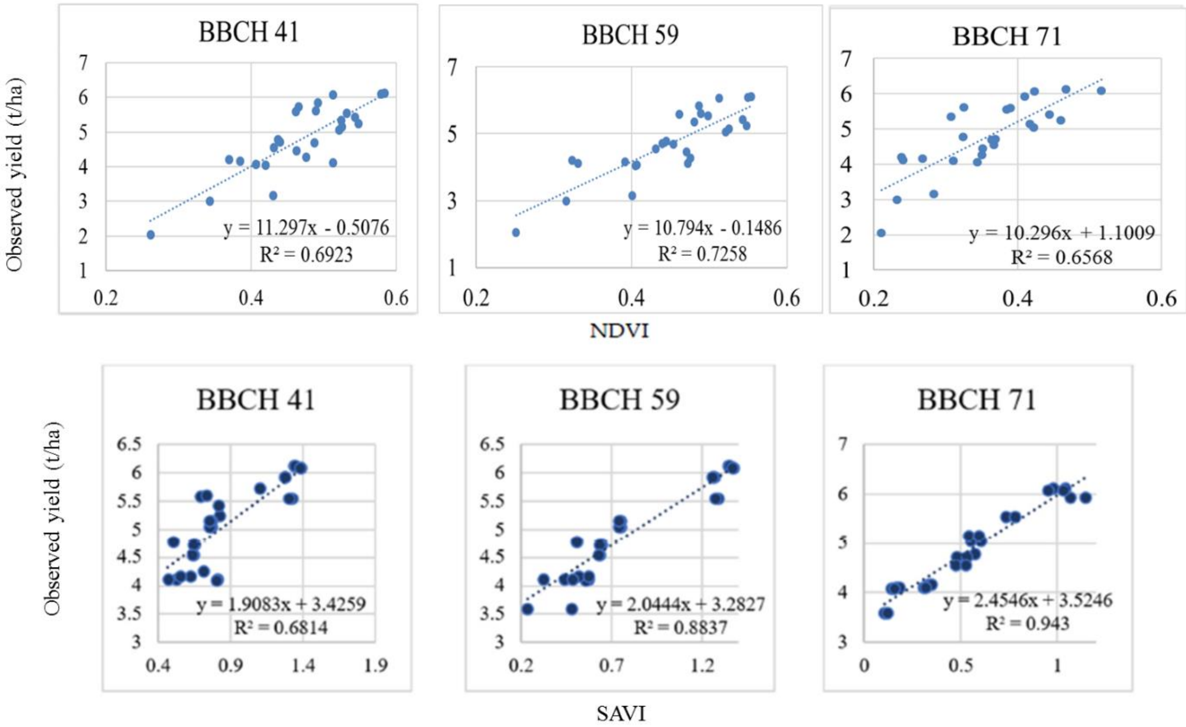

Figure 37: Yield prediction algorithms and NDVI and SAVI models

The performance of NDVI and SAVI for wheat yield forecasting was calculated based on 6 years' training data over the most sensitive (heading, flowering, ripening) period of wheat (May and early June). Average wheat yield data observed in the study area from 2018 to 2019 were used to further validate the forecast models and to calculate prediction accuracy. The Nash-Sutcliffe efficiency index (E_1) was used to test the performance of the wheat yield models. $E_1 = 0.716$ for the NDVI-based model and $E_1 = 0.91$ for the SAVI-based model. The prediction outcomes were compared to the officially reported yield values. RMSE, NRMSE, absolute and relative deviation versus reported yield were also calculated. The coefficients of determination for wheat yield were more than 60% for NDVI and 70% for SAVI during the phenological peak period based on the 6 training years. For NDVI, the forecast error varied between 0.25-0.45 t/ha (5.13-9.30 %) based on the RMSE and NRMSE of the prediction models. The lowest prediction errors were obtained for models calibrated for the early ripening periods. In the case of SAVI, the forecast error varied between 0.17-0.23 t/ha (3.34-4.64 %), i.e. it demonstrated a better performance than the NDVI-based prediction (Figure 38).

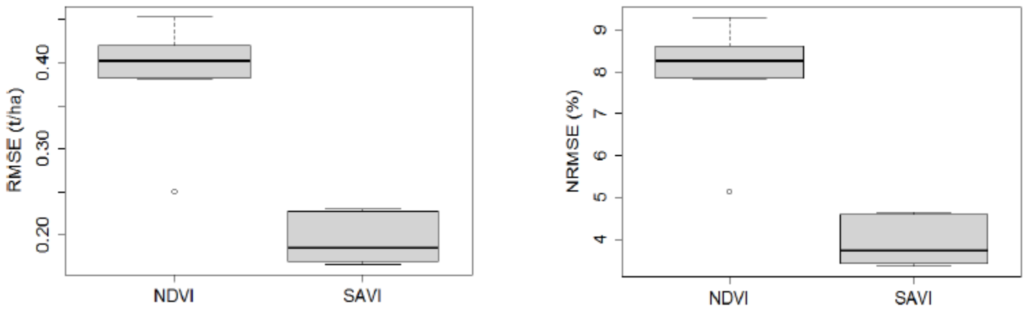

Figure 38: RMSE and NRMSE of predicted values versus reported wheat yield values

In order to assess the overall prediction accuracy of the VI-based prediction models, predicted yield values for the total, most sensitive period was averaged and compared to observed yield values. The RMSE of NDVI-based prediction model was 0.357 t/ha (NRMSE: 7.33%). The RMSE of SAVI-based prediction model was 0.191 t/ha (NRMSE 3.86%) (Figure 39).

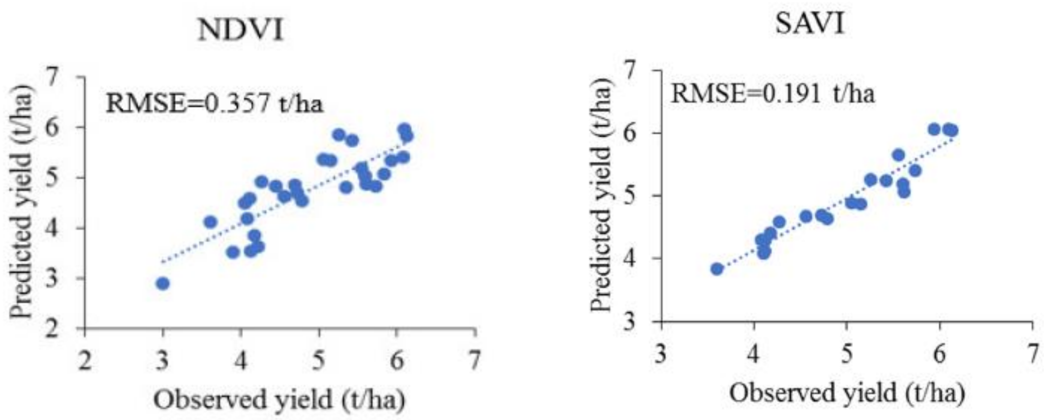

Figure 39: The accuracy of the predictions based on NDVI and SAVI

Based on the mean relative deviation (-1.072 %), NDVI slightly underestimated the observed yield values. On the other hand, SAVI-based predictions resulted in a slightly positive bias (0.46%) compared to reported values. The mean absolute deviation between the estimated and the reported yield data was also higher in the case of NDVI-derived prediction (about 8.5 %) compared to 4.1 % for SAVI-based yield predictions (Figure 40). The accuracy of NDVI-derived prediction was only below the 5% threshold, which is generally regarded as good (Ferencz et al. 2004).

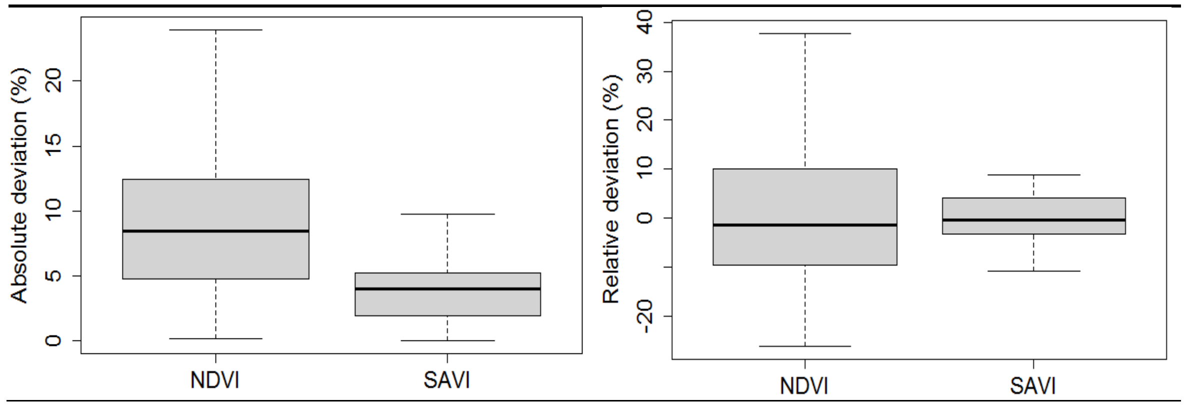

Figure 40: Absolute and relative deviation values from officially reported wheat yields

The uncertainties and forecasting precision for different yield ranges were evaluated in order to highlight the yield ranges in which the forecasting model shows the best performance. First, predicted yield values were associated with observed yields. Then 4 groups with different yield intervals were set up based on observed yield values. Independent T-test analyses were used to assess significant differences between observed and predicted wheat yields. As a result, the distribution of the predicted yields was compared to the real, observed yield distributions (Figure 41).

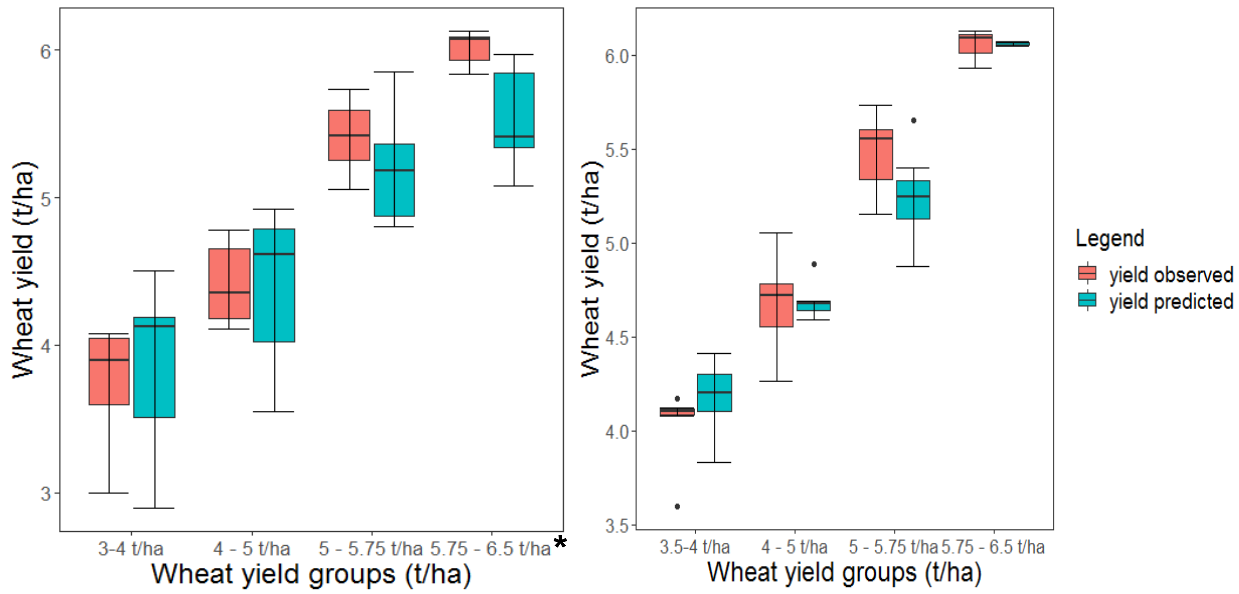

*yield range, in which there was significant difference between observed and predicted yield data ($p<0.05$)

Figure 41: Differences between observed and predicted yield within wheat yield ranges for NDVI and SAVI

In the case of NDVI, higher yield values were significantly underestimated. The difference between predicted yield values and observed yield values is 0.55 t/ha (on average). In the case of SAVI, there were no significant differences between observed and predicted values.

This study was carried out for the purpose of developing a satellite-based system (Landsat 8) for wheat yield forecasting and to determine the uncertainties of the prediction for different yield amounts to provide a solution applicable to the lowlands of the Tisza River catchment. Several studies (Rembold et al. 2013, Marti et al. 2007, Labus et al. 2002, Mkhabela et al. 2011, Bai et al. 2019, Yousfi et al. 2016) have shown the validity of using satellite-derived vegetation indices for wheat yield forecasting. In accordance with these previous studies, current results have demonstrated that there are significant correlations between the VIs and final crop yields, and the peak season with the highest NDVI values at the heading stage of wheat was found to be the most optimal to predict the crop yield.

The NDVI- and SAVI-derived models performed well regarding wheat yield prediction. Wheat yield prediction for the most sensitive period (May and early June) is a better predictor than the application of prediction models individually derived from VIs on a certain day of the year. The error rate of the NDVI-based prediction model was 0.357 t/ha (7.33%), which is in correspondence with Rudorff and Batista (1991), who estimated wheat yield at the farm level using Landsat in Brazil with 0.37-0.44 t/ha prediction accuracy. In Pakistan, values were reported based on MODIS NDVI with 10% accuracy (Dempewolf et al. 2014) and Nagy et al. (2018) studied wheat yield forecasting for the Tisza River catchment using MODIS NDVI and found 7% accuracy between the predicted and actual yield.

For high yields, NDVI based yield forecasts demonstrate the highest rates of uncertainty. This might be because NDVI is known to saturate at high LAI values (Sellers 1985, Goswami et al. 2015), which in turn reduces NDVI sensitivity for higher yields. From average to lowest wheat yields, it is the NDVI-based forecasting model that performs the best, therefore prediction can be a useful tool to detect yield losses caused by drought phenomena, and it can also present a feasible option in specific crop drought monitoring.

Contrary to NDVI, SAVI-based predictions demonstrate a similar performance for all yield ranges and performed better compared to NDVI with an error rate of 0.191 t/ha (3.86%). Muller et al. (2020) also found that SAVI achieved slightly higher accuracies than NDVI, suggesting that SAVI reduced some of the effects of soil background reflectance. Liaqat et al. (2017) also proved that SAVI-derived models performed better for wheat prediction than NDVI or EVI. Results also showed that soil adjusted vegetation index (SAVI) was the best VI (out of several others, including NDVI) for LAI estimation (Mokhtari et al. 2018), which can contribute to the better prediction accuracy of SAVI.

On the whole, moderate and high spatial resolution remote sensing images such as Landsat 8 images have a significant potential in wheat yield prediction and SAVI is a better predictor for wheat yield than NDVI.

The model developed is based on spectral indices derived from 30 m spatial resolution Landsat 8 multispectral images. In our days, with Sentinel’s 2 and Proba-V sensors, a new era of Earth observation has started (Rembold et al. 2013). With these new sensors, data availability at coarse and medium resolution increases at high revisit frequency, but further studies are needed to guarantee proper sensor inter-calibration, as there aren’t any time series available for them for the time being which could be used for accurate yield forecasting. In addition, some studies have suggested that multivariate analysis or non-linear methods are more reasonable than linear approaches when canopy reflectance is used to establish the yield prediction model and that they have equal or better performance than the spectral index method in crop yield prediction, especially when hyperspectral data are used (Uno et al. 2005, Ferrio et al. 2005, Ye et al. 2007).

Information on long-term yield variability is important for tailoring farming practices to the needs of crops. In particular, remotely sensed vegetation indices (VIs) such as NDVI and SAVI have been widely utilized for agricultural mapping and monitoring. Wheat yield forecasting techniques based on remote sensing data with 30 m spatial resolution have been evaluated. In this study, the forecasting method was developed based on vegetation indices derived from multi-spectral remote sensing data (Landsat 8 NDVI and SAVI) and reported wheat yield data in the Tisza River catchment area. The wheat yield forecasting model developed based on six training years provides timely information on wheat production in a regular and standardized manner at the field and catchment level and makes it possible to predict the yield six weeks before harvest. Understanding the applicability and accuracy of yield prediction is also an essential component of forecasting, because the ultimate goal is to reduce forecast uncertainties for a particular location and for a specific group of people or a specific segment of the agricultural or economic sector. With the forecasting method, moderately good and good estimates can be provided based on NDVI and SAVI as early as possible during the growing season, which can then be updated periodically throughout the season until harvest. This information can reduce the impacts of possible yield losses, if communicated to farmers or decision-makers in a timely and appropriate manner. This way, considering the recent development of global environmental changes, governments and international boards would become capable of mitigating water shortage, and thus providing for food security and addressing societal and international conflicts more effectively. On another decision-making level, this type of information would enable farmers to optimize irrigation and fertilization expenditures and thereby contribute to the achievement of maximum profits.

6 Remote sensing based vegetation data in irrigation

Crop irrigation demand is essential for agricultural producers to understand (WOZNICKI et al., 2015). The active control of irrigation and water resources can prevent land degradation, increase plant yields and reduce capital investment (DE VRIES et al., 2003). Irrigation water management involves the application of a certain amount of water according to crop demand, which can be retained in and is consistent with the intake characteristics of the soil (USDA, 2016). The demand of plants is extremely important in the process of water supply management. In other words, accurate prediction of plant consumption and evapotranspiration is the key to determining the irrigation amount (DJAMAN et al., 2018). Weather parameters, crop factors, farming methods and environmental conditions all affect crop evapotranspiration (FAO, 2010).

6.1 Satellite images of vegetation and soil with potential use for irrigation support

6.1.1 Study area

Temmesjoki basin is located south-east of Oulu (Northern Ostrobothnia region in Finland, Figure 42). As reflected by Earth Observation Satellite (EOS) data, the basin encompasses 9 land cover classes as listed in the table below (Table 5).

From all the 10 classes mentioned in the global land use/land cover (LULC) map for the year 2020 by ESRI[1], the land cover of the class 'Trees' (i.e. Forests) appears to be the major class (880.330 km^2 or 66.72% of the area). Other land cover classes are 'Crops' and 'Shrubs' covering an area of nearly 241.94 km^2 (16.68 %) and 215.26 km^2 (14.84 %), respectively. Although a variety of crops are cultivated in the basin, potato is the main crop.

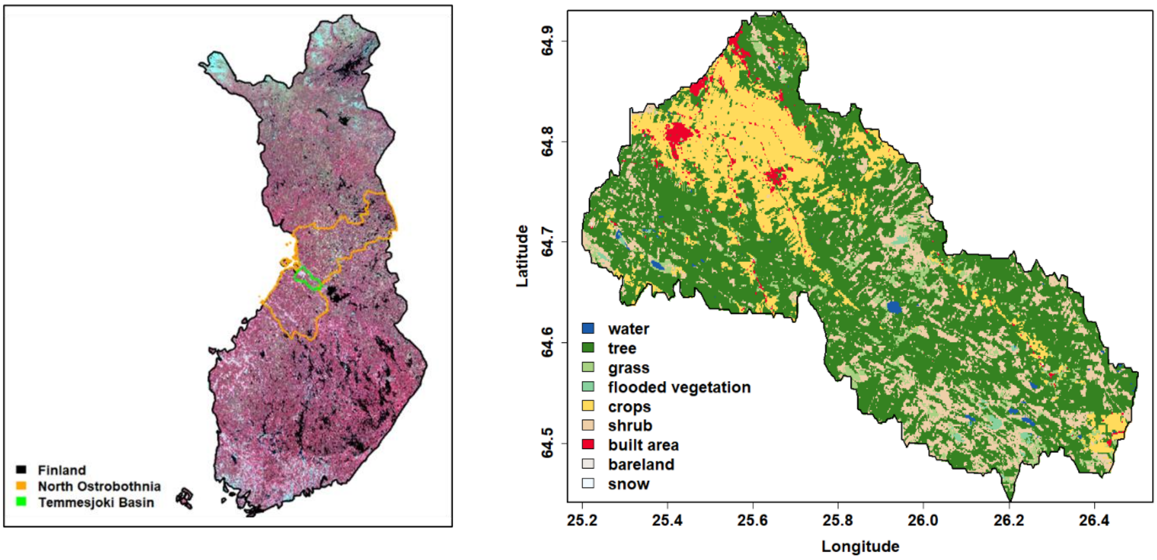

[1] https://www.arcgis.com/home/item.html?id=d6642f8a4f6d4685a24ae2dc0c73d4ac , accessed 28.10.21

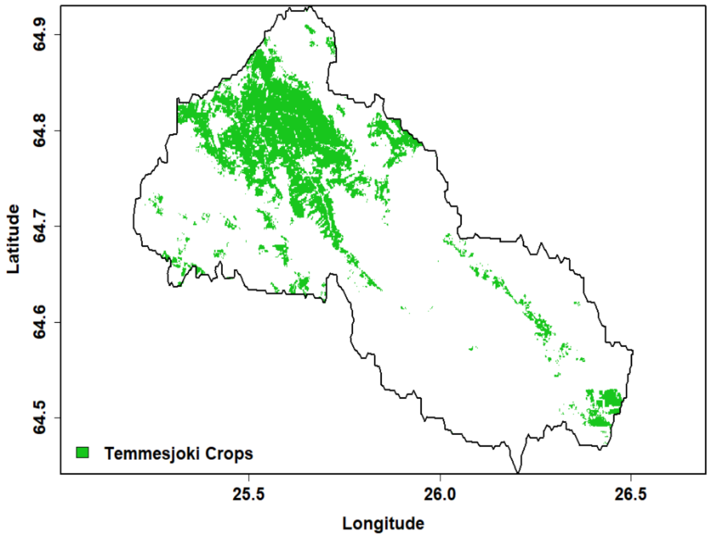

Figure 42: Temmesjoki basin and its location and land cover

Table 6: Land cover classes in Temmesjoki basin

Class Code	Class Name	Area (km^2)	Percent
1	Water	7.48	0.51
2	Trees	880.33	60.72
3	Grass	70.48	4.86
4	Flooded Vegetation	7.38	0.50
5	Crops	241.94	16.68
6	Shrub	215.26	14.84
7	Built Area	26.17	1.80
8	Bare land	0.29	0.02
9	Snow	0.44	0.03

6.1.2 Methods

Analysis of remote sensing datasets

Remote sensing analysis focused on the assessment of cropland areas and was aimed at the evaluation of the potential use of satellite images for irrigation and crop management. We assessed the correlation between annual crop production and potential climatological variables which may affect it. From the earth observation variables available to us, land cover, precipitation, Land Surface Temperature (LST) and evapotranspiration (ET) were considered in this study. We used the Google Earth Engine (GEE) platform to process the remote sensing images. The Earth Observation Satellite (EOS) data used in this study are summarized along with spatial and temporal resolutions in Table 7. Crop yield values were collected from the agricultural statistics database of the Natural Resources Institute Finland (LUKE).

Temporal resolution constitutes the major prerequisite for the current investigation. For the purpose of the effective monitoring of crop water requirement, the temporal resolution of the temperature and the precipitation have to be available for every day.

Table 7: Earth Observation Satellite (EOS) data used in the study

Variable	Satellite / Sensor	Spatial Resolution	Temporal Resolution	References
Land cover	Sentinel 1-2	10-m	Year 2020	(Karra et al.,2021)
Precipitation	GPM	10-km	3-Hours	(Skofronick-Jackson et al., 2018)
	TERRA Climate Model	4-km	Monthly	(Abatzoglou et al., 2018)
LST	MODIS	1-km	Daily	(Wan, 2006)
ET		500-m	8-Days	(Running, 2018)

Remote sensing-based water stress assessment

Satellite observations have also been used to assess crop water stress. For that purpose, the crop water stress index (CWSI) is used. According to Jackson et al., (1981), the CWSI can be expressed in terms of evapotranspiration as follows:

$$\mathrm{CWSI} = 1 - \frac{\mathrm{ET_a}}{\mathrm{ET_0}}$$

where ET_a= Actual evapotranspiration and ET_0= Reference evapotranspiration.
The definition of drought proposed here is based on standardized precipitation. The Standardized Precipitation Index (SPI) was calculated at the timescales of 3, 6, 12, 24 or 48 months. The SPI-based drought categories according to McKee et al. (1993) are presented in Table 8.

Table 8: SPI-based drought categories

SPI Values	Drought Category
0 to -0.99	Mild Drought
-1 to -1.49	Moderate Drought
-1.50 to -1.99	Severe Drought
≤ -2.0	Extreme Drought

6.1.3 Results

As shown by the results, Temmesjoki basin in general receives sufficient precipitation for rainfed farming, however, too low or high precipitation may cause reduced crop yield in some years. Yield was low in 2004, 2006 and 2008, and these years were analyzed more carefully. As for precipitation, EOS data show high, low and normal mean annual monthly values for 2004, 2006 and 2008, respectively (estimated from TERRA-Climate) (Figure 43).

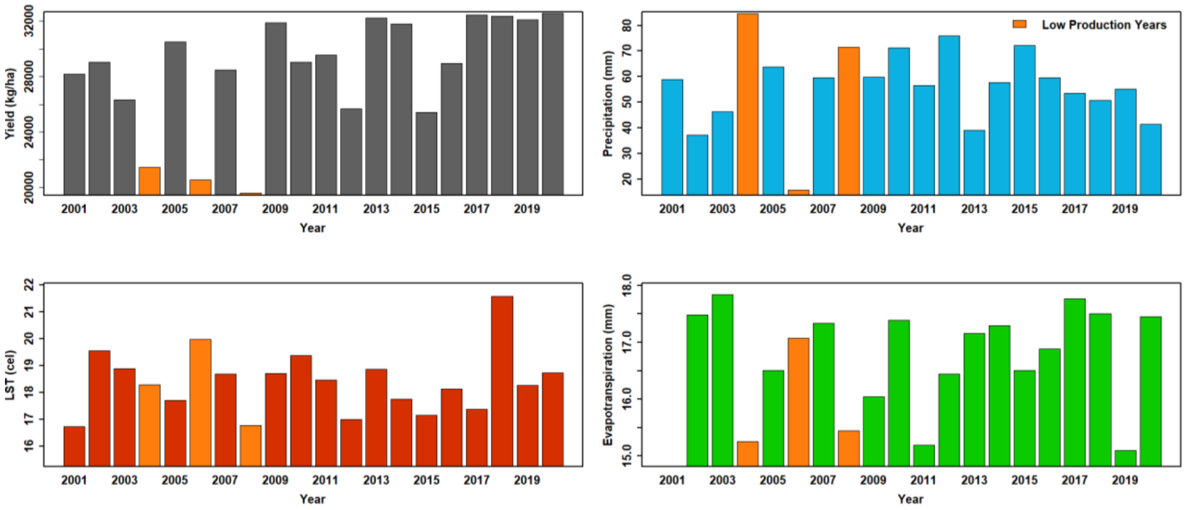

Figure 43: Crop production yield vs. Climatological Variables

The highest precipitation occurred in 2004 with mean monthly precipitation exceeding 80 mm (Figure 43). The frequency table (calculated by GPM daily data, Table 8) shows 56 days with precipitation above 1 mm during the growing season (May-Sep). The low yield in 2004 was probably due to too much precipitation.

The lowest mean monthly precipitation (less than 20 mm per month) was recorded in 2006. In that year, only 32 days had more than 1 mm rainfall, 37.5% of which occurred in months relevant for crop production (Table 8). This has been the lowest recorded rainfall over the last 20 years. The low yield observed in 2006 was due drought, as also indicated by the crop water stress index (Figure 44).

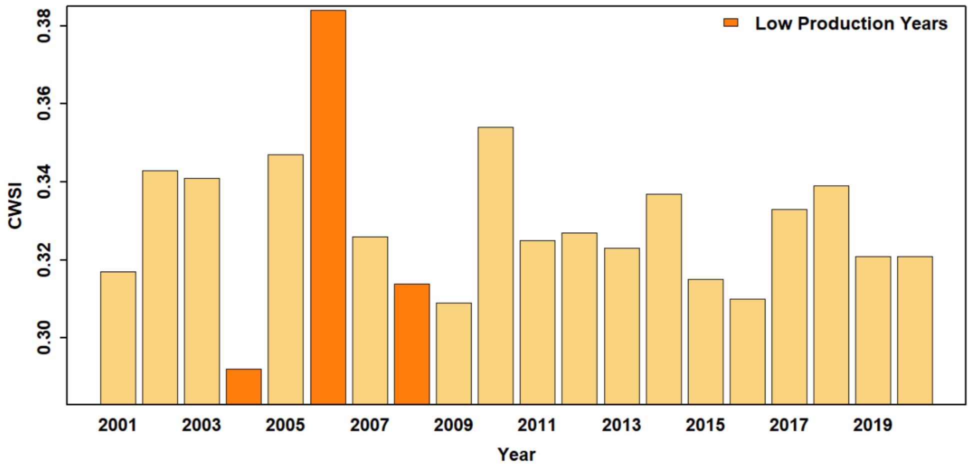

Figure 44: Crop Water Stress Index

The RS data (cf. Section 6.1) and water balance simulation (WBS) (cf. Section 3) analysis also show that a serious drought occurred and caused low crop production in 2006. The SPI-based drought categories also indicated extreme drought in 2006 (Appendix 1, Figure A1). Monthly precipitation maps of June - August for the last two decades also indicate lower precipitation in 2006 compared to other years (Appendix 1, Figure A2- A4).

In 2008, mean monthly precipitation was almost 70 mm (Figure 43). However, it was not evenly distributed over the cropping period (Table 9), which could be a reason for low crop production (Figure 43).

Table 9: Precipitation frequency over the last 20 years

Year	Precipitation < 1 mm			Precipitation > 1 mm		
	Days (May - Sep)	Percent (Jun-Aug)	Mean (Jun-Aug)	Days (May - Sep)	Percent (Jun-Aug)	Mean (Jun-Aug)
2001	99	57.6	0.17	54	64.9	5.49
2002	113	61.1	0.22	40	47.5	7.9
2003	108	62.9	0.28	45	53.3	5.13
2004	97	58.7	0.27	56	62.5	7.67
2005	108	61.1	0.29	45	57.8	6.81
2006	121	66.2	0.15	32	37.5	3.1
2007	100	61	0.25	53	58.5	7.1
2008	108	50.9	0.20	45	82.2	7.64
2009	111	63.9	0.18	42	49.9	7.9
2010	100	56	0.16	53	67.9	5.9
2011	102	58.8	0.18	51	62.7	7.7
2012	93	55.9	0.27	60	66.6	6.12
2013	111	53.1	0.24	42	78.8	6.25
2014	108	53.7	0.13	45	75.6	5.5
2015	95	58.9	0.19	58	62	6.75
2016	102	52.9	0.16	51	74.6	8.5
2017	118	55.8	0.07	35	74.2	6.5
2018	117	58.1	0.08	36	77.8	6.7
2019	112	62.6	0.07	41	53.7	7.14
2020	104	61.5	0.15	49	57.2	7.5

6.2 Model concept for vegetation based ET_c estimation

FAO Irrigation and drainage paper 56 proposed an updated workflow for the calculation of reference and crop evapotranspiration based on meteorological data and crop coefficient (Han, 2018). The regenerated method provides estimates which are more consistent with the actual crop water demand information worldwide and overcomes the shortcomings of the previous FAO Penman method (SMITH et al., 1998). In addition, it describes and explains crop evapotranspiration (ET_C), crop coefficient (K_c), meteorological data and reference evapotranspiration (ET_0), and also clarifies the relationship between them.

ET_0 is defined by temperature, relative air humidity, solar radiation, wind speed and air pressure according to the FAO Penman-Monteith equation (FAO, 2010). The equation determines the evapotranspiration of the reference surface of hypothetical grass and provides a standard that can be compared to the evapotranspiration in different periods or other regions in a year and is related to the evapotranspiration of other crops (Zotarelli - Dukes, 2010).

Crop evapotranspiration is estimated in the FAO methodology by the multiplication of the reference grass evapotranspiration with the factor K_c, which is dependant on crop characteristics such as crop height, the albedo of the crop-soil surface, canopy resistance and evaporation from soil (Pereire, 2007). Thus, K_c has a seasonal pattern during the vegetation period, distinguishing between an initial, growing, mid-season and end stage (Lazzara - Rana, 2010).

Denser canopy tends to reduce evaporation, as well as transpiration from the layer closer to the ground surface by creating a more humid and cooler microclimate. Consequently, only a limited volume of water can leave the system, since the direct contact between the surface of the more saturated canopy top and the dry, hot external system is limited (Jing et al 2021).

The FAO provides time-averaged K_c stage-specific values for several crops, including maize. For maize, the typical K_c values in the four stages are 0.3 in the initial stage, followed by a continuous increase from 0.3 to 1.2 in the growing stage, a plateau in the mid-season and a continuous decrease from 1.2 to the values between 0.6 and 0.35 in the end stage (Han, 2018). Jiang et al. reveal that K_c and the Leaf Area Index (LAI) show a strong relationship during the different growing stages of maize (Jiang et al., 2014). In a crop water supply model, both LAI and K_c are related to vegetation state (Čerekovic et al., 2010; Diet al., 2019; Munitz et al., 2019), it is significant to determine them for practical reasons. K_c can be obtained by the FAO-formulations or estimated from the Leaf Area Index (LAI).

$$ET_c = K_c \cdot ET_0$$

Leaf Area Index is defined as the unilateral green leaf area per unit surface area characterizing plant canopies (Watson, 1947). Monitoring the distribution and change of LAI is important for assessing the growth and vitality of the vegetation (Fang et al., 2019). LAI can be measured by (1) a direct method ("destructive sampling") or (2) an indirect approach, by using optical equipment (Fang et al., 2019). Both methods of in-situ measurements usually involve intensive labour costs, and optical methods are also affected by the weather and environment due to instrument characteristics. LAI can also be estimated by remote sensing, through the empirical relationships with canopy reflectance or some vegetation index (Broge - Leblanc, 2001).

6.2.1 Overview of the analysis

Remote sensing technologies are systems broadly used in the analysis of Earth surface processes, including the assessment of moisture conditions and vegetation health. The present chapter aims to provide irrigation support based on cost-effective, satellite-derived remote sensing information collected for the years 2018, 2019 and 2020 in Emilia-Romagna, Italy and the past two years in Nyírbátor, Hungary. The applicability of optical remote sensing technologies is highly determined by the visibility of the land surface. 2020 was a cloudy and rainy year in Hungary, resulting in long data gaps in the most important growth stages of the vegetation, which in turn forced the authors of the current Chapter to develop a novel approach to provide a straightforward solution for the evaluation of the water balance.

Two methodologies were developed for the deterministic spatiotemporal modelling of the water budget. Both approaches are based on the joint realization of observed phenological phases (BBCH) and hydrometeorological data series, and the fusion of the either spatially or temporally high resolution of remotely sensed vegetation indices. The methodologies can be summarised as follows:

<u>(1) The simplified model of the crop coefficients</u> can be useful, when the agricultural field is small compared to the sensor footprint of the high temporal resolution data series. This approach is based solely on high spatial resolution vegetation indices calculated from SENTINEL-2 images alongside with local observations. The spatiotemporal pattern of water budget calculation is simplified into the combination of a one-dimensional series for a certain vegetation index and the sequences of the Penman-Monteith input environmental factors. This technique is only effective with no significant data gaps in the satellite acquisitions (Figure 45).

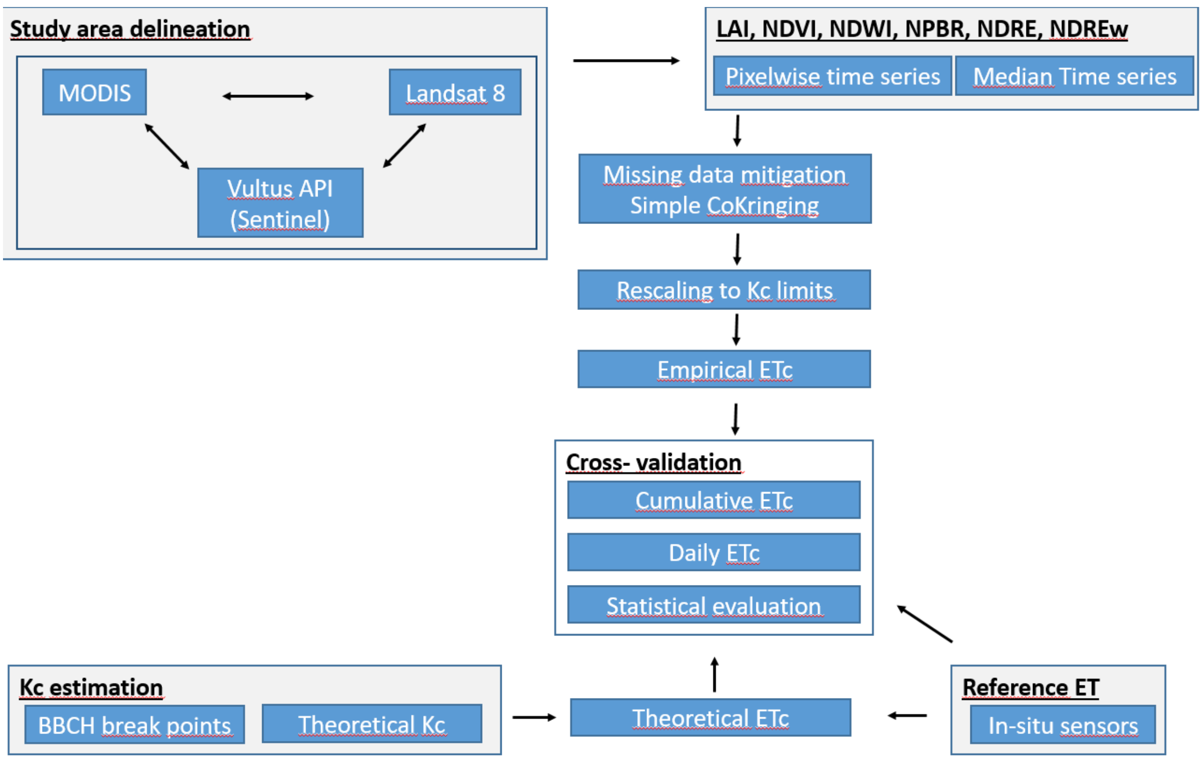

Figure 45: Simplified overview of the crop evapotranspiration model

(2) The fusion of high spatial and high temporal resolution satellite-derived information, which is the second approach, attempts to estimate long gaps in satellite information. The June of 2020 happened to be an unusually rainy period in Hungary. The continuous cloud cover made the proper modelling of the most significant vegetation development stage impossible. Our novel approach is based on the complete fusion of the MODIS and SENTINEL images. The time-series model parameters of derived vegetation indices (even the raw spectral reflectances) are varied in space, therefore the capturing of space-time interactions provides substantial information about the development of the environmental process under study. The implementation of the model enabled the assessment of the water budget, thereby supporting precision irrigation for every 10 m^2 of the study area. The variability regarding the water budget at the locations sampled was modelled simultaneously in space and time through deterministic functions.

The next subchapters discuss the interpretation and limitations of remotely sensed spectral indices, as well as their relationship with the water consumption of the vegetation. Section 6.2.3 introduces the study sites where the distinguished methodology is benchmarked. In Section 6.2.4, the modelling framework of the simplified approach is introduced via an example study site located in Italy. In Section 6.2.5, the implications of the fusion model and the spatiotemporal phenomena in general are briefly discussed via an example from the Hungarian study site in 2020.

6.2.1.1 Considerations related to remotely sensed data fusion

High temporal resolution information from MODIS Terra and high spatial resolution information from SENTINEL 2 MultiSpectral Instrument (MSI) sensors (Table 10) were combined in order to support the optimal use of the limited water resources for crop yield maximization[2]. Due to the differences in sensor characteristics and product generation algorithms, cross-sensor relationships were extensively analysed to estimate reflectance values (Miura et al., 2006).

In order to be able to assess and compare the remote sensing bands for different resolutions, resampling processes had been widely investigated by UNIDEB in a closely related research of the phenomena under the current study. The results were summarized by Zhao (2021). As pointed out by Zhao, the task is analogous with the concerning the exploration of subsurface oil reservoirs, for which lattice data (seismic surveys) are widely available, in combination with location-specific lithological series (logging data) (Deutsch and Journel, 1998). In our case, the spatially sparsely, but temporally more often sampled MODIS images represent the lattice data, whereas higher resolution satellite images can be considered as spatially extensive auxiliary information.

In remote sensing, lattice data represent the sum of the energy reflected from the surface on the specific region of the sensor (charge-coupled device - CCD) for a specific time interval (camera shutter). Remotely sensed electromagnetic energy is divided into energy sub-intervals, called spectra***.*** In short, larger CCD surface or lower flight path results in better spatial resolution, higher flight path leads to faster revisit over the same area, and longer shutter time generates better spectral resolution (Table 10). Consequently, if the same spectral content needs to be maintained, higher spatial resolution comes at the expense of less frequent revisits, while higher temporal resolution is achievable for the spatial resolution in exchange (BROOK et al 2020).

[2] The rare revisit and weaker spatial resolution, as well as cross-sensor calibration instability led to the exclusion of the Landsat 8 images from the analysis.

Table 10: Spatial (m), temporal (day) and spectral (µm) resolution of the most popular multispectral sensors

	SENTINEL 2 MSI		LANDSAT 8 - OLI		MODIS - Aqua	
	wavelength (micrometer)	spatial resolution (m)	wavelength (micrometer)	spatial resolution (m)	wavelength (micrometer)	spatial resolution (m)
C/A	0.421-0.457	60	0.435-0.451	30	0.438-0.448	1000
Blue	0.439-0.535	10	0.452-0.512	30	0.459-0.479	500
Green	0.537-0.582	10	0.533-0.590	30	0.545-0.565	500
Red	0.646-0.685	10	0.636-0.673	30	0.620-0.670	250
VRE	0.694-0.714	20				
VRE	0.731-0.749	20				
VRE	0.768-0.796	20				
NIR	0.767-0.908	10				
narrow NIR	0.848-0.881	20	0.851-0.879	30	0.840-0.876	250
Cirrus	1.338-1.414	60	1.363-1.384	30	1.230-1.250	500
SWIR	1.539-1.681	20	1.567-1.651	30	1.628-1.652	500
SWIR	2.072-2.312	20	2.107-2.294	30	2.105-2.155	500
Revisit period (day)	5		16		1	

The combination of energy levels measured in the spectral intervals over the same geographic location enables us to characterize the earth surface at a high frequency and relatively limited costs. This characterization may take the form of multivariate classification (e.g. cluster analysis), segmentation (e.g. principal component analysis) or an index calculated from the wide variety of spectral band combinations.

6.2.1.2 The significance of the spectral indices

Both MODIS Terra and SENTINEL MSI are optical and passive remote sensing sensors, thus their operation is highly vulnerable to the incoming electromagnetic wave reaching the reflective surface. The energy sum is determined by both the inter-annual sun angle fluctuation and atmospheric conditions (weather, pollution, dust). Spectral indices have great significance, not only because they are easy to apply, but also by mitigating the varying insolation conditions effectively – to some extent at least. This normalizing nature of the spectral indices enables the comparison of the surface conditions for different time instants (Brook et al 2020).

Based on the satellite data provided by VULTUS for the Italian and Hungarian site, the performance of the following vegetation indices was examined in the crop evapotranspiration analysis:

- NDVI: Normalized Difference Vegetation Index (Sun et al 2021)
- NDWI: Normalized Difference Water Index (Saddik et al 2021)
- NDRE: Normalized Difference Red Edge (Reuben et al 2021)
- NDREw: Normalized Difference Red Edge for wheat provided by VULTUS
- NRPB: Normalized Ration Procedure between bands VV and VH polarization
- LAI: Leaf Area Index (Qu et al 2021)

The ultimate aim of the MODIS – SENTINEL fusion discussed is to estimate a temporally continuous, spatially dense dataset in the SENTINEL data dimension. To this end, the temporal pattern of the filtered and estimated MODIS data series can be mathematically transformed to valid SENTINEL observations through regression equations (Rufin et al 2021). The approach is limited, in that MODIS and SENTINEL pixel values have to represent the same, stationary environmental process. For example, if both active agricultural production and permanent land use are present under a specific pixel, the heterogeneity of the natural fluctuation of electromagnetic reflectance will make it impossible for us to reconstruct the development process of the vegetation in the agricultural area under study in a representative manner.

Therefore, the approach introduced requires pixel-wise stationarity over the site subject to the analysis. Consequently, the minimal parcel size that can be estimated with the proposed approach is in the best case identical with the pixel size of the spatially sparse MODIS band. Only the red and near infrared bands of MODIS can provide 250 m resolution, all other bands are 500 m. This limits the analysis to the widespread Normalized Difference Vegetation Index (NDVI) for the Hungarian site.

Although parcel sizes in Emilia-Romagna are much smaller, i.e. 4 hectares on average, the effect of cloud cover on the availability of SENTINEL images was fortunately not as substantial as at the Nyírbátor site in year 2020. However, it should be noted that the lack of the stationarity of the 250m resolution MODIS images (sub-pixel spectral mixture related to roads or different irrigation facilities) would not allow the application of the more complex data fusion approach implemented in Hungary

6.2.2 Study site description

Field trials are carried out by CER at the experimental farm Acqua Campus, covering 12.5 hectares and divided into approximately 25 fields. The fields are located in the plain of the Po valley, in the province of Bologna, near the village of Mezzolara di Budrio (44°34´N, 11°32´E). There are various crops cultivated in the farm (both perennial and annual). Crop rotation in the experimental fields is characterized by annual crops, such as winter wheat, soya, maize, onion and processing tomato.

The soil of the farm is typical of the Po valley low land and has a high content of both silt, clay and fine sands. It is deep and without a noticeable skeleton (>2 mm). The soil in the area can be described as clay loam. It belongs to the Italian soil group "Suoli SECCHIA franco argillosi", which can be classified as "Oxyaquic Haplustepts" (fine loamy, mixed, superactive and mesic according to Soil Taxonomy). These soils are calcareous and moderately alkaline; they have a texture of clay loam in the superficial layers and loam deeper in the profile. Soil layers are by multiple floods of the nearby Idice river. The soil within the farm is heterogeneous and its hydraulic characteristics vary from field to field and layer to layer, with a slight gradient from east to west. The average values for the soil parameters are specified in **Hiba! Érvénytelen könyvjelző-hivatkozás.**1. Soil bulk density ranges from 1.3 to 1.5 g/cm^3; saturation is between 0.47 and 0.50 m^{3}m^{-3}; field capacity is between 0.27 and 0.34 m^{3}m^{-3}; the permanent wilting point is between 0.08 and 0.11 m^{3}m^{-3}; and the available water content is between 0.207 and 0.238 m^{3}m^{-3}. An extended, shallow groundwater table is normally present at a depth ranging from -0.6 to -1.8 m. During winter and at the beginning of the growing season, capillary rise could be significant in terms of the replenishment of the evapotranspiration of crops.

The experimental farm is supplied with the CER canal water/supplied with water from the CER canal, the quality of which is checked several times during the irrigation season. CER's irrigation water characteristics (long-term average) are freely available at https://qa.consorziocer.it:3000/cer_graph/client/index.html.

Table 11: Soil analyses

Parameter	Unit	Average
Sand	%	32
Silt	%	50
Clay	%	18
pH	log H^-	8,27
$CaCO_3$ total	%	13,5
$CaCO_3$ active	%	3,1
N total	%	0,06
K exchangeable	meq/100 g	0,34
P (Olsen)	meq/100 g	5,49
CEC	meq/100 g	21,6

The farm itself is fully equipped to monitor various environmental variables used for modelling and there is also a small laboratory set up for principal soil and biomass analyses. The major variables monitored include soil moisture levels, groundwater levels, the amount of drainage and the concentration of pollutants and nutrients in drainage water. The farm also has a fully operational weather station equipped with a rain gauge, anemometer, phreatimeter and pan evaporimeter (Figure 46).

Figure 46: Weather station located at Acqua Campus

The climate of the site can be defined as sub-humid, with a mean annual temperature of 13.7°C and an average annual rainfall of 771 mm. The year of the field trials was characterized by severe drought. According to the estimates based on CER analyses, it has been the second harshest year in the study area with cumulative precipitation mostly below 200 mm in all areas which represents a deviation by 50% from the reference climate (period 1961-2018). These conditions contributed significantly to corn production and yield values.

For the purposes of this study, two experimental fields have been cultivated with corn in the ACQUACAMPUS farm (Figure 47):

Field 10 – Irrigated (Irr): this field was irrigated with the pressurized method (roller irrigator), where timing and volume was defined with the support of IRRIFRAME.

Field 11 – Not irrigated (NoIrr): this field represents the test and was not irrigated.

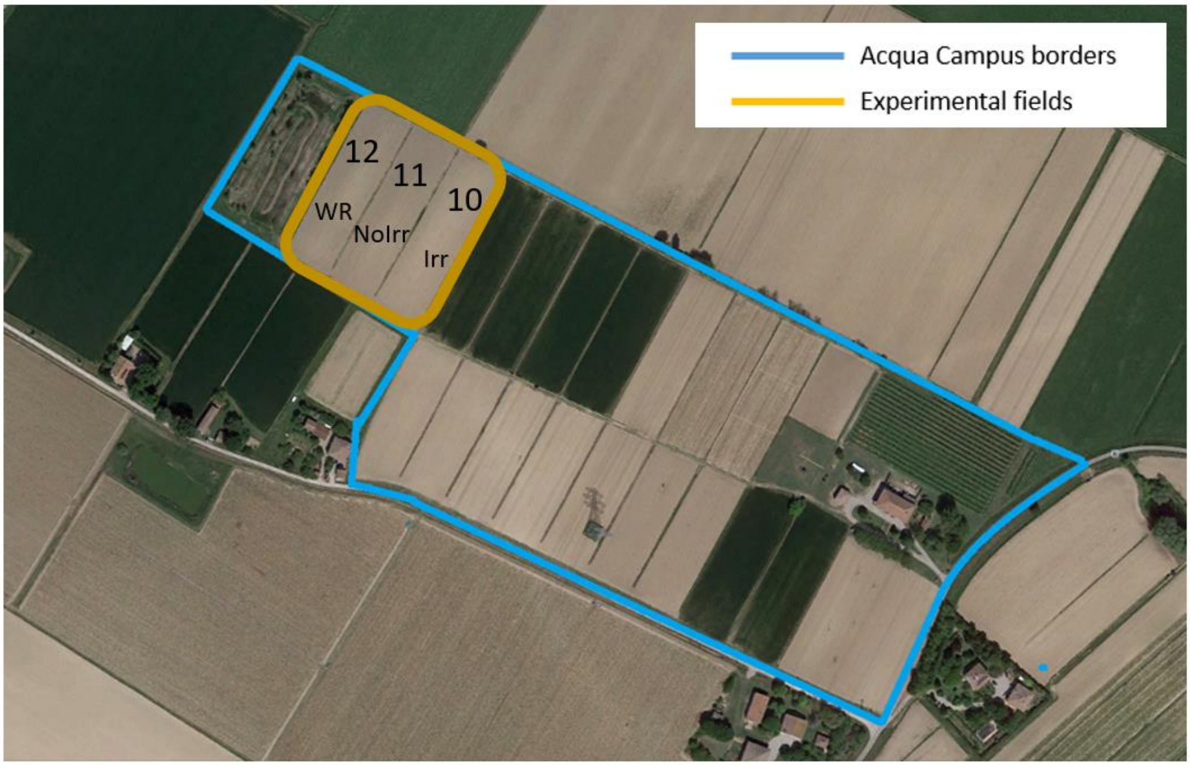

Figure 47: Experimental fields dedicated to the tests

Hungarian study site

The study site is the same as described in Chapter 5.

6.2.3 Compilation of the database of observations

The analysis is based on several independent, freely available datasets. The overview of the data sources is summarized in Table 12.

Table 12: The overview of the data sources

Data provider	Provided datasets	Primary data source
VULTUS	NRPB, raw bands	Sentinel 1 satellite (ESA)
VULTUS	NDVI, NDWI, NDRE, LAI, raw bands	Sentinel 2 satellite (ESA)
CER	Italian study site characteristics	in situ weather station, soil data at the site
CER	BBCH, LAI	local observations
CER	Historical hydrometeorological series	in situ instruments
UNIDEB	Hungarian site characteristics	local observations/instruments
NASA	GQ09 061 (NDVI)	MODIS-Terra
NASA	Level 2 Collection 2	Landsat 8
UNIDEB	Hydrometeorological data series	in situ weather station

UNIDEB	Soil moisture data series	in situ moisture sensor at the site
Hu Met Office	Global radiation	Open Data Server
Hu Water Auth	Historical hydrometeorological and soil moist	drought monitoring server
Agricolus	Weather monitoing and data forecast	Agricolus platform

6.2.3.1 BBCH measurements

Crop phenophases are assessed in a qualitative manner by the daily sampling of corn plants in the field. Results are expressed on the "Biologische Bundesanstalt, Bundessortenamt and CHemical industry (BBCH)" scale (Hack et al., 1992).

6.2.3.2 LAI, reference evapotranspiration and precipitation series in Emilia-Romagna, Italy

The measurement of *Leaf Area Index* (LAI) was carried out through direct methods, which involve the removal of plants in the field on certain test areas and subsequent analyses carried out on the samples collected.

In particular, for the plants collected in the field were subjected to LAI measurements carried out through the computerized analysis of high-definition images. This method involves the collecting of leaves, the calculation of the area using image analysis techniques and the measuring of the weight of dried leaves to derive the ratio between leaf area and mass per unit area. The existing method provides an accurate and reliable means to estimate LAI and is considered to be efficient. However, the application of this method on evergreen species is invasive. [1][2][3]

Plants were harvested in the field on test areas of 1 m^2. The methodology proposed for the direct measurement of the leaf area index requires:

- a fresh leaf vegetation sample
- a scanner (*Mustek A3 600 Pro*)
- an image analysis software (*Fiji ImageJ2*)

After having been calibrated through the scanning of a shape of a known area, the scanner is used to capture the images of the fresh leaf vegetation subsample. The single image captured by the scanner is processed by the analysis software. Subsequent processing leads to the measurement of the area occupied by vegetation in the image. The following operations are carried out to obtain this result:

- **Identification of the geometric characteristics of the image**: The image resolution (dpi) and geometric resolution of the image are detected based on the settings of the scanner.
- **Binarization:** Binarization refers to the process of the assignment of a binary digit for the purpose of the conversion of any image into its black and white equivalent according to the pixel intensities of an RGB image.
- **Adjustment of any noise in the image:** There may be some pixels within binarized geometries that have not been categorized as intended. In this case, their desired classification can be achieved through the application of thresholding methods, through algorithms increasing the contrast of the image or manually, by the selection of the portions of the image not classified as desired.

- **Quantification of the histogram:** By analysing the histogram on the binary image, one can learn the number of pixels associated with the geometry of the image.
- **Area of leaf calculation:** The number of pixels associated with the desired geometry is divided by the total number of pixels in the image. The result is then multiplied with the image area (in this case an A3 sheet).

The result of the analysis of the area of the sub-sample refers to its dry matter to be used for the calculation of the SLA (Specific Leaf Area). The SLA (cm^2 g of dry $matter^{-1}$) can then be multiplied with the total dry matter (g) present in the 1 m^2 test area to obtain the leaf area index (LAI).

CER provided exact, calculated ET_0 values for the Italian site, which were later considered as time series for model input.

6.2.3.3 The organization of evapotranspiration-related datasets in Nyírbátor, Hungary

In order to be able to calculate precise reference evapotranspiration based on the Penmann-Monteith approach, Batortrade Ltd as the cultivator of the Nyírbátor site provided meteorological data for 2020 and 2021 (DavisMet 2020, coordinates: 47° 49' 26", 22° 08' 53", elevation 145 masl.). The station collected data such as:

- Daily minimum, maximum and mean temperature,
- Mean dew point,
- Mean air pressure,
- Daily cumulative precipitation, and
- Wind speed and wind direction.

Furthermore, daily global radiation is also necessary to determine ET_0. Solar insolation can be regarded as spatially less heterogeneous than the aforementioned hydrometeorological variables, therefore the series of the Debrecen weather station located about 70km from the site (47° 29' 25"; 21° 36' 38") provided by the Hungarian Meteorological Service were in this analysis. The dataset is freely available from the odp.met.hu site.

Long-term hydrometeorological, as well as soil moisture data time series can be queried from the nearby drought observatory station located in Nyírlugos, at about 1 km from the study site (47° 49' 34", 22° 06' 15"). The station is operated by the Hungarian Water Authority. The dataset is freely downloadable from the Hungarian drought monitoring site[3].

The station provides the following information:

- Daily mean temperature,
- Soil moisture at 10, 20, 30, 45, 60 and 75 cm,
- Soil temperature at 10, 20, 30, 45, 60 and 75 cm,
- Soil water deficit at 35 and 80 cm,
- Relative air humidity,
- Precipitation, and
- Meteorological drought index.

[3] www.aszalymonitoring.hu/en

The Agricolus platform has also been used in 2021 to monitor the Hungarian case study site to support irrigation and minimize potential crop damage.

6.2.3.4 Construction of the database of remotely sensed data

In contrast to field-based experiments, satellite imagery provides a much more economical and cost-effective and labour and time saving data collection opportunity (Romano et al., 2020). Nowadays, high resolution satellite datasets are easily and freely accessible online. VULTUS designed and deployed a processing remote sensing pipeline that utilizes optical and microwave remote sensing observations from Sentinel-1 and Sentinel-2 satellite imagery to obtain biophysical parameters for vegetation, such as above-ground biomass, LAI and soil moisture. Furthermore, the remote sensing pipeline also provides insights into monitoring tools that integrate and consider the advanced approaches from WP3 and WP5 for monitoring crop growth stages and assessing water retainer management.

SENTINEL 2 Earth observation mission consists of two satellites, Sentinel 2A and Sentinel 2B, phased 180 degrees from each other on the same orbit. Sentinel 2 flies over the Hungarian site every 5 days, at 10:00 am. The NRPB supplied by Sentinel 1 provided turned out not to be useful for any further analysis in the end, since the time series did not show any vegetation development, only freshly ploughed land was distinguishable from already sown arable land (Zhao, 2021).

Moderate Resolution Imaging Spectroradiometer (MODIS) is an imaging sensor, launched into orbit by NASA in 1999 on board of the Terra satellite and in 2002 on board of the Aqua satellite. Terra flies over the area in the morning and Aqua in the afternoon, so they are affected by the differences in solar zenith angle and atmospheric humidity. Terra was chosen as data source, since it flies over the area 3 hours before the Sentinels. MODIS data are freely available on the Earth Data site, operated by the US Geological Survey (USGS, 2020). After gathering the necessary MODIS datasets from the NASA Earth Data portal, the calculation of the NDVI data series for the Nyírbátor and the Emilia-Romagna site was batch processed using the Sentinel Application Platform.

The database of the raw remotely sensed observations includes the extracted calculated vegetation index series at the location of the SENTINEL pixel centers. In the case of SENTINEL-related index values, this is a straightforward solution. In the case of MODIS NDVI, the extracted values were interpolated to the SENTINEL pixel centre coordinates (Zhao, 2021)[4].

6.2.4 The simplified model of crop coefficients (K_c) with VULTUS data

In the current modelling scenario a simplified modelling task of the crop coefficient (K_c) to a 1-dimensional temporal relationship analysis between the environmental factors and remotely sensed images have been performed. The following analysis was carried out parcel-wise annually for the 6 Italian parcels between 2018 and 2020. Since the CER provided hydrometheorological time series for two-two selected parcels for each year, thus not all 18 scenarios have been modelled. Furthermore, the large arable land for the years of 2020 and 2021 in Hungary was also examined. The current chapter introduces step by step, the analysis for the Italian site for 2018-2020, based on the example

[4] As part of the WATERAGRI project, a wide benchmark has been implemented/was applied to analyse the effects of various interpolation methods, which cannot be introduced in the current report due to page number constraints.

of the parcel No 8, maize field (Figure 47). The results of the other sites are published in Appendix 3-Appendix .5.

In the case of the modelling workflow discussed, each site subject to the analysis was considered as a point-type entity, with temporally changing environmental variables (Table 12), which made it possible to assess the relationship between natural and theoretical processes. The steps of the analysis were as follows:

(1) Determination of the reference evapotranspiration based on the Penman – Monteith approach.
(2) Different crop coefficients were assigned to different time periods, in accordance with the plant development stages observed for the crop under study.
   - BBCH phenological phases were determined every two weeks both for the Italian sites and the Hungarian site. Due to non-continuous in-situ observations, the proper identification of the first Kc break point is uncertain, which results in a temporal uncertainty of up to 7 days.
   - Since the theoretical K_c sequence presented in the FAO-56 document is unnaturally rectangular and does not reflect the natural process of canopy saturation, the break points of the series were curved by the application of two technical approaches. The solution called *"FAO-56 curved"* was to cut 10 days around the break points and implement the spline algorithm to estimate missing values. The other approach was the so-called "MidPoint Spline", where only the middle stage plateau was determined by its middle point and the length of the plateau phase (Figure 48).

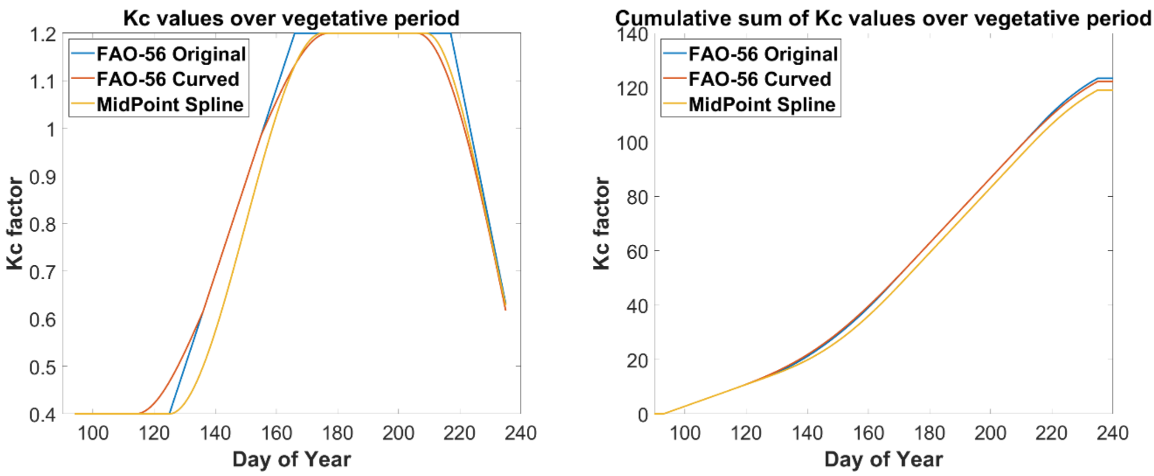

Figure 48: Calculated crop coefficients and their cumulative time series

Finally, the theoretical crop evapotranspiration time series was determined for each of the three K_c, as a combination of the reference evapotranspiration and the crop coefficient time series. The estimated ET_c values seem more uncertain around the K_c break points (Figure 49).

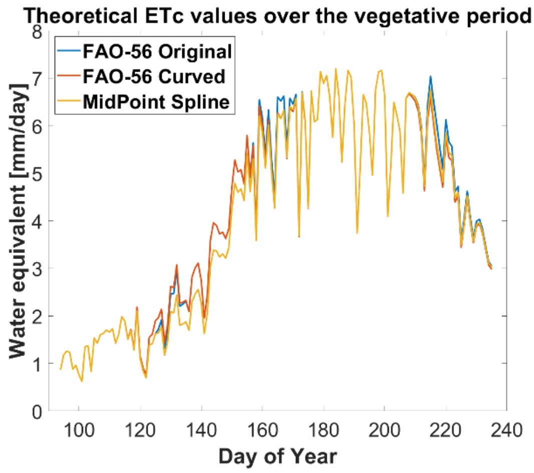

Figure 49: Calculated theoretical crop evapotranspiration

(3) Independently from the first step, the 1-dimensional time series of the pixel centres of all of the following indices were established simultaneously for every year and for each specific parcel: NDVI, NDWI, NDRE, NDREw, LAI and NPBR. This step included:
- The filtering out of outlier index values from the time series for all pixel centres individually and the consideration of cloud cover masks and index limit values.
- In order to minimize the effect of missing values, the median of the contemporal pixel values was assigned to each observed time instant. The method provides one single time sequence for each distinguished spectral index, which is from now on considered representative for the whole parcel under study (Figure 50).

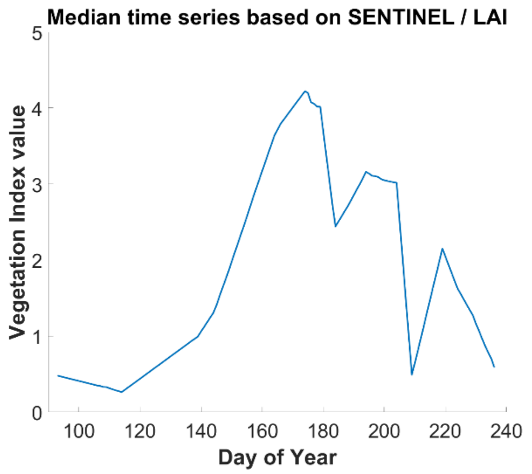

Figure 50: Estimated median type time series of the Leaf Area Index, for the Italian Field 8, in 2018

- Estimation of the empirical K_c curves based on the spectral indices by the fitting of the index-based time series to the theoretical K_c trend. Until this moment, the index values are only known at the time instants observed. The missing values have been estimated by the application of the Piecewise Cubic Hermite Interpolating Polynomial (PCHIP) approach (Figure 51).

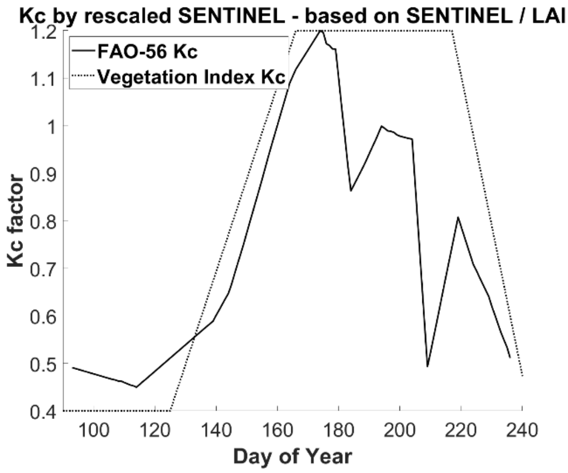

Figure 51: Estimated Kc series compared to the FAO-56 theoretical Kc for Italian parcel No. 8 in 2018

(4) The combination of the determined ET_0 and the estimated index-based and theoretical K_c series provides several alternative crop evapotranspiration (ET_C) estimates. The cumulative sum of the crop evapotranspiration determines the amount of water evaporated during the vegetative period (Figure 52).

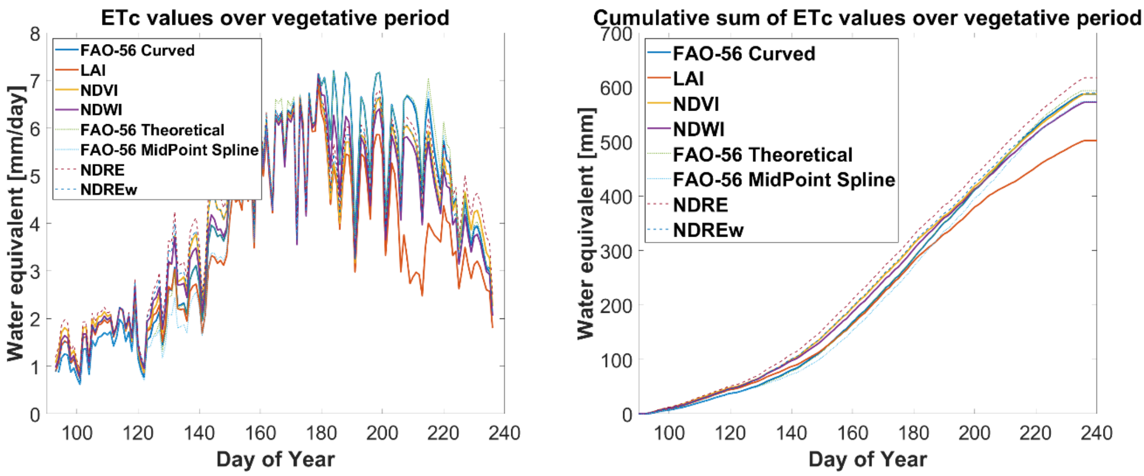

Figure 52: Comparison of crop evapotranspiration and its cumulative series based on the spectral indices analysed and theoretical models for Italian parcel No. 8 in 2018

(5) The difference between the cumulative sum of the crop evapotranspiration and precipitation (incl. irrigation) gives the cumulative water budget over the area. This factor indicates how much irrigation is needed to maintain soil humidity on the same level as it is at the beginning of the vegetative period (Figure 53).

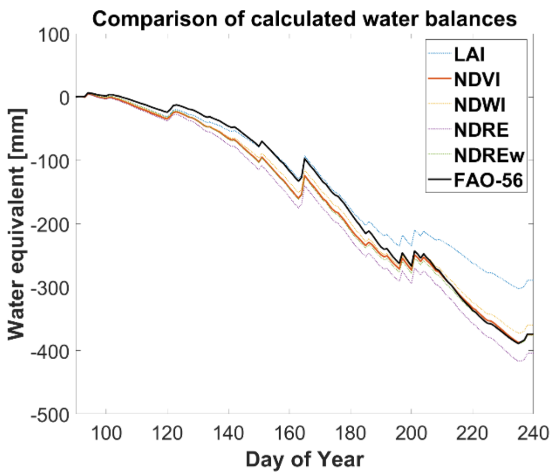

Figure 53: Cumulated water balance for the Italian Field 8, in 2018

There is significant correlation between the analyzed ET_c curves, thus a proper regression model may be capable to describe the real crop evapotranspiration based on any other vegetation index (Table 13). The correlation matrix indicates, that Leaf Area Index is less effective to reproduce the temporal pattern of the theoretical curves, while NDVI seems the most effective to predict ET_c.

Table 13: Correlation coefficients between estimated ETc curves

	FAO-56			Spectral indices				
	Original	Curved	MidPoint	LAI	NDRE	NDREw	NDVI	NDWI
Original	1.00	0.98	1.00	0.89	0.93	0.94	0.94	0.94
Curved	0.98	1.00	0.98	0.85	0.89	0.89	0.90	0.91
MidPoint	1.00	0.98	1.00	0.89	0.94	0.94	0.95	0.95
LAI	0.89	0.85	0.89	1.00	0.93	0.95	0.94	0.95
NDRE	0.93	0.89	0.94	0.93	1.00	0.99	1.00	0.99
NDREw	0.94	0.89	0.94	0.95	0.99	1.00	1.00	1.00
NDVI	0.94	0.90	0.95	0.94	1.00	1.00	1.00	0.99
NDWI	0.94	0.91	0.95	0.95	0.99	1.00	0.99	1.00

(6) Finally, the cross-validation of the results presents the relationship between the index-based and theoretical crop evapotranspiration. In this step, both linear and power regression models were evaluated (Table 14). Since the LAI-based model has a somewhat exponential nature compared to the other indices, be capable of expressing the non-linearity of the relationship between the factors investigated. In the current case, the power model of the Normalized Difference Water Index generates the least errors for the different metrics (SSE: sum of squared error; R-sq: R-square: Coeff. of Determination; DFE: Degrees of Freedom error; Adj. R-sq: Same as R-squared with adjustment for the number of coefficients; RMSE: Root Means Square Error; nRMSE: normalized Root Mean Square Error).

Table 14: Results of regression between calculated empirical and theoretical FAO-56 evapotranspiration time series

	SSE	R-sq	DFE	Adj. R-sq	RMSE	nRMSE	a	b	formula
NDWI	18.86	0.95	140	0.95	0.37	0.09	1.46	0.75	power
NDWI	20.30	0.95	140	0.95	0.38	0.10	0.79	0.82	linear
NDRE	29.96	0.93	140	0.93	0.46	0.11	1.80	0.66	power
NDVI	27.21	0.93	140	0.93	0.44	0.11	1.60	0.70	power
NDREw	31.97	0.92	140	0.92	0.48	0.12	1.58	0.71	power
NDVI	32.20	0.92	140	0.92	0.48	0.12	0.78	0.97	linear
NDRE	36.84	0.91	140	0.91	0.51	0.12	0.77	1.20	linear
NDREw	36.32	0.91	140	0.91	0.51	0.12	0.79	0.94	linear
LAI	69.06	0.81	140	0.81	0.70	0.20	1.28	0.74	power
LAI	69.54	0.81	140	0.81	0.70	0.20	0.69	0.74	linear

6.2.5 Calculation of ET_C for 2020 and 2021 with using RS based K_c calculation

In this modelling scenario, the advantages of the high temporal resolution of MODIS NDVI and the high spatial resolution of the variety of SENTINEL NDVI indices were exploited. Although the MODIS and SENTINEL products are obtained from different sensors, a significant relationship can be presumed between them on the temporal domain.

This Chapter takes three approaches to the estimation of missing SENTINEL pixel values:

1. Co-regionalization: Bivariate spatial interpolation with cokriging

Using some regression equation (in this case, the linear and the power model were analysed) between the SENTINEL and MODIS time series by

2. Local time series of MODIS pixel centres or

3. Median time series of the co-temporal MODIS pixel centres.

The first option is to densify MODIS images spatially via bivariate geostatistical interpolation such as the cokriging algorithm. In this case, the spatial pattern of the SENTINEL pixel values would guide the estimation with the minimization of estimation covariance. This approach inherently requires a high correlation between SENTINEL and MODIS NDVI values for the same time interval. As it can be seen in Table 15, there is no significant correlation between the two data products, therefore this approach cannot be applied. Optimally, the proportion of the vegetation cover should be equally represented on both data products. However, since NDVI expresses the ratio between the soil and chlorophyll reflectance and environmental conditions (the availability of water and nutrients) are spatially heterogeneous, the pace of development inevitably varies in space.

The second approach attempts to exploit the temporal profile of both the SENTINEL and the MODIS images, by considering each time series of MODIS pixels. In order to be able to perform this analysis, we need to predict the MODIS NDVI for exactly the same geolocations, therefore MODIS pixel values were spatially interpolated explicitly to the SENTINEL pixel centres with univariate ordinary kriging. The approach requires a stationary spatial covariance function valid for the whole study area. Thereafter, MODIS time series can be constructed, and correlations between the SENTINEL and MODIS NDVI can be determined for each pixel separately. The regression equation between the two products enables the estimation of the SENTINEL index values, when only MODIS images are available.

Table 15: Preprocessing methodology of the MODIS and SENTINEL NDVI time series

	Correl	Linear		Power	
		nRMSE	RMSE	nRMSE	RMSE
Coregionalization	0.25	*not applicable*			
Univariate interpolation	0.68	0.247	0.171	0.257	0.178
Median time series model	0.81	0.134	0.194	0.13	0.189

In contrast to the above-mentioned method, where each MODIS pixel represents the reflectance sum over the observed area, a third, novel approach has been developed to minimize the effects of sub-pixel spectral mixtures on the MODIS values. This type of error is related to the asphalt roads around the study site and an irrigation channel with dense natural vegetation running across the centre of the study site. The proportion of the pixels affected is insignificant compared to all available pixels, therefore the sequence of the median values of contemporary pixel values can presumably minimize the effects of sub-pixel spectral mixtures. Finally, this median time series can be used to estimate missing SENTINEL values.

According to Table 15, the sub-pixel spectral mixture has a more significant effect on the MODIS pixels than the locally varying development stage of the vegetation. Figure 54 shows the cumulative statistical distribution of the correlation strength between the MODIS-based median model and the observed SENTINEL time series. It seems like the median time series based model clearly outperforms the local varying time series models

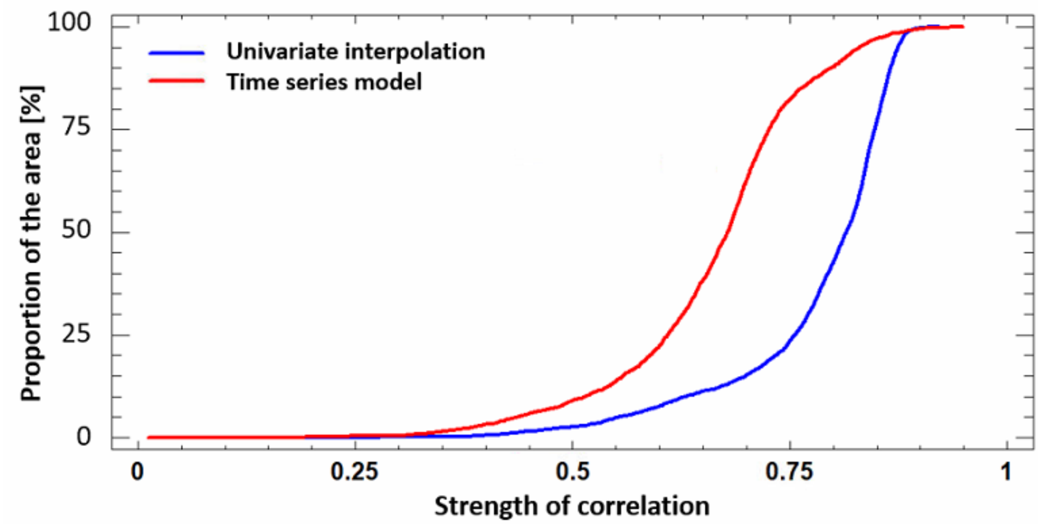

Figure 54: Comparison of pixel-wise correlation coefficients by two different approaches: A: Interpolated MODIS NDVI vs SENTINEL NDVI, B: Modelled MODIS NDVI vs SENTINEL NDVI

The maps below present the spatial pattern of correlation strengths and regression parameters and are projected to the *"Hungarian Datum 1972 Egységes Országos Vetület"* system (EPSG code: 23,700).

The nearby asphalt cover seems to decrease correlation strength and increase normalized RMS-error significantly in the area of the field close to its eastern edge (Figures 55, 56). However, the median time series mode can filter this type of error effectively (Figures 57, 58).

The effect of the spectral mixture can be evaluated pixel-wise after the calculation of the crop evapotranspiration according to the classic workflow of the parcel-scale crop evapotranspiration calculation described in the previous Chapter.

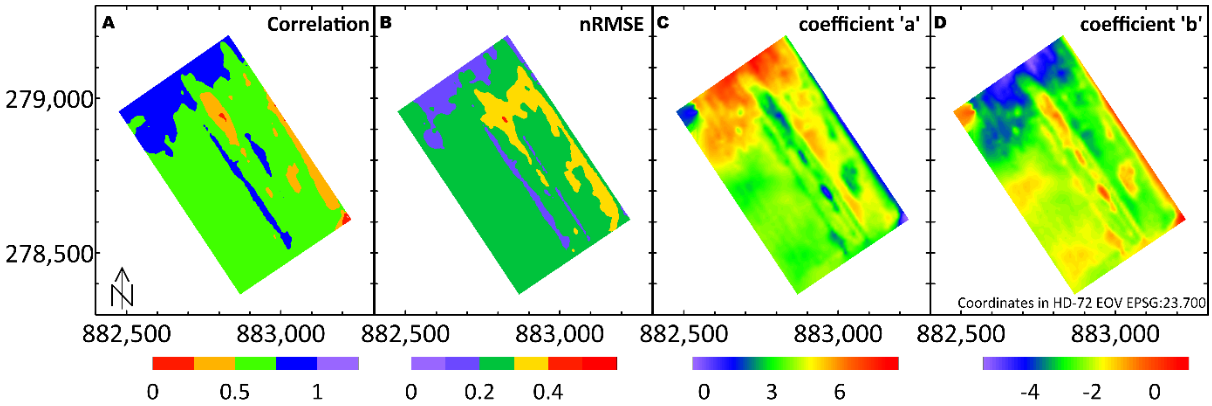

Figure 55: Interpolated MODIS pixel values to Sentinel pixel values – linear model: A: pixel-wise correlation between estimated MODIS & direct SENTINEL observation, B: nRMSE, C: spatial pattern of linear regression coefficient 'a', D: spatial pattern of linear regression coefficient 'b'

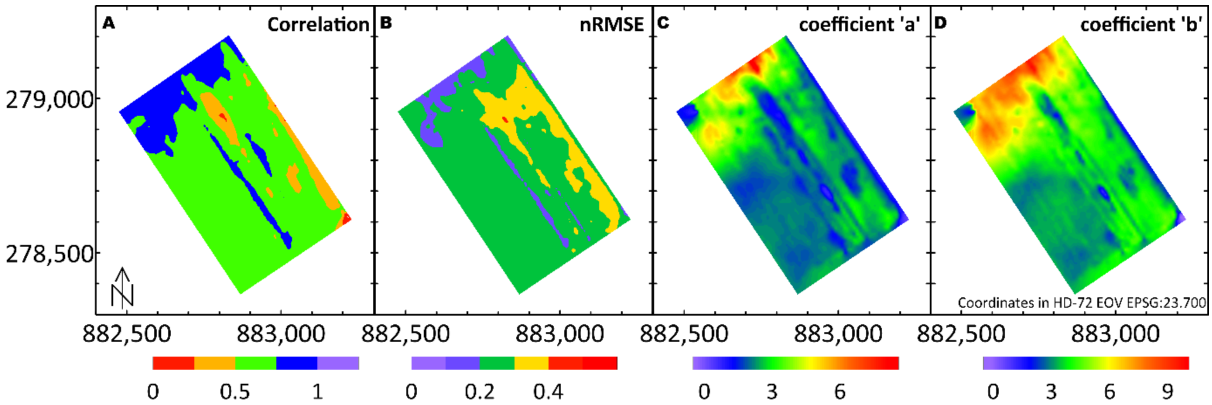

Figure 56: Maps of interpolated MODIS pixel values to Sentinel pixel values – power model: A: pixel-wise correlation between estimated MODIS & direct SENTINEL observation, B: nRMSE, C: spatial pattern of power-type regression coefficient 'a', D: spatial pattern of power-type regression coefficient 'b'

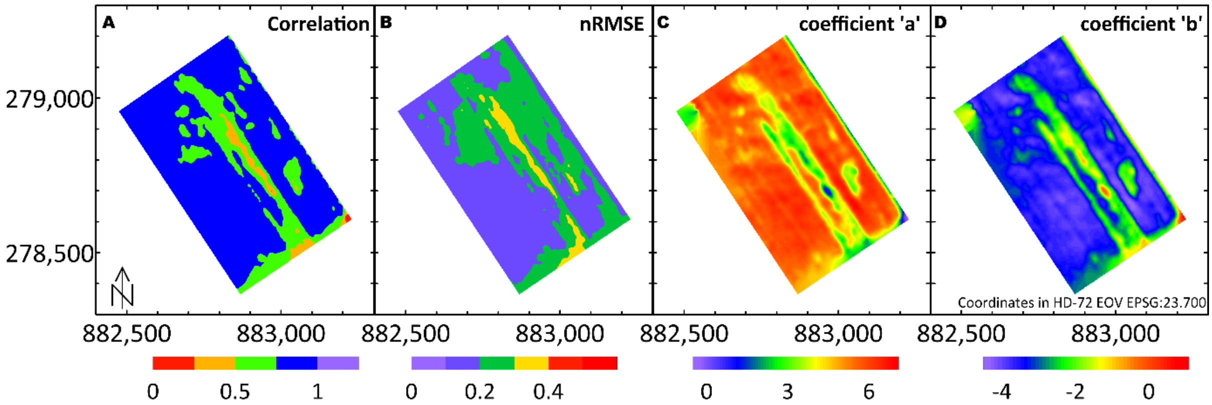

Figure 57: Maps of modeled MODIS optimal time series to Sentinel pixel values – linear relationship: A: pixel-wise correlation between estimated MODIS & direct SENTINEL observation, B: nRMSE, C: spatial pattern of linear regression coefficient 'a', D: spatial pattern of linear regression coefficient 'b'

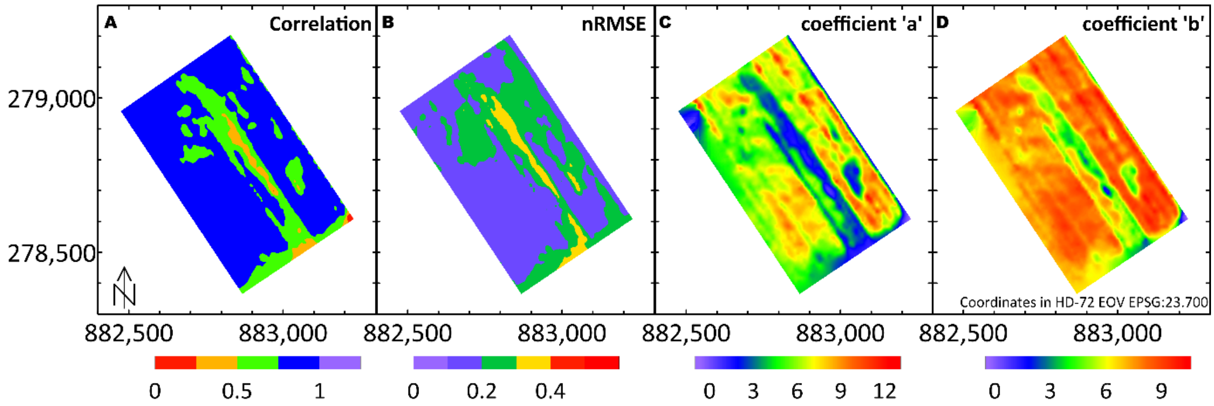

Figure 58: Maps of modeled MODIS optimal time series to Sentinel pixel values – power-type relationship: A: pixel-wise correlation between estimated MODIS & direct SENTINEL observation, B: nRMSE, C: spatial pattern of power-type regression coefficient 'a', D: spatial pattern of power-type regression coefficient 'b'

6.2.5.1 Analysis of Sentinel-type Indices vs. MODIS NDVI model

While the previous Chapter indicated a significantly strong correlation between the spectral indices, in this Chapter, we attempt to check whether any other available index is worth being considered in the analysis. As the highest resolution spectral bands (Red and near IR) enable the effective use of the MODIS - NDVI index, Figure 59 and Figure 60 suggest that Sentinel-type NDWI closely mimics the efficiency of the NDVI index, while LAI shows mediocre and NDRE shows very weak performance if used in a hybrid MODIS – Sentinel fusion model.

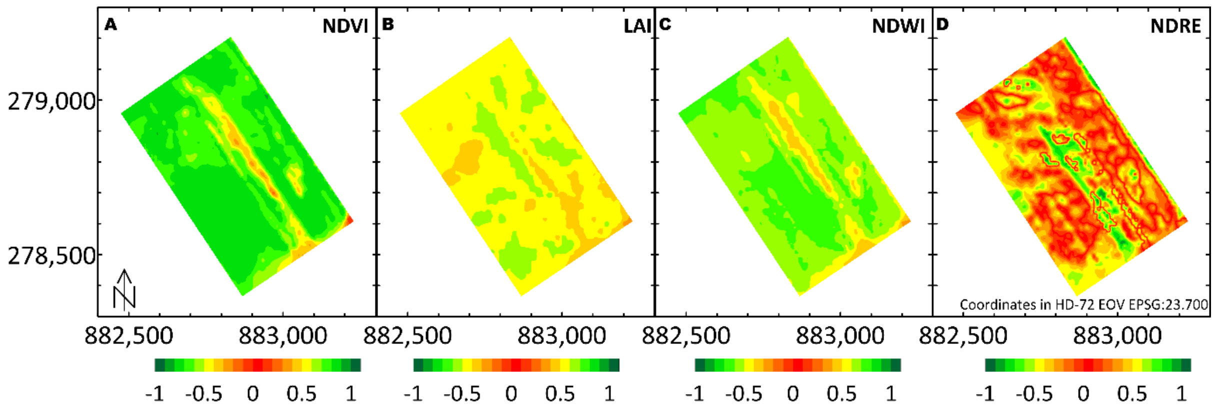

Figure 59: Correlation coefficients: MODIS-NDVI vs SENTINEL products: A: NDVI, B: LAI, C: NDWI, D: NDRE

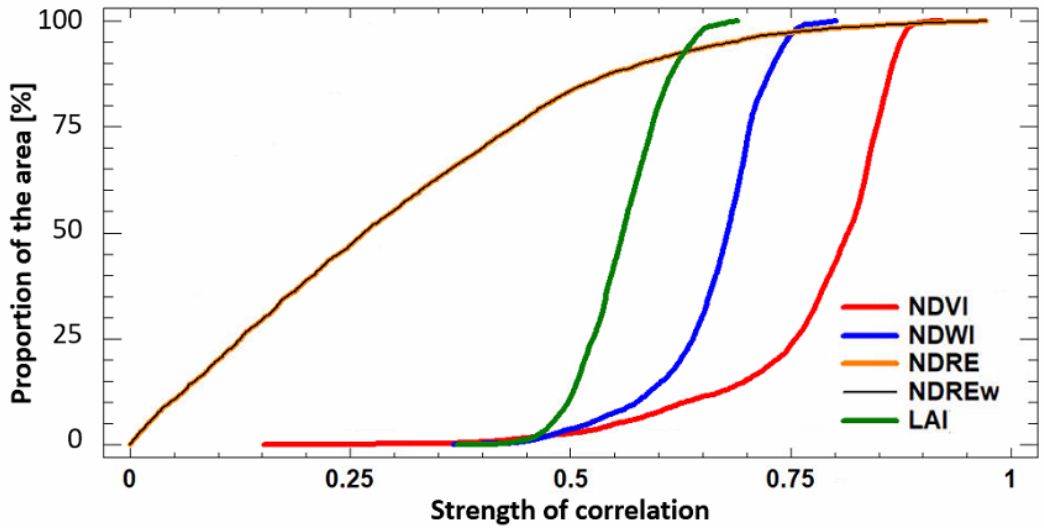

Figure 60: Comparison of correlation coefficient histograms over the field

6.2.5.2 Estimation of the water demand on the Nyírbátor field

The reference evapotranspiration series has been calculated from the combination of the in-situ sensors using the Penman-Monteith approach, following the methodology introduced in Section 6.2.4. The high spatio-temporal dataset of NDVI pixel values has been calculated by the median-model based technique introduced in Section 6.2.5.1. In addition, the crop coefficient from the FAO-56 paper determines the typical Kc values for maize. The transformation of the NDVI values can be carried out by the fitting of the unstructured statistical distribution of the whole set of NDVI values to the statistical distribution of the unstructured FAO-56 Kc series. The method is analogous with the normal-score transformation well-known from geostatistics. The method ensures that the relative difference between the Kc values just calculated both in the spatial and temporal context can be retained for each pixel centre.

The combination of the ET_o time sequence with the now available Kc spatiotemporal values and the irrigation data series gives the water budget relative to the conditions at the starting time of the simulation. Figure 61 shows the relative water balance of the area at some selected time instant. The images make it clear that the relative change of water balance from the time of sowing in March to September in the rainy year of 2020 was the same as until July in the much more arid year of 2021 (Figure 61). The variable spatial distribution of relative water balance change indicates the importance of the implementation of precision irrigation.

The patterns of crop evapotranspiration can be expressed both in map and time series format. Figure 62 shows that the median of the pixel-wise separately estimated water balance sequences closely represents the FAO-56-based theoretical evapotranspiration sequence.

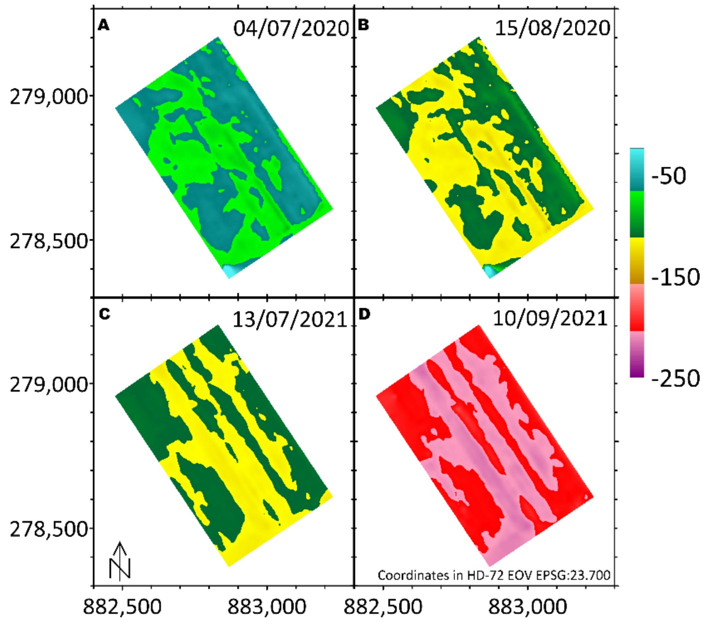

Figure 61: Comparison of the spatial pattern of estimated water balance on A: 4th of July 2020; B: 15th of August 2020.; C: 13th of July 2021; D: 10th of September 2021 on the Nyírbátor site

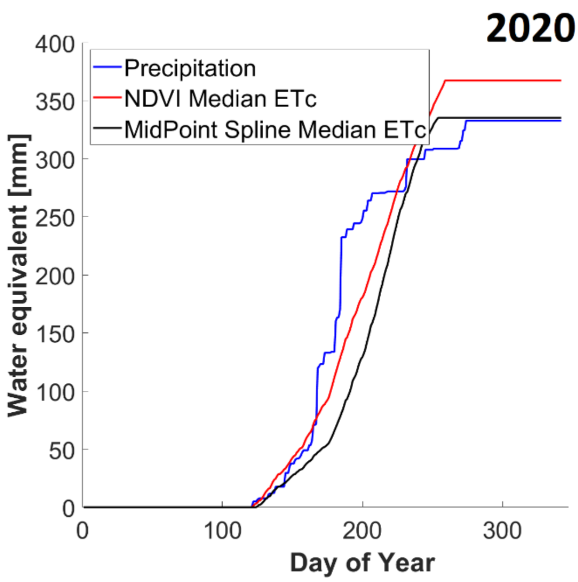

Figure 62: Cumulative water deficit estimate by NDVI based crop evapotranspiration for 2020

6.2.6 NDVI-based ETc estimations in water balance modelling

NDVI-based ET_c values of maize for the vegetation period of 2021 were integrated into the previously validated Hydrus-based soil physical model (Chapter 4.1). The aim was to assess how ET_c values correspond to measured soil moisture data.

First, the NDVI-based ET_c values were calculated for the maize vegetation period in 2021 for the Hungarian case study site. The sowing date of the maize was 21 May, 2021 and the harvesting date was 13 September, 2021. The entire time period was divided into 4 crop development stages

(Table 16). Precipitation data were collected from a hydro-meteorological station (DavisMET) located next to the site.

Table 16: Lengths and VI based ET_c ranges according to the crop development stages.

Stage	Indicators	Time period, T [days]	ET_c range, [mm·day^{-1}]
Initial	Planting date (or the start of new leaves for perennials) to 10% ground cover.	21 May, 2021 – 24 June, 2021 *(35 days)*	0.99-4.41
Crop development	10% ground cover to effective full cover, about 60-70% coverage for tree crops and 70-80% for field and row crops.	25 June, 2021 – 30 July, 2021 *(36 days)*	2.00-6.40
Mid-season	Effective full cover to maturity, indicated by yellowing of leave, leaf drop, browning of fruit.	31 July, 2020 – 26 August, 2021 *(27 days)*	1.03-5.12
Late-season	Maturity to harvest: K_c value could be high, if the crop is irrigated frequently until fresh harvest or low, if the crop is allowed to dry out in the field before harvest.	27 August, 2021 – 13 September, 2021 *(18 days)*	1.10-3.18

NDVI-based ET_c served as an input for the Hydrus-based soil physical model for the simulation of soil moisture content changes. For comparison, the soil moisture profile measured at 15 cm depth was considered. The water content at sowing time was 25.6% according to the soil moisture sensor and used as initial condition. Simulated soil moisture values were higher than the measured ones. The difference was the highest from the second week of June until the middle of July (initial and first half of the development stage). The maximum differences exceeded 10% in the middle of that period (Figure 63).

The temporal dynamics of measured and modelled soil moisture contents were compared based on a curve estimation procedure for the entire investigated time period considering the different crop development stages. The software Grapher 17 was used for the estimation of regression models (Table 17). R^2 values were determined for each crop development stage, and their weighted average value for the entire time period was also calculated. R^2 values were found to be the highest for the mid-season and the late-season stages and the lowest for the initial stage.

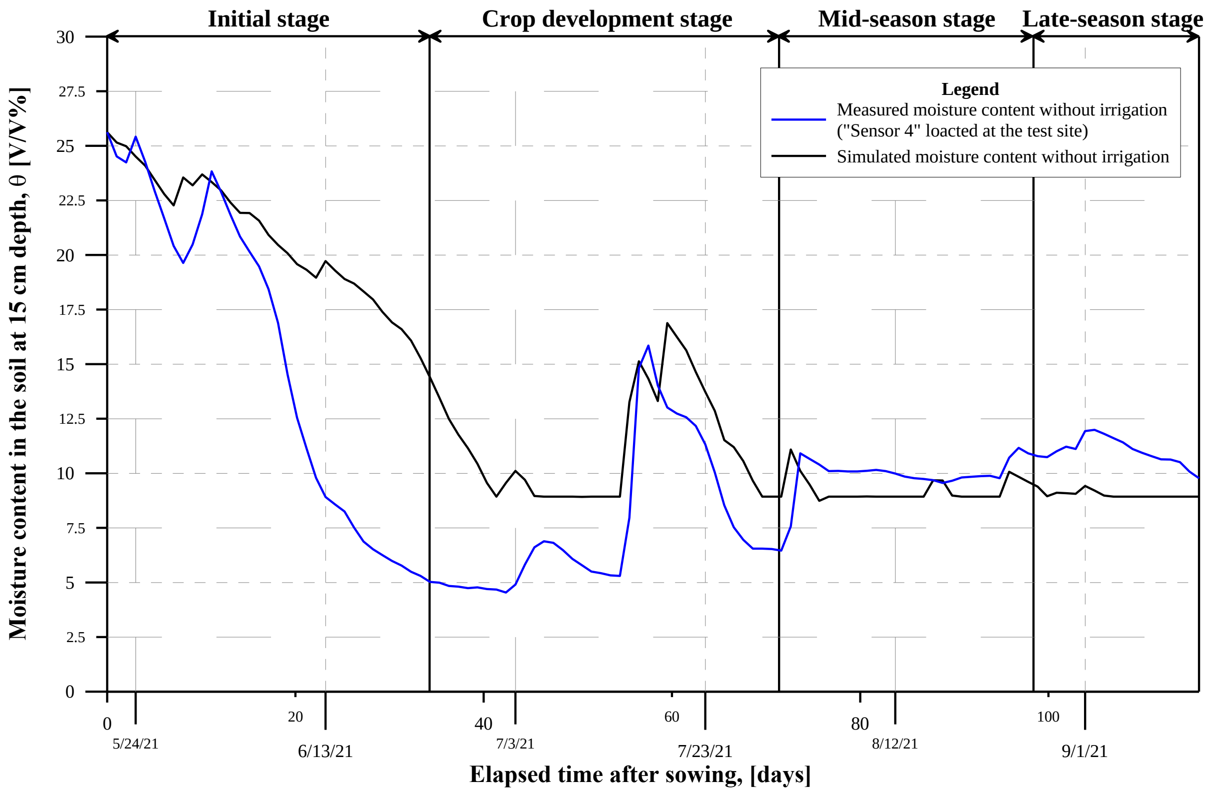

Figure 63: Measured and simulated soil moisture contents for the Nyírbátor site in the vegetative period of 2021

Table 17: The calculated R^2 values for each crop development stage and the weighted average value for the entire period

Stage	Coef. of determination (R^2)
Initial	0.21
Crop development	0.45
Mid-season	0.67
Late-season	0.53
Average	0.44

The weak prediction in the initial and the development stages may be explained by the extreme weather conditions in June 2021, which has been the driest and the third hottest June since 1901 (HMS, 2021).

Results suggest at the same time that NDVI-based ET_c models perform well for the estimation of maize water balance in the mid-season stage. July and August are the most important months from the point of view of irrigation for two reasons. First, based on long-time historical climate data, this time period is most affected by drought. Second, maize requires the largest amount of water during its flowering stage.

7 Conclusions

Physically-based modelling and remote sensing-based vegetation status surveying can be used for accurate irrigation scheduling. A Finnish case study shows that controlled tile drainage systems can be an alternative for irrigation in areas where shallow groundwater is available in addition to surface water. However, shallow groundwater and/or soil compaction can also contribute to excess inland water. This may occur even if there are drought periods in a year (e.g. in the Pannonian region), resulting in spots with a low crop yield. A LiDAR-based digital elevation model was found to provide appropriate data to identify sites affected by excess inland water. The spots identified can be used as spatial input data to compile a variable rate irrigation prescription map for imposing reduced (or zero) irrigation at areas more vulnerable to the occurrence of excess inland water.

The water balance was also assessed for sites with physically-based models. Hydrus was used to model soil moisture changes at the Hungarian case study site. Furthermore, an analysis with different meteorological conditions forcing the HydroGeoSphere model for the Lower Silesia case study site was performed to demonstrate the model's potential in representing all important components of the water cycle in an integrated and physically explicit way.

The potential of the use of remote sensing-based vegetation indices in irrigation scheduling was also assessed. Besides SPI (Standardized Precipitation Index), CWSI (Crop Water Stress Index) was also an effective tool to detect vegetation stress at the Finnish case study site. Landsat-based wheat yield prediction models were established based on data collected from the Pannonian region, which predicts yield six weeks before harvesting. This information can reduce the impacts of possible yield losses if provided to farmers who can refine the irrigation schedules of these fields.

A model concept for crop evapotranspiration estimation was developed based on vegetation indices calculated from satellite imagery. Several combinations of sensors and remote sensing products were tested to use in ETc modelling potentially. This approach was tested both at the Hungarian and the Italian case study sites. Remote sensing-based analysis of crop evapotranspiration, combined with physically-based modelling, appears to be a promising method in water balance modelling of maize fields, especially if these fields are in summer when the crop is fully developed. However, the remotely sensed information verification is essential for the proper utilization of the remote sensing data in ET_c modelling and predicting the spatio-temporal dynamics of crop yield, evapotranspiration, and irrigation demands.

We need further benchmark scenarios to improve both physically-based models and satellite-based crop evapotranspiration models to achieve more accurate and valid simulations. Further research and validations will be done under Task 5.10 of the WATERAGRI project to generate more reliable remote sensing-based water balance models, which can support the efficiency of irrigation scheduling.

8 References

Abatzoglou, J. T., Dobrowski, S. Z., Parks, S. A., Hegewisch, K. C., 2018. TerraClimate, a high-resolution global dataset of monthly climate and climatic water balance from 1958–2015. Scientific Data 5 1–12.

AghaKouchak, A., Farahmand, A., Melton, F. S., Teixeira, J., Anderson, M. C., Wardlow, B. D., Hain, C. R., 2015. Remote sensing of drought: Progress, challenges and opportunities. Reviews of Geophysics 53, 452–480.

Ahopelto, L., Veijalainen, N., Guillaume, J.H., Keskinen, M., Marttunen, M., Varis, O., 2019. Can there be Water Scarcity with Abundance of Water? Analyzing Water Stress during a Severe Drought in Finland. Sustainability 2019, Vol. 11, Page 1548 11, 1548.

Ala-Aho, P., Soulsby, C., Wang, H., Tetzlaff, D., 2017. Integrated surface-subsurface model to investigate the role of groundwater in headwater catchment runoff generation. A minimalist approach to parameterisation. J, Hydrol., 547, 664-677. doi: 10.1016/j.jhydrol.2017.02.023

Allen, R., Pereira, L., Raes, D., Smith, M., Parte, C., 2006. Evapotranspiración del cultivo en condiciones no estándar ET c bajo condiciones de estrés hídrico, Evapotranspiración del cultivo Guías para la determinación de los requerimientos de agua de los cultivos. ESTUDIO FAO RIEGO Y DRENAJE 56.

Allen, R. G., Pereira, L. S., Raes, D., Smith, M., 1998. Crop evapotranspiration - Guidelines for computing crop water requirements - FAO Irrigation and drainage paper 56. FAO - Food and Agriculture Organization of the United Nations Water Resources, Development and Management Service Rome, Italy. 300.

Allen, R. G., Tasumi, M., Trezza, R., 2007. Satellite-Based Energy Balance for Mapping Evapotranspiration with Internalized Calibration (METRIC)—Model. Journal of Irrigation and Drainage Engineering 133, 380–394.

Andales, A. A., Chávez, J. L., Bauder, T. A., 2011. Irrigation scheduling: the water balance approach. Doctoral dissertation, Colorado State University Libraries. 6.

Anderson, M. C., Hain, C., Wardlow, B., Pimstein, A., Mecikalski, J. R., Kustas, W. P., 2011. Evaluation of Drought Indices Based on Thermal Remote Sensing of Evapotranspiration over the Continental United States. Journal of Climate 24, 2025–2044.

Angal, A., Xiong, X., Shrestha, A., 2020. Cross-Calibration of MODIS Reflective Solar Bands with Sentinel 2A/2B MSI Instruments. In IEEE Transactions on Geoscience and Remote Sensing, vol. 58, no. 7, pp. 5000-5007, July 2020, doi: 10.1109/TGRS.2020.2971462.

Aquanty, Inc., 2021. HydroGeoSphere. A three-dimensional numerical model describing fully-integrated subsurface and surface flow and solute transport. Waterloo.

Asner, G. P., Alencar, A., 2010. Drought impacts on the Amazon forest. The remote sensing perspective. New Phytologist 187, 569–578.

Asrar, G., Fuchs, M., Kanemasu, E. T., Hatfield, J.L., 1984. Estimating Absorbed Photosynthetic Radiation and Leaf Area Index from Spectral Reflectance in Wheat 1. Agronomy Journal 76, 300–306.

Asrar, G., Myneni, R. B., Kanemasu, E. T., 1989. Estimation of plant-canopy attributes from spectral reflectance measurements. Theory and applications of optical remote sensing 252–296.

Bai, T., Zhang, N., Mercatoris, B., Chen, Y., 2019. Jujube yield prediction method combining Landsat 8 Vegetation Index and the phenological length. Comput. Electron. Agric. 2019, 162, 1011–1027.

Basnyat, P., McConkey, B., Lafond, G. P., Moulin, A., Pelcat, Y., 2004. Optimal time for remote sensing to relate to crop grain yield on the Canadian prairies. Can. J. Plant Sci. 2004, 84, 97–103.

Becker-Reshef, I., Vermote, E., Lindeman, M., Justice, C., 2010. A generalized regression based model for forecasting winter wheat yields in Kansas and Ukraine using MODIS data. Remote Sens. Environ. 2010, 114, 1312–1323, doi:10.1016/j.rse.2010.01.010.

Biro, S., Apáti, F., Szőllősi, L., Szűcs, I., 2011. The economic context of irrigation development. In Hungarian In Water Use and Irrigation Development in Hungarian Agriculture (in Hungarian);

Biro, S., Kapronczai, I., Szűcs, I., Váradi, L., Eds., 2011. Agricultural Research Institute: Budapest, Hungary, 2011; pp. 45–74.

Boken, V. K., Shaykewich, C. F., 2002. Improving an operational wheat yield model using phenological phase-based normalized difference vegetation index. Int. J. Remote Sens. 2002, 23, 4155–4168, doi:10.1080/014311602320567955.

Bonton, A., Bouchard, C., Rodriguez, M. J., Therrien, R., 2012. Calibration and validation of an integrated nitrate transport model within a well capture zone. J. Contam, Hydrol., 18, 1-18. doi: 10.1016/j.jconhyd.2011.10.007

Broge, N.H., Leblanc, E., 2001. Comparing prediction power and stability of broadband and hyperspectral vegetation indices for estimation of green leaf area index and canopy chlorophyll density. Remote Sensing of Environment. Doi:10.1016/S0034-4257(00)00197-8

Brook A, De Micco., A, Battipaglia., D, Erbaggio., G, Ludeno., A, Catapano., G, Bonfante I., 2020. A smart multiple spatial and temporal resolution system to support precision agriculture from satellite images: Proof of concept on Aglianico vineyard, Remote Sensing of Environment, vol 240, 2020, 111679, doi: 10.1016/j.rse.2020.111679.

Brunner, P., Simmons, C. T., 2011. HydroGeoSphere. A fully Integrated, Physically Based Hydrological Model. Ground Water, 50(2), 170-176. doi: 10.1111/j.1745-6584.2011.00882.x.

Buckingham, E., 1907. Studies on the movement of soil moisture, Bureau of Soils, Bulletin, 38, Washington D.C., U.S.Department of Agriculture. URL: https://archive.org/details/studiesonmovemen38buck.

Cashion, J., Lakshmi, V., Bosch, D., Jackson, T.J., 2005. Microwave remote sensing of soil moisture. Evaluation of the TRMM microwave imager (TMI) satellite for the Little River Watershed Tifton, Georgia. Journal of Hydrology 307, 242–253.

Čerekovic, N., Todorovic, M., Snyder, R.L., 2010. The relationship between leaf index area and crop coefficient for tomato crop grown in southern Italy. Euroinvent.

Dann, R., Close, M., Flintoft, M., Hector, R., Barlow, H., Thomas, S., Francis, G., 2009. Characterization and estimation of hydraulic properties in an alluvial gravel vadose zone. Vadose Zone Journal, 8(3), 651–663. https://doi.org/10.2136/vzj2008.0174

Darvishzadeh, R., Skidmore, A., Schlerf, M., Atzberger, C., Corsi, F., Cho, M., 2008. LAI and chlorophyll estimation for a heterogeneous grass-land using hyperspectral measurements. ISPRS J. Photogramm. Remote Sens. 2008, 63, 409–426, doi:10.1016/j.isprsjprs.2008.01.001.

DAVISMET.,2020.VantageVueWeatherStationSpecSheets.www.davisinstruments.com/product_documents/weather/spec_sheets/6250_6351_57_SS.pdf

Davison, J. H., Hwang, H. T., Sudicky, E. A., Lin, J. C., 2015. Coupled atmospheric, land surface, and subsurface modeling: Exploring water and energy feedbacks in three dimensions. Adv. Water Resour., 86, 73-85. doi: 10.1016/j.advwatres.2015.09.002

de Rooij, R., 2017. New insights into the differences between the dual node approach and the common node approach for coupling surface-subsurface flow. Hydrol. Earth Syst. Sci., 21, 5709-5724. doi: 10.5194hess-21-5709-2017

de Schepper, C., Therrien, R., Refsgaard, J. C., He, X., Kjaergaard, C., Iversen, B. V., 2017. Simulating seasonal variations of tile drainage discharge in an agricultural catchment. Water Resour. Res., 53, 3896-3920. doi: 10.1002/2016WR020209

de Vries, F.W., Acquay, H., Molden, D., Scherr, S. J., Valentin., C, Cofie, O., 2003. Integrated land and water management for food and environmental security. Research Report - Comprehensive Assessment of Water Management in Agriculture.

Delécolle, R., Maas, S. J., Guérif, M., Baret, F., 1992. Remote sensing and crop production models: Present trends. ISPRS J. Photogramm. 1992, 47, 145–161, doi:10.1016/0924-2716(92)90030-D.

Dempewolf, J., Adusei, B., BeckerRehef, I., Hansen, M., Potapov, P., Khan, A., Barker, B., Wheat Yield Forecasting for Punjab Province from Vegetation Index Time Series and Historic Crop Statistics. Remote Sens. 2014, 6, 9653–9675, doi:10.3390/rs6109653.

Deutsch, C. V., Journel, A. G., 1998. GSLIB. Geostatistical Software Library and User's Guide. Oxford, New York: Oxford University Press.

Di, N., Wang, Y., Clothier, B., Liu, Y., Jia, L., Xi, B., Shi, H., 2019. Modeling soil evaporation and the response of the crop coefficient to leaf area index in mature Populus tomentosa plantations growing under differentsoilwateravailabilities. Agriculturaland Forest Meteorology. <https://doi.org/10.1016/j.agrformet.2018.10.004>

Djaman, K., O'neill, M., Owen, C. K., Smeal, D., Koudahe, K., West, M., Allen, S., Lombard, K., Irmak, S., 2018. Crop evapotranspiration, irrigation water requirement and water productivity of maize from meteorological data under semiarid climate. Water (Switzerland).
<https://doi.org/10.3390/w1004040>

Downer, C. W., Ogden, F. L., 2004. Appropriate vertical discretization of Richards' equation for two-dimensional watershed-scale modelling. Hydrol. Process., 18, 1-22. doi:10.1002/hyp.1306

Entekhabi, D., Njoku, E.G., Houser, P., Spencer, M., Doiron, T., Kim, Y., Smith, J., Girard, R., Belair, S., Crow, W., Jackson, T.J., Kerr, Y.H., Kimball, J.S., Koster, R., McDonald, K.C., O'Neill, P.E., Pultz, T., Running, S.W., Shi, J., Wood, E., Van Zyl, J., 2004. The hydrosphere state (hydros) satellite mission: An earth system pathfinder for global mapping of soil moisture and land freeze/thaw. IEEE Transactions on Geoscience and Remote Sensing 42, 2184–2195.

Fang H., Baret F., Plummer S., Schaepman., Strub G., 2019. AN OVERVIEW OF GLOBAL LEAF Area Index (LAI): Methods, Products, Validation, and Applications. In Reviews of Geophysics. <https://doi.org/10.1029/2018RG000608>

FAO. 2010. Chapter 1 - Introduction to evapotranspiration Evapotranspiration process. Crop Evapotranspiration - Guidelines for Computing Crop Water Requirements.

Feddes, R. A., Raats, P. A. C., 2004. Parameterizing the soil–water–plant root system. In R. A. Feddes, G. H. de Rooij, & J. C. van Dam Eds., Unsaturated-zone modeling (pp. 364). Dordrecht: Kluwer Academic Publ.

Feddes, R. A., Kowalik, P. J., & Zaradny, H. 1978. Simulation of field water use and crop yield. Simulation Monograph. Wageningen, NL.

Ferencz, C., Bognár, P., Lichtenberge, J., Hamar, D., Tarcsai, G., Timár, G., Molnár, G., Pásztor, S., Steinbach, P., Székely, B., et al. 2004. Crop yield estimation by satellite remote sensing. Int. J. Remote Sens. 2004, 25, 4113–4149, doi: 10.1080/01431160410001698870.

Ferrio, J. P., Villegas, D., Zarco, J., Aparicio, N., Araus, J. L., Royo, C., 2005, Assessment of durum wheat yield using visible and near-infrared reflectance spectra of canopies. Field Crop. Res. 2005, 94, 126–148, doi:10.1016/j.fcr.2004.12.002.

Gerosa, G., 2011. Evapotranspiration: From Measurements to Agricultural and Environmental Applications.

Gobron, N., Verstraete, M. M., 2009. Fraction of Absorbed Photosynthetically Active Radiation FAPAR Global Terrestrial Observing System NRC; Food and Agriculture Organization of the United Nations (FAO): Rome, Italy, 2009; p. 14.

Gorelick, N., Hancher, M., Dixon, M., Ilyushchenko, S., Thau, D., Moore, R., 2017. Google Earth Engine: Planetary-scale geospatial analysis for everyone. Remote Sensing of Environment 202, 18–27.

Goswami, S.; Gamon, J.; Vargas, S.; Tweedie, C., 2015. Relationships of NDVI, Biomass, and Leaf Area Index (LAI) for six key plant species in Barrow, Alaska. PeerJ PrePrints 2015, 3, e913v1, doi:10.7287/peerj.preprints.913v1.

Guilioni, L., Jones, H. G., Leinonen, I., Lhomme, J. P., 2008. On the relationships between stomatal resistance and leaf temperatures in thermography. Agricultural and Forest Meteorology 148, 1908–1912.

Han D., 2018. FAO irrigation and drainage paper no. 56. Global Change Biology. <https://doi.org/10.1080/02626667909491834>

Hatfield, J., Asrar, G., Katemasu. E. T., 1984. Intercepted photosynthetically active radiation estimated by spectral reflectance. Remote Sensing of Environment. (14) 65–75.

HMS 2021: Extreme drought and heat in 2021 June. In Hungarian. met.hu/ismeret-tar/erdekessegek_tanulmanyok/index.php?id=3049&hir=Extrem_szarazsag_es_forrosag_2021_juniusaban

Jackson, R. D., 1986. Remote Sensing of Biotic and Abiotic Plant Stress. Annual Review of Phytopathology 24, 265–287.

Jackson, R. D., Idso, S. B., Reginato, R. J., Pinter, P. J., 1981. Canopy temperature as a crop water stress indicator. Water Resources Research 17, 1133–1138.

Jiang X., Kang S., Tong L ., Li F., Li D., Ding R., Qiu R., 2014. Crop coefficient and evapotranspiration of grain maize modified by planting density in an arid region of northwest China. Agricultural Water Management, 142, 135–143. doi: 10.1016/j.agwat.2014.05.006

Jing Z., Junliang F., Fucang Z., Qianlai Z., 2021. Evapotranspiration partitioning and water productivity of rainfed maize under contrasting mulching conditions in Northwest China, Agricultural Water Management, vol. 243, 2021, 106473, doi: 10.1016/j.agwat.2020.106473.

Jones, H. G., 2004. Irrigation scheduling: advantages and pitfalls of plant-based methods. J Exp Bot 407:2427–2436

Karra; Kontgis; et al., 2021. Global land use/land cover with Sentinel-2 and deep learning. IEEE International Geoscience and Remote Sensing Symposium.

Kristensens, K. J., Jensen, S. E., 1975. A model for estimating actual evapotranspiration from potential evapotranspiration. Hydrol. Res., 6(3), 170-188. doi: 10.2166/nh.1975.0012

Kumar, L., Mutanga, O., 2018. Google Earth Engine Applications since Inception: Usage, Trends, and Potential. Remote Sensing 2018, Vol. 10, Page 1509 10, 1509.

Kurtz, W., He, G., Kollet, S., Maxwell, R. M., Vereecken, H., Hendricks Franssen, H.-J., 2016. TerrSysMP–PDAF (version 1.0): A modular high-performance data assimilation framework for an integrated land surface–subsurface model. Geosci. Model Dev., 9(4), 1341-1360. doi: 10.5194/gmd-9-1341-2016

Kurtz, W., Lapin, A., Schilling, O. S., Tang, Q., Schiller, E., Braun, T., Brunner, P., 2017. Integrating hydrological modelling, data assimilation and cloud computing for real-time management of water resources. Environ. Model. Softw., 93, 418-135. doi: 10.1016/j.envsoft.2017.03.011

Labus, M. P., Nielsen, G. A., Lawrence, R. L., Engel, R., Long, D. S., 2002. Wheat yield estimates using multi-temporal NDVI satellite imagery. Int. J. Remote Sens. 2002, 23, 4169–4180, doi:10.1080/01431160110107653.

Lazzara P., Rana G., 2010. The crop coefficient (K c) values of the major crops grown under Mediterranean climate. Italian Journal of Agrometeorology.

Li, Q., Unger, A. J., Sudicky, E. A., Kassenaar, D., Wexler, E. J., Shikaze, S., 2008. Simulating the multi-seasonal response of a large-scale watershed with a 3D physically-based hydrologic model. Journal of Hydrology, 357, 317–336. https://doi.org/10.1016/j. jhydrol.2008.05.024

Liaqat, U. M., Cheema, M. J., Huang, W., Mahmood, T., Zaman, M., Khan, M. M., 2017. Evaluation of MODIS and Landsat multiband vegetation indices used for wheat yield estimation in irrigated. Comput. Electron. Agric. 2017, 138, 39–47, doi:10.1016/j.compag.2017.04.006.

Liu, L., Wang, J., Bao, Y., Huang, W., Ma, Z., Zhao, C., 2006. Predicting winter wheat condition, grain yield and protein content using multi-temporal EnviSat-ASAR and Landsat TM satellite images. Int. J. Remote Sens. 2006, 27, 737–753, doi: 10.1080/01431160500296867.

Lobell, D. B., 2013. The use of satellite data for cop yield gap analysis. Field Crops Res. 2013, 143, 56–64, doi:10.1016/j.fcr.2012.08.008.

Lyle, G., Lewis, M., Ostendorf, B., 2013. Testing the Temporal Ability of Landsat Imagery and Precision Agriculture Technology to Provide High Resolution Historical Estimates of Wheat Yield at the Farm Scale. Remote Sens. 2013, 5, 1549–1567, doi: 10.3390/rs5041549.

Marti, J., Bort, J., Slafer, G. A., Araus, J. L., 2007. Can wheat yield be assessed by early measurements of Normalized Difference Vegetation Index? Ann. Appl. Biol. 2007, 150, 253–257, doi:10.1111/j.1744-7348.2007.00126.x.

McKee, T., Doesken, N., 1993. 8th, J.K.-P. of the, 1993. The relationship of drought frequency and duration to time scales. climate.colostate.edu 17–22.

Miura T., Huete A., Yoshioka H., 2006. An empirical investigation of cross-sensor relationships of NDVI and red/near-infrared reflectance using EO-1 Hyperion data. Remote Sensing of Environment. <https://doi.org/10.1016/j.rse.2005.10.010>

Mkhabela, M. K., Bullock, P., Raj, S., Wang, S., Yang, Y., 2011. Crop yield forecasting on the Canadian Prairies using MODIS NDVI data. Agric. Forest Meteorol. 2011, 151, 385–393, doi:10.1016/j.agrformet.2010.11.012.

Mokhtari, A., Noory, H., Vazifedoust, M., 2017. Improving crop yield estimation by assimilating LAI and inputting satellite-based surface incoming solar radiation into SWAP model. Agric. Forest Meteorol. 2018, 250–251, 159–170, doi:10.1016/j.agrformet.2017.12.250.

Moran, M., Clarke, T., Inoue, Y., 1994. Estimating crop water deficit using the relation between surface-air temperature and spectral vegetation index. Remote Sensing of Environment, 49 3 246-263, https://doi.org/10.1016/0034-4257(94)90020-5.

Muller, S. J., Sithole, P., Singels, A., Van Niekerk, A., 2020. Assessing the fidelity of Landsat-based fAPAR models in two diverse sugarcane growing regions. Comput. Electron. Agric. 2020, 170, 105248, doi:10.1016/j.compag.2020.105248.

Munitz S., Schwartz A., Netzer Y., 2019. Water consumption, crop coefficient and leaf area relations of a Vitis vinifera cv. “Cabernet Sauvignon” vineyard. Agricultural Water Management. <https://doi.org/10.1016/j.agwat.2019.03.051>

Mustafa, S.M., Abdollahi, K., Verbeiren, B. and Huysmans, M., 2017. Identification of the influencing factors on groundwater drought and depletion in north-western Bangladesh. Hydrogeology journal, 25(5), pp.1357-1375.

Nagy, A., Tamás, J., 2009. Integrated airbone and field methods to characterize soil water regime. In: Ing., A. Celková (szerk.) Transport of water, chemicals end energy in the soil-plant-atmosphere system Bratislava, Szlovákia : Slovak Academy of Sciences Institute of Hydrology, (2009) pp. 412-420. , 9 p.

Nagy, A., Fehér, J., Tamás, J., 2018. Wheat and maize yield forecasting for the Tisza river catchment using MODIS NDVI time series and reported crop statistics. Comput. Electron. Agric. 2018, 151, 41–49, doi:10.1016/j.compag.2018.05.035.

Nash, J. E., Sutcliffe, J. V., 1970. River flow forecasting through conceptual models, Part I–A discussion of principles. J. Hydrol. 1970, 10, 282–290, doi: 10.1016/0022-1694(70)90255-6.

Nerger, L., Hiller, W., 2013. Software for ensemble-based data assimilation systems - Implementation strategies and scalability. Computers & Geosciences, 55(110-118). Doi: 10.1016/j.cageo.2012.03.026

Okołowicz, W., 1977. The climate of Poland, Czechoslovakia and Hungary. In: Wallen CC (ed) Climates of central and southern Europe. Elsevier, Amsterdam/Oxford/New York, pp 75–124 (World Survey of Climatology 6)

Panday, S., Huyakorn, P. S., 2004. A fully coupled physically-based spatially-distributed model for evaluating surface/subsurface flow. Adv. Water Resour., 27, 361-382. doi: 10.1016/j.advwatres.2004.02.016

Panek, E., Gozdowski, D., Stepien, M., Samborski, S., Rucinski, D., Buszke, B., 2020. Within-Field Relationships between Satellite-Derived Vegetation Indices, Grain Yield and Spike Number of Winter Wheat and Triticale. Agronomy 2020, 10, 1842, doi:10.3390/agronomy10111842.

Patela, N. N., Angiuli, E., Gamba, P., Gaughan, A., Lisini, G., Stevens, F. R., Tatem, A. J., Trianni, G., 2015. Multitemporal settlement and population mapping from Landsat using Google Earth Engine. International Journal of Applied Earth Observation and Geoinformation 35, 199–208.

Peltonen, Sainio, P., Juvonen, J., Korhonen, N., Parkkila, P., Sorvali, J., Gregow, H., 2021. Climate change, precipitation shifts and early summer drought: An irrigation tipping point for Finnish farmers. Climate Risk Management, 33, 100334.

Pereira L. S., 2007. Relating water productivity and crop evapotranspiration. In IN: Water use efficiency and water productivity.

Pôças I., Calera A., Campos I., Cunha M., 2020. Remote sensing for estimating and mapping single and basal crop coefficientes: A review on spectral vegetation indices approaches, Agricultural Water Management, vol. 233, 2020, 106081, doi: 10.1016/j.agwat.2020.106081.

Potgieter, A. B., Power, B., Mclean, J., Davis, P., Rodriguez, D., 2014. Spatial Estimation of Wheat Yields from Landsat's Visible, near Infrared and Thermal Reflectance Bands. Int. J. Remote Sens. Appl. 2014, 4, 134–143, doi:10.14355/ijrsa.2014.0403.03.

Price, J. C., 1982. Estimation of Regional Scale Evapotranspiration through Analysis of Satellite Thermal-Infrared Data. IEEE Transactions on Geoscience and Remote Sensing GE-20, 286–292.

Putnam, A. E., Broecker, W. S., 2017. Human-induced changes in the distribution of rainfall. Science Advances, 3(5), e1600871.

Qu Y., Gao Z., Shang J., Liu J., Casa R., 2021. Simultaneous measurements of corn leaf area index and mean tilt angle from multi-directional sunlit and shaded fractions using downward-looking photography, Computers and Electronics in Agriculture, vol. 180, 2021, 105881, doi: 10.1016/j.compag.2020.105881.

Rembold, F., Atzberger, C., Rojas, O., Savin, I., 2013. Using low resolution satellite imagey for yield prediction and yield anomaly detection. Remote Sens. 2013, 11, 1704–1733, doi:10.3390/rs5041704.

Reuben P., Mbiliny P., Mbungu B., Mouruce K., Mahoo H., Schmitter P., 2021. The feasibility of hand-held thermal and UAV-based multispectral imaging for canopy water status assessment and yield prediction of irrigated African eggplant (Solanum aethopicum L), Agricultural Water Management, vol. 245, 2021, 106584, doi: 10.1016/j.agwat.2020.106584.

Rudorff, B., Batista, G., 1991. Wheat yield estimation at the farm level using TM Landsat and agrometeorological data. Int. J. Remote Sens. 1991, 12, 2477–2484, doi:10.1080/01431169108955281.

Rufin P., Frantz D., Yan L., Hostert P., 2021. Operational Coregistration of the Sentinel-2A/B Image Archive Using Multitemporal Landsat Spectral Averages," in IEEE Geoscience and Remote Sensing Letters, vol. 18, no. 4, pp. 712-716, April 2021, doi: 10.1109/LGRS.2020.2982245.

Rummukainen, M., Bergström, S., Persson, G., Rodhe, J., Tjernström, M., 2004. The Swedish regional climate modelling programme, SWECLIM: a review. AMBIO: A Journal of the Human Environment, 33(4), 176-182.

Running, S.W., Nemani, R.R., Peterson, D.L., Band, L.E., Potts, D.F., 1989. Mapping Regional Forest Evapotranspiration and Photosynthesis by Coupling Satellite Data with Ecosystem Simulation. Ecology, 70: 1090-1101. https://doi.org/10.2307/1941378

Running, S. W., Mu, Q., Zhao, M., Moreno, A., 2019. User's Guide MODIS Global Terrestrial Evapotranspiration (ET) Product (MOD16A2/A3 and Year-end Gap-filled MOD16A2GF/A3GF) NASA Earth Observing System MODIS Land Algorithm (For Collection 6).

Ruosteenoja, K., Markkanen, T., Venäläinen, A., Räisänen, P., Peltola, H., 2018. Seasonal soil moisture and drought occurrence in Europe in CMIP5 projections for the 21st century. Climate Dynamics, 50(3), 1177-1192.

Saddik A., Latif R., Elhoseny M., Quardi A., 2021. Real-time evaluation of different indexes in precision agriculture using a heterogeneous embedded system, Sustainable Computing: Informatics and Systems, vol. 30, 2021, 100506, doi: 10.1016/j.suscom.2020.100506.

Schilling, O. S., Doherty, J., Kinzelbach, W., Wang, H., Yang, P. N., Brunner, P., 2014. Using tree ring data as a proxy for transpiration to reduce predictive uncertainty of a model simulating groundwater–surface water vegetation interactions. J. Hydrol., 519, 2258-2271. doi: 10.1016/j.jhydrol.2014.08.063s

Schilling, O. S., Irvine, D. J., Hendricks Franssen., H. J., Brunner, P., 2017. Estimating the spatial extent of unsaturated zones in heterogeneous river-aquifer systems. Water Resour. Res., 53(12), 10583-10602. doi: 10.1002/2017WR020409

Schilling, O. S., Park, Y. J., Therrien, R., Nagare, R. M., 2018. Integrated surface and subsurface hydrological modeling with snowmelt and pore water freeze-thaw. Groundwater, 57(1), 63-74. doi: 10.1111/gwat.12841

Sellers, P. J., 1985. Canopy reflectance, photosynthesis and transpiration. Int. J. Remote Sens. 1985, 6, 1335–1372, doi:10.1080/01431168508948283.

Skofronick-Jackson, G., Berg, W., Kidd, C., Kirschbaum, D. B., Petersen, W. A., Huffman, G. J., Takayabu, Y. N., 2018. Global Precipitation Measurement (GPM): Unified Precipitation Estimation from Space 175–193.

Smith M., Allen R., Pereira L., 1998. Revised FAO methodology for crop-water requirements. International Atomic Energy Agency (IAEA).

Sorooshian, S., AghaKouchak, A., Arkin, P., Eylander, J., Foufoula-Georgiou, E., Harmon, R., Hendrickx, J.M.H., Imam, B., Kuligowski, R., Skahill, B., Skofronick-Jackson, G., 2011. Advanced Concepts on Remote Sensing of Precipitation at Multiple Scales. Bulletin of the American Meteorological Society 92, 1353–1357.

Sun L., Gao F., Xie D., Anderson M., Chen R., Yang Y., Yang Z., 2021. Reconstructing daily 30 m NDVI over complex agricultural landscapes using a crop reference curve approach, Remote Sensing of Environment, vol. 253, 2021, 112156, doi: 10.1016/j.rse.2020.112156.

Tamiminia, H., Salehi, B., Mahdianpari, M., Quackenbush, L., Adeli, S., Brisco, B., 2020. Google Earth Engine for geo-big data applications: A meta-analysis and systematic review. ISPRS Journal of Photogrammetry and Remote Sensing 164, 152–170.

Tang, Q., Kurtz, W., Schilling, O. S., Brunner, P., Vereecken, H., Hendricks Franssen., H.J., 2017. The influence of riverbed heterogeneity patterns on river-aquifer exchange fluxes under different connection regimes. J. Hydrol., 554, 383-396. doi: 10.1016/j.jhydrol.2017.09.031

Tang, Q., Schilling, O. S., Kurtz, W., Brunner, P., Vereecken, H., Hendricks, Franssen., H. J., 2018. Simulating flood induced riverbed transience using unmanned aerial vehicles, physically-based hydrological modelling and the ensemble Kalman filter. Water Resour. Res., 54(11), 9342-9363. doi: 10.1029/2018WR023067

Thomas L. A., Jordan P., Shine O, Fenton O., Mellander E., Dunlop P., 2017. Defining optimal DEM resolution and point densities for modelling hydrologically sensitive areas in agricultural catchments dominated by microtopography. International Journal of Applied Earth Observation and Geoinformation. pp 38-52.

Tsutsumi, M., Itano, S., 2005. Variant of estimation method of above-ground plant biomass in grassland with gamma model 1. Use of an electronic capacitance probe. Grassland Science, 51, 275–279.

Tucker, C. J., Choudhury, B. J., 1987. Satellite remote sensing of drought conditions. Remote Sensing of Environment 23, 243–251.

Tyrnävä Municipality., Tyrnävä., 2002. water supply department, N.O. environmental center, 2002. Preliminary Research Program About the Experiment Uses the groundwater of the cultivation area for irrigation of agricultural production- Tyrnävä.

Uno, Y., Prasher, S. O., Lacroix, R., Goel, P. K., Karimi, Y., Viau, A., Patel, R. M., 2005. Artificial neural networks to predict corn yield from compact airborne spectrographic imager data. Comput. Electron. Agr. 2005, 47, 149–161.

USDA. 2016. Irrigation Water Use. United States Departement of Agriculture, Economic Reasearch Service.

van Genuchten, M. Th., 1980. A closed-form equation for predicting the hydraulic conductivity of unsaturated soils". Soil Science Society of America Journal. 44 (5): 892–898. DOI: 10.2136/sssaj1980.03615995004400050002x.

Vautard, R., Gobiet, A., Jacob, D., Belda, M., Colette, A., Déqué, M., Yiou, P., 2013. The simulation of European heat waves from an ensemble of regional climate models within the EURO-CORDEX project. Climate Dynamics, 41(9-10), 2555-2575.

Vicente-Serrano, S. M., Beguería, S., López, Moreno., J. I., 2010. A multiscalar drought index sensitive to global warming: the standardized precipitation evapotranspiration index. Journal of climate, 23(7), pp.1696-1718.

Vidal, A., Pinglo, F., Durand, H., Devaux, Ros, C., Maillet, A., 1994. Evaluation of a temporal fire risk index in mediterranean forests from NOAA thermal IR. Remote Sensing of Environment 49, 296–303.

Vörösmarty C. J., McIntyre P. B., Gessner M. O., Dudgeon D., Prusevich A., Green P., 2010. Rivers in crisis: global water insecurity for humans and biodiversity. Nature 467, 555–561. Vymazal, J., Sklenicka, P., pp 20

Wan, Z., 2007. Collection-5 MODIS Land Surface Temperature Products Users' Guide.

Wardlow, B., Anderson, M., Verdin, J., 2012. Remote sensing of drought: Innovative monitoring approaches.

Watson D. J., 1947. Comparative physiological studies on the growth of field crops: I. Variation in net assimilation rate and leaf area between species and varieties, and within and between years. Annals of Botany. <https://doi.org/10.1093/oxfordjournals.aob.a083148>

Wesseling, J. G., 1991. Meerjarige simulatie van grondwaterstroming voor verschillende bodemprofielen, grondwatertrappen en gewassen met het model SWATRE. Wageningen: DLO-Staring Centrum (Rapport / DLO-Staring Centrum 152) - 63.

Wójtowicz, M., 2016. U., 2016. Application of remote sensing methods in agriculture. researchgate.net 11, 31–50.

Woodcock, C.E., Allen, R., Anderson, M., Belward, A., Bindschadler, R., Cohen, W., Gao, F., Goward, S.N., Helder, D., Helmer, E., et al., 2008. Free access to Landsat imagery. Science 2008, 320, 1011, doi:10.1126/science.320.5879.1011a.

Woznicki S. A., Nejadhashemi A. P., Parsinejad M., 2015. Climate change and irrigation demand: Uncertainty and adaptation. Journal of Hydrology: Regional Studies. https://doi.org/10.1016/j.ejrh.2014.12.003

Ye, X., Sakai, K., Manago, M., Asada, S.; Sasao, A. 2007. Prediction of citrus yield from airborne hyperspectral imagery. Precis. Agric. 2007, 8, 111–125, doi:10.1007/s11119-007-9032-2.

Yousfi, S., Kellas, N., Saidi, L., Benlakehal, Z., Chaou, L., Siad, D., Herda, F., Karrou, M., Vergara, O., 2015. A. Comparative performance of remote sensing methods in assessing wheat performance under Mediterranean conditions. Agric. Water Mangement 2016, 164, 137–147, doi:10.1016/j.agwat.2015.09.016.

Zhao C., 2021. Harmonization of multispectral satellite date to support parcel level irrigation. MSc Thesis, University of Debrecen.

Zotarelli L., Dukes M., 2010. Step by step calculation of the Penman-Monteith Evapotranspiration (FAO-56 Method): Institute of Food and …, 1–10. https://edis.ifas.ufl.edu/pdffiles/AE/AE45900.pdf

9 Appendices

Appendix 1

A1: Standardized Precipitation Index

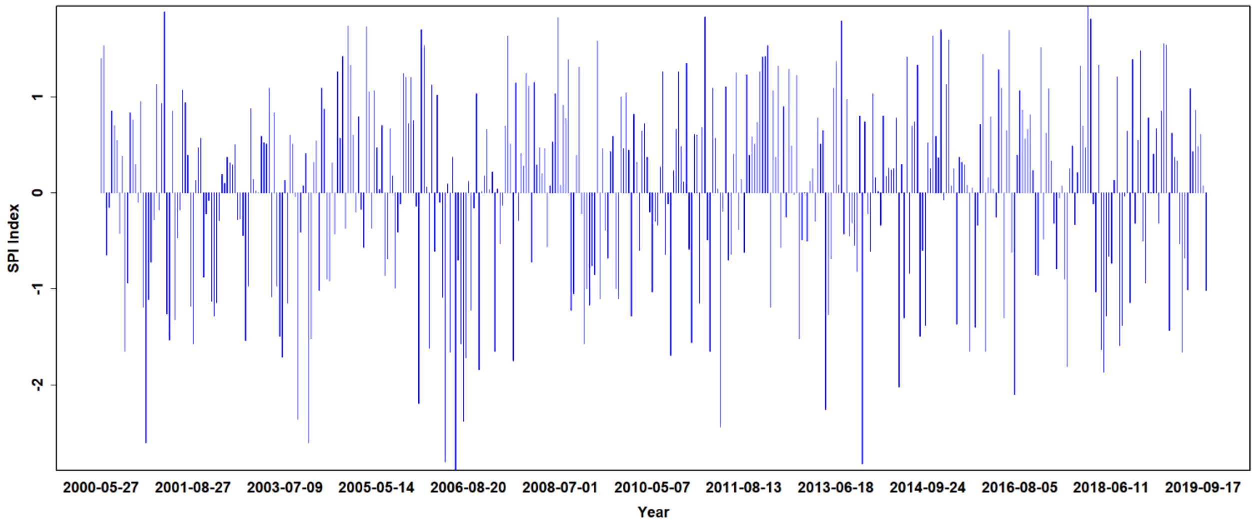

A2: Monthly precipitation rate in June

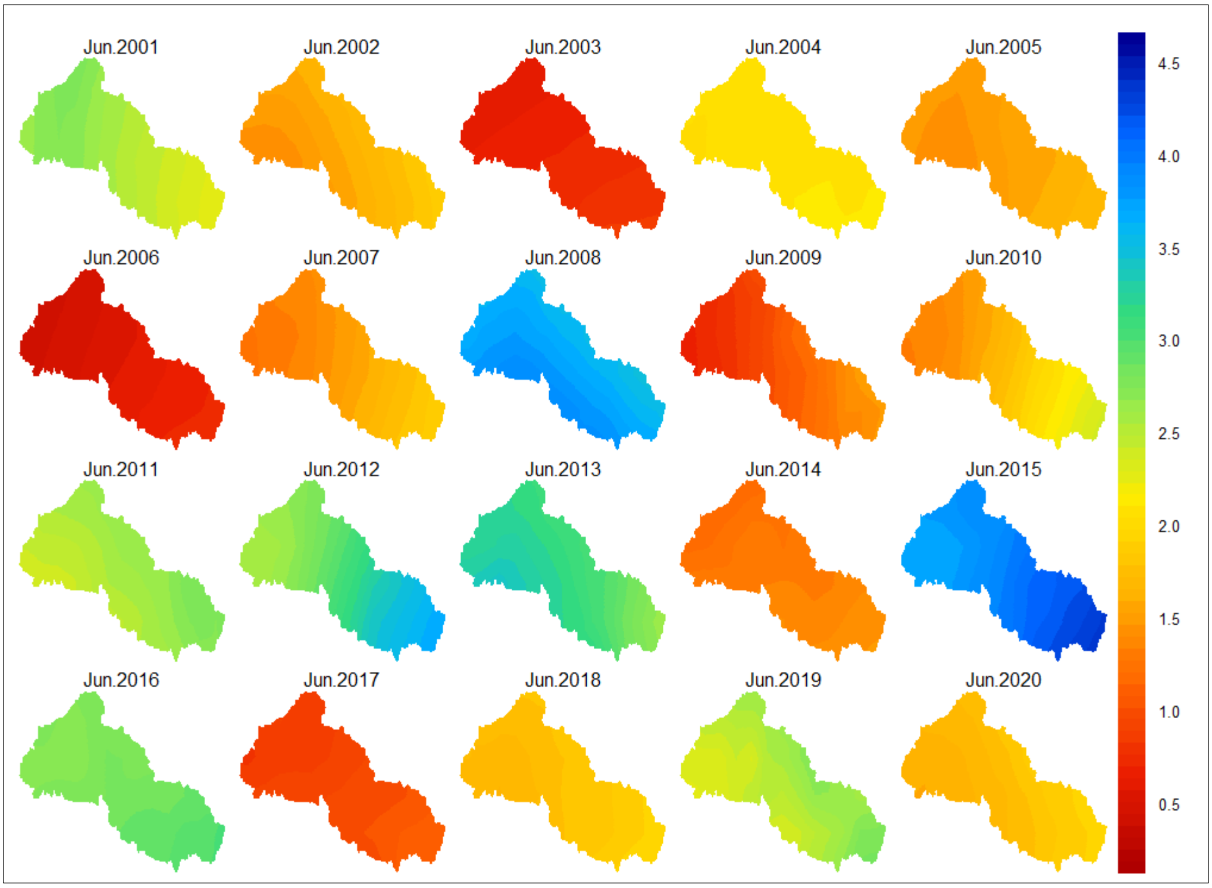

A3: Monthly precipitation rate in July

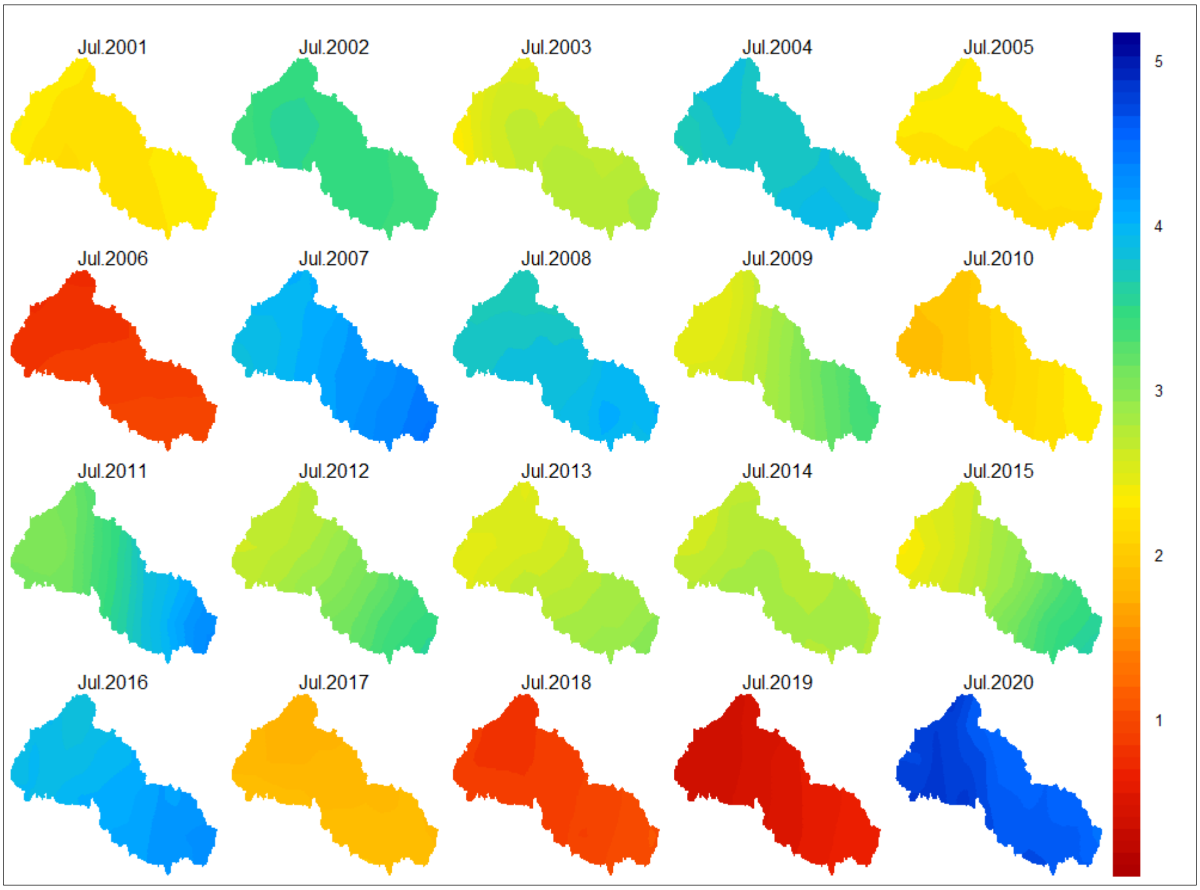

A4: Monthly precipitation rate in Aug

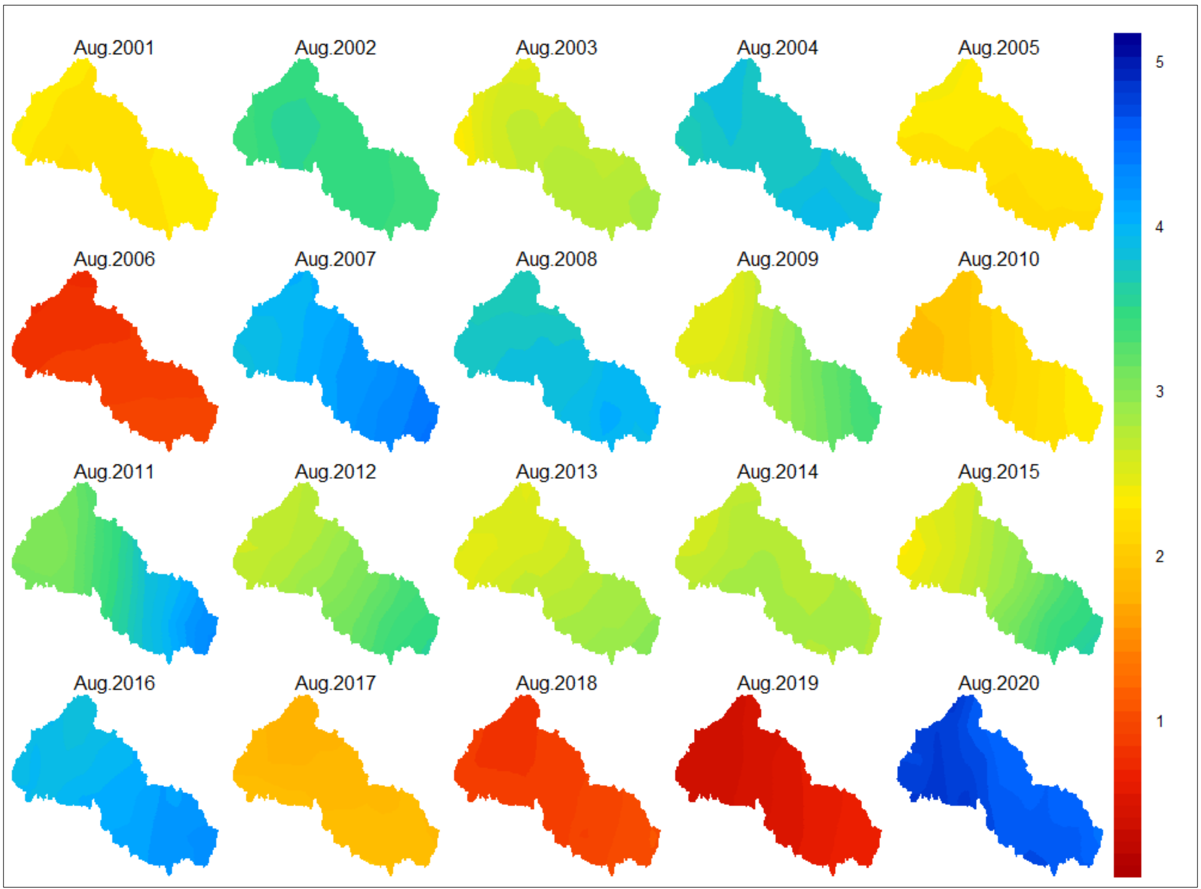

Appendix 2 Temperature Frequency in growing season over the last 20 years in Finnish study site

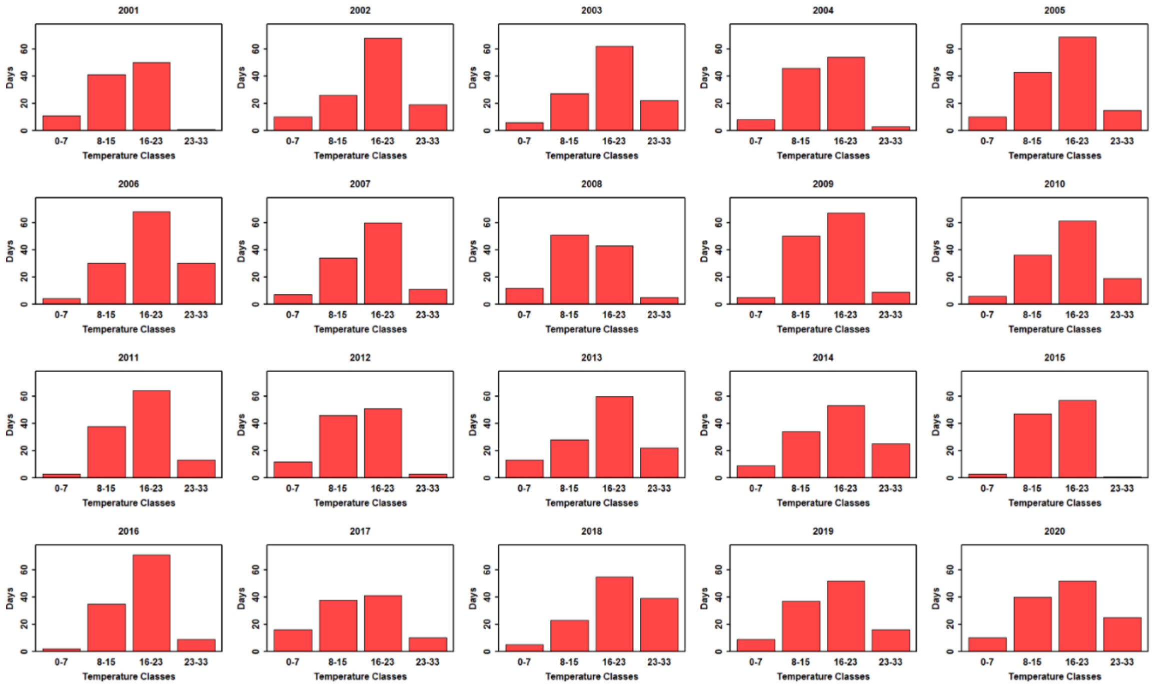

Appendix 3: Italy, 2018

Field ID: 8 Comparison of estimation model performances

Correlation coefficients between estimated ETc curves

	FAO-56			Spectral Indices				
	Original	Curved	MidPoint	LAI	NDRE	NDREw	NDVI	NDWI
Original	1,00	0,98	1,00	0,89	0,93	0,94	0,94	0,94
Curved	0,98	1,00	0,98	0,85	0,89	0,89	0,90	0,91
MidPoint	1,00	0,98	1,00	0,89	0,94	0,94	0,95	0,95
LAI	0,89	0,85	0,89	1,00	0,93	0,95	0,94	0,95
NDRE	0,93	0,89	0,94	0,93	1,00	0,99	1,00	0,99
NDREw	0,94	0,89	0,94	0,95	0,99	1,00	1,00	1,00
NDVI	0,94	0,90	0,95	0,94	1,00	1,00	1,00	0,99
NDWI	0,94	0,91	0,95	0,95	0,99	1,00	0,99	1,00

Regression between calculated empirical and theoretical FAO-56 evapotranspiration series

	SSE	R-sq	DFE	Adj. R-sq	RMSE	nRMSE	a	b	formula
NDWI	18.863	0.954	140	0.953	0.367	9%	1.457	0.747	power
NDWI	20.304	0.950	140	0.950	0.381	10%	0.791	0.815	linear
NDRE	29.959	0.926	140	0.926	0.463	11%	1.796	0.657	power
NDVI	27.205	0.933	140	0.932	0.441	11%	1.602	0.701	power
NDREw	31.968	0.924	140	0.923	0.478	12%	1.583	0.711	power
NDVI	32.203	0.921	140	0.920	0.480	12%	0.778	0.972	linear
NDRE	36.839	0.909	140	0.909	0.513	12%	0.774	1.197	linear
NDREw	36.320	0.913	140	0.913	0.509	12%	0.789	0.941	linear
LAI	69.062	0.809	140	0.808	0.702	20%	1.284	0.743	power
LAI	69.543	0.808	140	0.806	0.705	20%	0.688	0.737	linear

Field ID: 8 Validation of crop evapotranspiration series

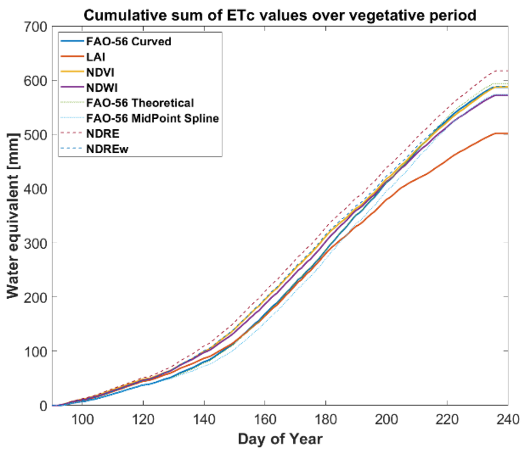

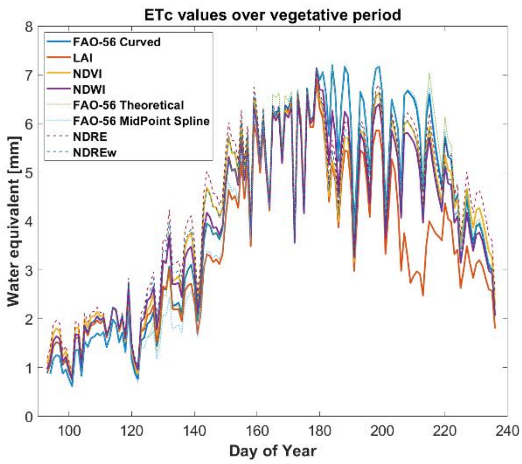

Field ID: 11 Comparison of estimation model performances – table

Correlation coefficients between estimated ETc curves

	FAO-56			Spectral Indices				
	Original	Curved	MidPoint	LAI	NDRE	NDREw	NDVI	NDWI
Original	1,00	0,99	1,00	0,88	0,91	0,90	0,92	0,88
Curved	0,99	1,00	0,99	0,83	0,86	0,85	0,88	0,84
MidPoint	1,00	0,99	1,00	0,89	0,91	0,90	0,92	0,89
LAI	0,88	0,83	0,89	1,00	0,94	0,95	0,95	0,94
NDRE	0,91	0,86	0,91	0,94	1,00	1,00	1,00	0,99
NDREw	0,90	0,85	0,90	0,95	1,00	1,00	0,99	1,00
NDVI	0,92	0,88	0,92	0,95	1,00	0,99	1,00	0,98
NDWI	0,88	0,84	0,89	0,94	0,99	1,00	0,98	1,00

Regression between calculated empirical and theoretical FAO-56 evapotranspiration series

	SSE	R-sq	DFE	Adj. R-sq	RMSE	nRMSE	a	b	formula
NDVI	31.746	0.920	140	0.920	0.476	11%	1.774	0.656	power
NDRE	38.938	0.899	140	0.899	0.527	12%	2.041	0.595	power
NDVI	39.039	0.902	140	0.901	0.528	12%	0.764	1.178	linear
NDREw	44.341	0.873	140	0.872	0.563	13%	2.104	0.563	power
NDWI	48.941	0.850	140	0.849	0.591	13%	2.310	0.517	power
NDRE	48.813	0.874	140	0.873	0.590	13%	0.741	1.503	linear
NDREw	52.685	0.849	140	0.848	0.613	14%	0.692	1.629	linear
NDWI	57.774	0.823	140	0.822	0.642	14%	0.660	1.889	linear
LAI	65.684	0.786	140	0.784	0.685	19%	1.548	0.631	power
LAI	69.416	0.773	140	0.772	0.704	20%	0.620	1.091	linear

Field ID: 11 Validation of crop evapotranspiration series

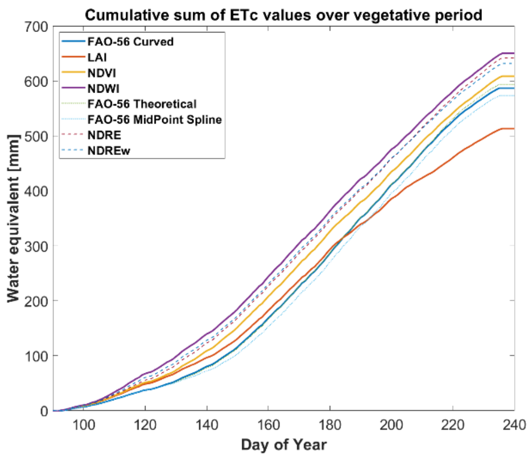

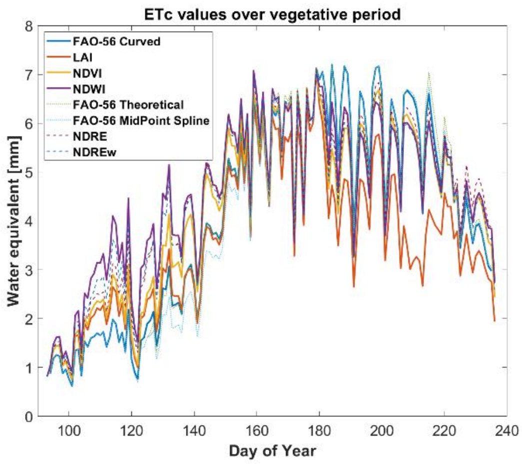

Appendix 4: Italy, 2019

Field ID: 11 Comparison of estimation model performances – table

Correlation coefficients between estimated ETc curves

	FAO-56			Spectral Indices				
	Original	Curved	MidPoint	LAI	NDRE	NDREw	NDVI	NDWI
Original	1,00	0,99	1,00	0,94	0,99	0,99	0,99	0,98
Curved	0,99	1,00	0,99	0,95	0,98	0,98	0,98	0,98
MidPoint	1,00	0,99	1,00	0,95	0,99	0,99	0,99	0,99
LAI	0,94	0,95	0,95	1,00	0,96	0,97	0,97	0,98
NDRE	0,99	0,98	0,99	0,96	1,00	1,00	1,00	0,99
NDREw	0,99	0,98	0,99	0,97	1,00	1,00	1,00	0,99
NDVI	0,99	0,98	0,99	0,97	1,00	1,00	1,00	0,99
NDWI	0,98	0,98	0,99	0,98	0,99	0,99	0,99	1,00

Regression between calculated empirical and theoretical FAO-56 evapotranspiration series

	SSE	R-sq	DFE	Adj. R-sq	RMSE	nRMSE	a	b	formula
NDWI	28.282	0.970	175	0.969	0.402	11%	0.899	1.045	power
NDREw	30.418	0.967	175	0.967	0.417	11%	0.961	0.139	linear
NDWI	29.075	0.969	175	0.969	0.408	11%	0.966	0.032	linear
NDREw	31.301	0.966	175	0.966	0.423	12%	1.013	0.985	power
NDRE	37.752	0.959	175	0.959	0.464	12%	0.958	0.292	linear
NDVI	35.133	0.960	175	0.960	0.448	12%	0.938	0.208	linear
NDRE	38.910	0.958	175	0.958	0.472	12%	1.161	0.922	power
NDVI	36.431	0.959	175	0.959	0.456	13%	1.056	0.956	power
LAI	71.735	0.909	175	0.909	0.640	19%	0.862	0.192	linear
LAI	73.532	0.907	175	0.906	0.648	19%	0.877	1.015	power

Field ID: 11 Validation of crop evapotranspiration series

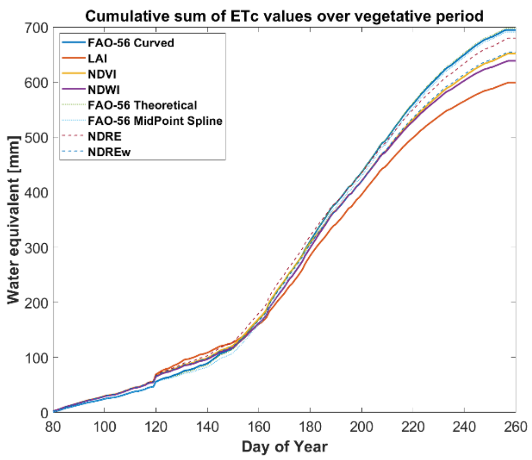

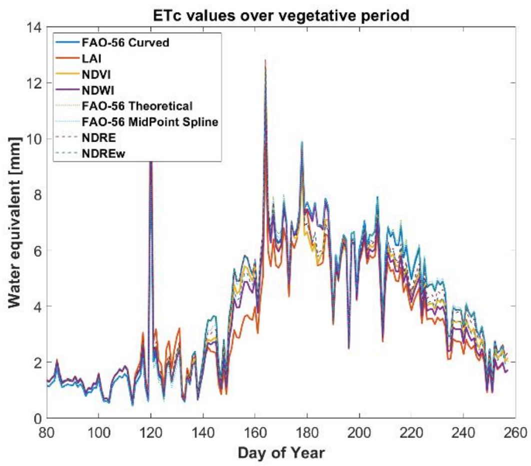

WATERAGRI

Field ID: 15 Comparison of estimation model performances – table

Correlation coefficients between estimated ETc curves

	FAO-56			Spectral Indices				
	Original	Curved	MidPoint	LAI	NDRE	NDREw	NDVI	NDWI
Original	1,00	0,99	1,00	0,94	0,99	0,98	0,99	0,98
Curved	0,99	1,00	0,99	0,95	0,99	0,99	0,99	0,98
MidPoint	1,00	0,99	1,00	0,95	0,99	0,99	0,99	0,98
LAI	0,94	0,95	0,95	1,00	0,96	0,98	0,97	0,98
NDRE	0,99	0,99	0,99	0,96	1,00	1,00	1,00	0,99
NDREw	0,98	0,99	0,99	0,98	1,00	1,00	1,00	1,00
NDVI	0,99	0,99	0,99	0,97	1,00	1,00	1,00	0,99
NDWI	0,98	0,98	0,98	0,98	0,99	1,00	0,99	1,00

Regression between calculated empirical and theoretical FAO-56 evapotranspiration series

	SSE	R-sq	DFE	Adj. R-sq	RMSE	nRMSE	a	b	formula
NDREw	19.386	0.978	175	0.978	0.333	9%	0.939	0.209	linear
NDVI	19.877	0.977	175	0.977	0.337	9%	0.933	0.230	linear
NDREw	20.127	0.977	175	0.977	0.339	9%	1.078	0.945	power
NDVI	20.247	0.976	175	0.976	0.340	9%	1.102	0.931	power
NDRE	21.878	0.976	175	0.976	0.354	9%	1.182	0.911	power
NDRE	22.219	0.976	175	0.975	0.356	9%	0.959	0.279	linear
NDWI	27.821	0.965	175	0.965	0.399	11%	0.892	0.364	linear
NDWI	29.976	0.962	175	0.962	0.414	11%	1.142	0.901	power
LAI	58.370	0.912	175	0.911	0.578	18%	0.789	0.364	linear
LAI	60.562	0.908	175	0.908	0.588	18%	1.040	0.890	power

Field ID: 15 Validation of crop evapotranspiration series

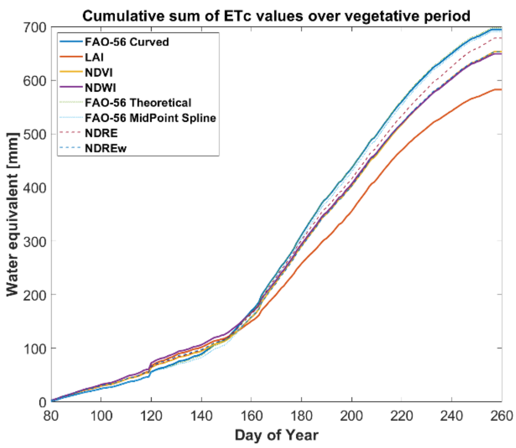

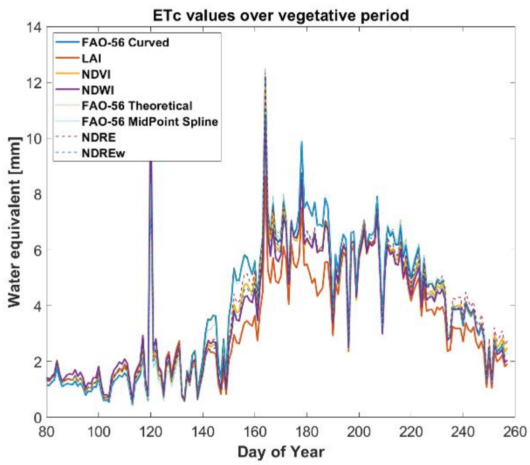

Appendix 5. Italy, 2020

Field ID: 20 Comparison of estimation model performances – table

Correlation coefficients between estimated ETc curves

	FAO-56			Spectral Indices				
	Original	Curved	MidPoint	LAI	NDRE	NDREw	NDVI	NDWI
Original	1,00	0,98	1,00	0,96	0,99	0,99	0,99	0,96
Curved	0,98	1,00	0,98	0,96	0,96	0,97	0,96	0,93
MidPoint	1,00	0,98	1,00	0,96	0,99	0,99	0,99	0,97
LAI	0,96	0,96	0,96	1,00	0,95	0,97	0,96	0,92
NDRE	0,99	0,96	0,99	0,95	1,00	1,00	1,00	0,98
NDREw	0,99	0,97	0,99	0,97	1,00	1,00	1,00	0,97
NDVI	0,99	0,96	0,99	0,96	1,00	1,00	1,00	0,97
NDWI	0,96	0,93	0,97	0,92	0,98	0,97	0,97	1,00

Regression between calculated empirical and theoretical FAO-56 evapotranspiration series

	SSE	R-sq	DFE	Adj. R-sq	RMSE	nRMSE	a	b	formula
NDREw	27.008	0.948	165	0.947	0.405	10%	1.485	0.778	linear
NDREw	31.314	0.939	165	0.939	0.436	11%	0.879	0.745	power
NDVI	32.438	0.939	165	0.939	0.443	11%	1.499	0.777	linear
NDRE	36.678	0.932	165	0.931	0.471	11%	1.664	0.734	linear
NDVI	38.271	0.928	165	0.928	0.482	12%	0.889	0.736	power
LAI	40.806	0.912	165	0.912	0.497	14%	0.822	0.528	power
LAI	41.399	0.911	165	0.911	0.501	14%	1.213	0.839	linear
NDRE	44.800	0.917	165	0.916	0.521	12%	0.884	0.940	power
NDWI	51.603	0.890	165	0.889	0.559	12%	2.230	0.595	linear
NDWI	64.274	0.863	165	0.862	0.624	13%	0.802	1.703	power

Field ID: 20 Validation of crop evapotranspiration series

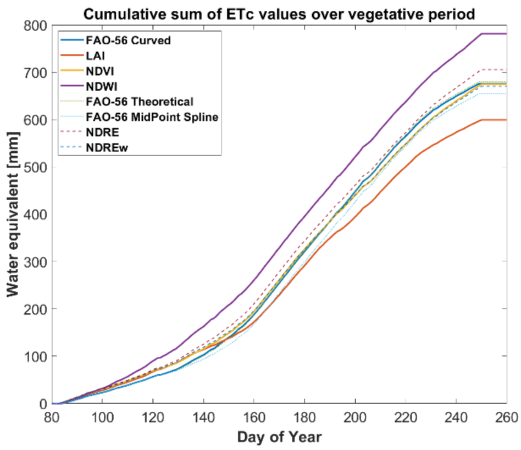

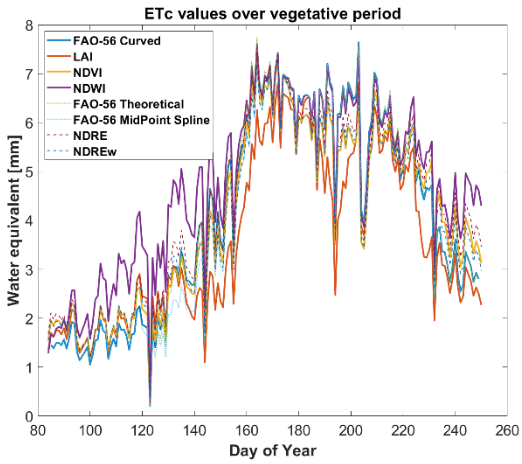

Field ID: 21 Comparison of estimation model performances – table

Correlation coefficients between estimated ETc curves

	FAO-56			Spectral Indices				
	Original	Curved	MidPoint	LAI	NDRE	NDREw	NDVI	NDWI
Original	1,00	0,98	1,00	0,95	0,99	0,99	0,99	0,96
Curved	0,98	1,00	0,98	0,95	0,95	0,96	0,95	0,93
MidPoint	1,00	0,98	1,00	0,96	0,99	0,99	0,99	0,96
LAI	0,95	0,95	0,96	1,00	0,95	0,96	0,95	0,92
NDRE	0,99	0,95	0,99	0,95	1,00	1,00	1,00	0,98
NDREw	0,99	0,96	0,99	0,96	1,00	1,00	1,00	0,97
NDVI	0,99	0,95	0,99	0,95	1,00	1,00	1,00	0,97
NDWI	0,96	0,93	0,96	0,92	0,98	0,97	0,97	1,00

Regression between calculated empirical and theoretical FAO-56 evapotranspiration series

	SSE	R-sq	DFE	Adj. R-sq	RMSE	nRMSE	a	b	formula
NDREw	33.425	0.935	165	0.935	0.450	11%	1.491	0.773	power
NDREw	37.740	0.927	165	0.926	0.478	12%	0.870	0.764	linear
NDVI	41.626	0.921	165	0.921	0.502	13%	1.517	0.766	power
NDRE	44.960	0.916	165	0.915	0.522	12%	1.679	0.727	power
LAI	46.651	0.901	165	0.900	0.532	15%	0.822	0.519	linear
LAI	47.391	0.900	165	0.899	0.536	15%	1.203	0.843	power
NDVI	47.731	0.910	165	0.909	0.538	13%	0.874	0.777	linear
NDRE	53.341	0.900	165	0.900	0.569	14%	0.875	0.968	linear
NDWI	54.341	0.884	165	0.883	0.574	12%	2.241	0.591	power
NDWI	66.850	0.857	165	0.856	0.637	14%	0.797	1.721	linear

Field ID: 21 Validation of crop evapotranspiration series